CHAPTER 2

INTERPRETIVE PROCESSING

The term interpretive processing has been used to describe the use of VSP results in guiding surface seismic processing (Hardage, 1985; Stone, 1981) and for VSP data processed repeatedly whilst modifying a single parameter to estimate reflector dip (Noponen, 1988). Merging of the VSP and intermediate seismic outputs are now emerging that enables the interpreter to continuously gauge the success of multiple attenuation. One such case occurs during model-based transform (MBT) processing (Næss, 1989). Hinds and Durrheim (1993, 1994) used a Karhunen-Loeve (K-L) based multiple attenuation scheme (Jones, 1985; Jones and Levy, 1987) to create an output seismic section that was used as input to MBT processing. Around the well on the seismic line used in that study, the VSP results from the well could be used to further constrain the MBT processing by supplying a model of the primary events in the immediate vicinity of the well.

Interpretive processing of VSP data involves the use of the interpretation of the VSP data to constrain the various processing stages of the VSP data. Flowchart 1 illustrates the procedures of interpretive processing for median filter based wavefield separation. The median filter wavefield separation processing involves amplitude balancing of raw data, static shifting, median filtering to isolate the downgoing events, amplitude balancing of the separated downgoing event data, the subtraction of the data containing up- and downgoing events from the panel containing only downgoing events, static shifting into pseudo-two-way traveltime and upgoing event enhancement.

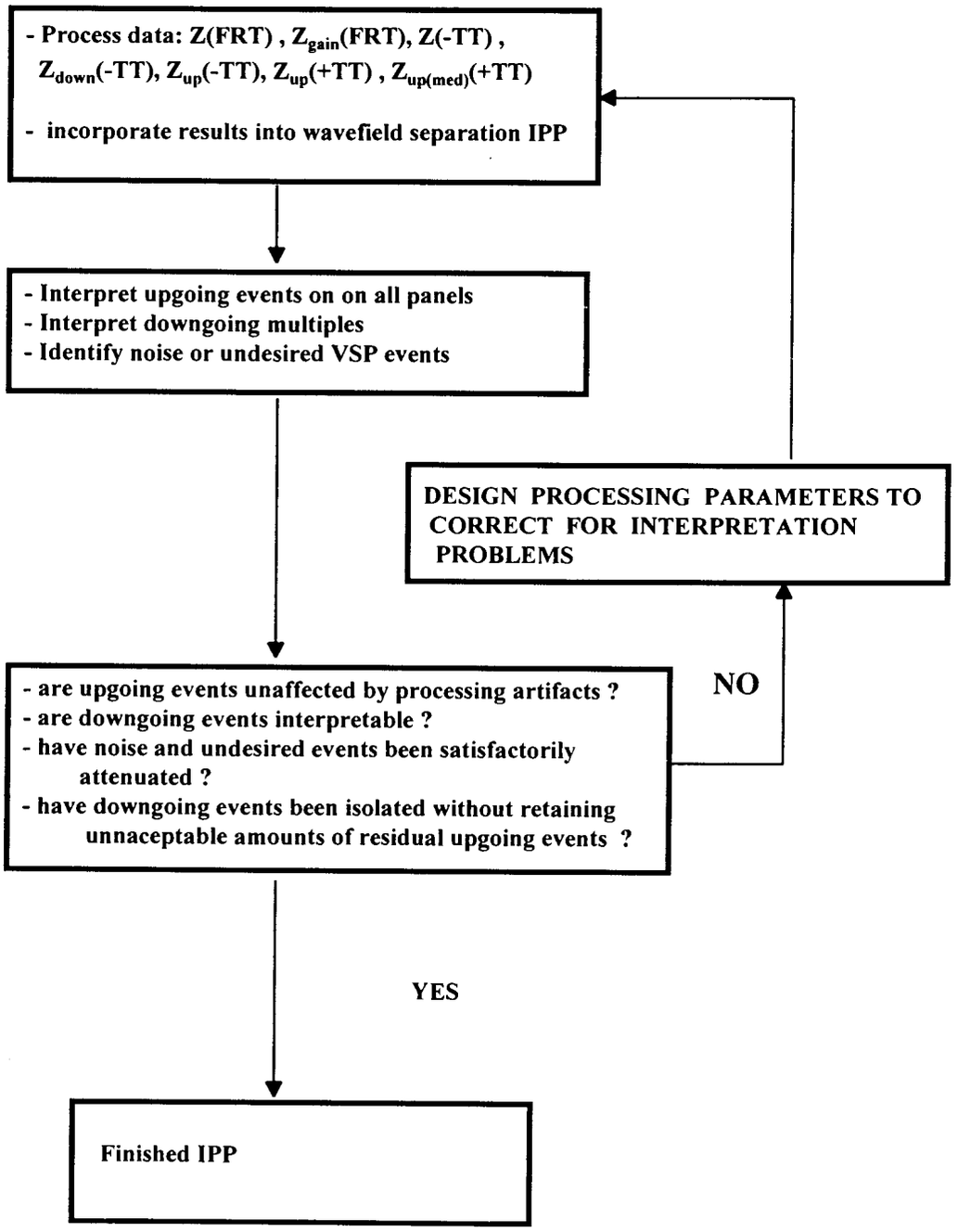

Flowchart 1: An example of the interpretive processing decision-making flowchart for the median filter plus subtraction wavefield separation processing (Hinds et al. 1989a).

An interpretive processing panel (IPP) is constructed (described in section 2.2.2) to examine the input and output of the various processing steps used to isolate the upgoing events into the final display, $\mathbf{Z_{up(med)}(+TT)}$. Here, the subscript describes the type of events within the data and the term in the bracket refers to the data time configuration (see section 1.4.2). The upgoing events in $\mathbf{Z_{up(med)}(+TT)}$ are interpreted; however the interpretation is also placed on the previous outputs along the processing route, such as the $\mathbf{Z_{up}(+TT)}$, $\mathbf{Z_{up}(-TT)}$, $\mathbf{Z_{down}(-TT)}$, **Z(-TT)**, $\mathbf{Z_{gain}(FRT)}$ and **Z(FRT)** data. If any of the processing steps, starting from the raw data, **Z(FRT)**, to the median filtered upgoing event data in pseudo-two-way traveltime, $\mathbf{Z_{up(med)}(+TT)}$, have introduced artifacts that adversely affect the interpretation, then the processing step is modified to eliminate the artifacts. This procedure of generating the IPP and then determining the effect of the processing on the data is repeated until the interpretation is clear of processing artifacts. Using the example of wavefield separation, interpretive processing continues by utilizing the $\mathbf{Z_{up(med)}(+TT)}$, $\mathbf{Z_{up}(+TT)}$, $\mathbf{Z_{down}(-TT)}$ data in the deconvolution processing and within the deconvolution IPP (described in section 2.2.6.1).

An example of processing artifacts is Rieber mixing (Sheriff, 1991) which can occur within Frequency-wavenumber (F-K) wavefield separation processing. As is illustrated further in section 2.2.4, separated upgoing events can be laterally smeared onto depth traces where the event was not recorded if only the narrow range of F-K domain data containing these upgoing events are used during the inverse Fourier transformation. An upgoing multiple event in $\mathbf{Z_{up}(+TT)}$ data could then extend laterally beyond its corresponding primary (Hardage, 1985). The multiple event could be misinterpreted to be a primary event and not a multiple event.

This chapter displays the processing of near and far offset VSP data. The interpretive processing is developed through the use of the IPP and interactive screen processing. Where there are alternative processing routes that can be used, as in the case of wavefield separation, the various wavefield separation techniques are reviewed. The various techniques are formulated into the framework of interpretive processing panels. Where a single method can be used in more than one way to perform a single task, such as **τ-P** wavefield separation processing, a number of different routes are explored. The advantages and disadvantages of using the various routes are then evaluated in terms of the effect on interpretation.

In the far offset VSP processing, a case study presented in this chapter illustrates a normal processing route for the Ricinus data (see chapter 4; Hinds et al.,1989a; Hinds et al., 1993c and Hinds et al., 1994c) which produced results which were contaminated by mode converted downgoing and upgoing SV events. Following the interpretation of these events, it was decided to go back to the **Z(FRT)** and **HMAX(FRT)** data and to perform filtering in order to attenuate the mode converted events at that point in the processing procedure. The data was then successfully reprocessed using wavefield separation and time-variant polarization to output more interpretable results.

The success of far offset VSP deconvolution process is shown to be data dependent. In this chapter, the far offset VSP data of the Ricinus (chapter 4; Hinds et al., 1989a; Hinds et al., 1993c and Hinds et al., 1994c) and Simonette (chapter 6; Hinds et al., 1991b; Hinds et al., 1993b and 1994c) carbonate reef case studies are deconvolved to show the positive and negative effects of far offset VSP deconvolution.

For wavefield separation processing, the use of the median (Hardage, 1985), F-K, K-L (Hinds et al., 1986; Freire and Ulrych, 1988) and τ-P (Hu and McMechan, 1987; Moon et al., 1986; Devaney and Oristaglio, 1986) are demonstrated. In this chapter, it will be shown how the various methods can also be combined to perform individual tasks within another method's wavefield separation IPP. An example of this is the case of using surgical F-K muting to attenuate the aliased tubewave events contaminating the $\mathbf{Z_{up}(+TT)}$ data that were originally wavefield separated from the **Z(-TT)** data using the median filter wavefield separation technique (section 2.2.4.4) . Here the surgical F-K muting technique is used for upgoing P-wave event enhancement.

Interactive screen processing is shown to assist interpretive processing in the evaluation of (1) event identification and (2) the effect of processing parameter selection on event isolation. This type of processing is deemed in this thesis to be a part of interpretive processing (Hinds et al., 1994c).

The final VSP products are used in conjunction with other exploration data in the integrated log display (ILD), integrated seismic display (ISD) and the integrated interpretive display (IID). This allows an additional interpretive check on the processing since the geological log and surface seismic data can be compared to the VSP results. These displays are used within integrated geological/geophysical interpretation (Hinds et al., 1989a, Hinds et al., 1991a, 1991b and 1993c; Hinds et al., 1993a and 1994b; Hinds et al., 1993b, 1994a and 1994c).

2.1 Processing runstreams

The main components of VSP processing to be discussed will be:

(1) up- and downgoing wavefield separation;

(2) VSP deconvolution (Hubbard, 1979);

(3) time-invariant polarization;

(4) time-variant polarization;

(5) VSP-CDP transformation (Dillon and Thomson, 1984); and

(6) VSP migration processing.

Wavefield separation runstreams in the literature highlight a single filter or method to perform the wavefield separation (Lee and Balch, 1983; Lee, 1984; Tariel and Michon, 1984; Beydoun et al., 1990; Shuck, 1988a and b). The runstreams highlight the processing steps; however, Hinds et al., (1989a) produced both near and far offset runstreams through the IPP displays that brought full interpretation into the processing picture.

The runstreams however should be considered to be data dependent since every VSP dataset will contain inherent interpretation problems. The suggested processing presented below and elsewhere in VSP literature should be considered as guidelines. An example near offset processing flow using the median filter wavefield separation (used in Hinds et al., 1989a) could include:

1. geometry design and completion of trace headers;
2. editing of the unstacked **Z(FRT)** data;

3. compensation for source timing errors (as an example, the picking of near-source airgun first breaks and subsequent static shifting of the corresponding VSP data);
4. common sonde location gathering and summation;
5. first break picking of first break compensated **Z(FRT)** data;
6. editing of VSP stacked data;
7. application of a spherical divergence correction for downgoing waves using a velocity model defined by the VSP first break times;
8. static shifting of **Z(FRT)** data to **-TT** alignment, **Z(-TT)** ;
9. application of a median filter to **Z(-TT)** data to isolate downgoing waves and produce the output data, $\mathbf{Z_{down}(TT)}$;
10. scaling of $\mathbf{Z_{down}(-TT)}$ to match the **Z(-TT)** data;
11. subtraction of scaled $\mathbf{Z_{down}(-TT)}$ from **Z(-TT)** to output $\mathbf{Z_{up}(-TT)}$;
12. perform multi-window frequency analysis to design and perform time-variant filtering on $\mathbf{Z_{up}(-TT)}$;
13. design deconvolution operator from $\mathbf{Z_{down}(-TT)}$ and apply to $\mathbf{Z_{up}(-TT)}$ to output $\mathbf{Z_{up(decon)}(-TT)}$;
14. statically shift $\mathbf{Z_{up}(-TT)}$ and $\mathbf{Z_{up(decon)}(-TT)}$ data to output $\mathbf{Z_{up}(FRT)}$ and $\mathbf{Z_{up(decon)}(FRT)}$ data, respectively;
15. apply spherical divergence correction for upgoing waves (model-based) to $\mathbf{Z_{up}(FRT)}$ and $\mathbf{Z_{up(decon)}(FRT)}$;
16. apply normal moveout correction (and simultaneously static shift) to output $\mathbf{Z_{up}(+TT)}$ and $\mathbf{Z_{up(decon)}(+TT)}$;
17. application of median and bandpass filter to enhance upgoing events on $\mathbf{Z_{up}(+TT)}$ and $\mathbf{Z_{up(decon)}(+TT)}$;
18. mute the upgoing wavefield data for use in the outside and inside corridor stack IPP's (Hinds et al., 1989a) of $\mathbf{Z_{up}(+TT)}$ and $\mathbf{Z_{up(decon)}(+TT)}$ data;

The wavefield separation route and analysis of multiple contamination will be data dependent. A reference far offset processing runstream includes two hodogram based trace data rotations, time-variant angle rotation, NMO, VSP-CDP or migration (Hinds et al., 1989a).

Assuming that the **X**, **Y**, **Z** channel data have been edited, common receiver location gathered, stacked and first break picked, an example runstream is presented below:

1. hodogram analysis about a window centred around the first break of the **X(FRT)** and **Y(FRT)** data;
2. rotation of the **X** and **Y** data to output the **HMIN(FRT)** and **HMAX(FRT)** data;
3. hodogram analysis about a window centred around the first breaks of the **HMAX(FRT)** and **Z(FRT)** data;
4. rotation of the **HMAX(FRT)** and **Z(FRT)** data to output the **Z'(FRT)** and **HMAX'(FRT)** data;
5. application of the spherical divergence correction for downgoing waves to the **Z'(FRT)** and **HMAX'(FRT)** data;
6. statically shift the **HMAX'(FRT)** to output **HMAX'(-TT)** data;
7. wavefield separation using the median filter to output **HMAX'$_{down}$(-TT)** data;
8. scaling of the **HMAX'$_{down}$(-TT)** data using a scale factor calculated from an analysis of data from a window around the aligned first break wavelets in the **HMAX'(-TT)** data;
9. subtraction of scaled **HMAX'$_{down}$(-TT)** from **HMAX'(-TT)** to output the **HMAX'$_{up}$(-TT)** data;
10. wavefield separation of the **Z'(FRT)** data using F-K masking to output the **Z'$_{up}$(FRT)** data;
11. application of inverse operation of step (4) on **Z'$_{up}$(FRT)** and **HMAX'$_{up}$(FRT)** to output **Z$_{up(derot)}$(FRT)** and **HMAX$_{up(derot)}$(FRT)**;
12. calculate the time-variant polarization (time, angle pairs) for every depth trace using ray-tracing of upgoing waves reflecting from a model of interfaces created from the first break times and interval velocities of the near offset VSP data;
13. application of the time-variant model-based rotations to the **Z$_{up(derot)}$(FRT)** and **HMAX$_{up(derot)}$(FRT)** to output the **Z"$_{up}$(FRT)** and **HMAX"$_{up}$(FRT)** data;
14. application of a spherical divergence correction to the **Z"$_{up}$(FRT)** data using modelled upgoing traveltimes;
15. application of model-based NMO correction to **Z"$_{up}$(FRT)** data;
16. time-variant bandpass filtering of **Z"$_{up}$(FRT)** data;
17. statically shift **Z"$_{up}$(FRT)** data to output **Z"$_{up}$(+TT)**;
18. application of a median and bandpass filter to **Z"$_{up}$(+TT)** data;

19. application of VSP-CDP transform to output the $\mathbf{Z"_{up}(+TT)}$ data or application of VSP migration to the $\mathbf{Z"_{up}(FRT)}$ data to output the $\mathbf{Z"_{up}}$ data in the **(+TT)** versus offset distance away from the well domain;
20. application of a deconvolution operator calculated from the $\mathbf{HMAX'_{down}(-TT)}$ data to the $\mathbf{Z"_{up}(FRT)}$ to output to $\mathbf{Z"_{up(decon)}(FRT)}$ data;
21. replication of steps (14) to (19) to the $\mathbf{Z"_{up(decon)}(FRT)}$ data to output the VSP-CDP or migrated $\mathbf{Z"_{up(decon)}}$ data in the (+TT) versus offset distance away from the well domain.

2.2 Near offset data processing IPP's

2.2.1 Separation and up- and downgoing waves

The wavefield separation methods described in this section are:

(1) median filtering;

(2) Karhunen-Loeve (K-L) filtering;

(3) Frequency-spatial wavenumber (F-K) filtering; and

(4) time intercept-slowness (τ-P) filtering.

For each method, an IPP is designed to reflect the processing steps of the wavefield separation process. A description of the filter is reviewed with the mathematics for the filter being reserved for the Appendix. The methods and the associated IPP's are described with interpretation in mind. The example data for each method were chosen to highlight interpretational problems that may occur in using the process.

For the median filtering method, the filtering is used to isolate the downgoing events from **Z(-TT)** data into $\mathbf{Z_{down}(-TT)}$ data. The $\mathbf{Z_{down}(-TT)}$ data are amplitude balanced to match the **Z(-TT)** data and then subtracted from the **Z(-TT)** data to output the $\mathbf{Z_{up}(-TT)}$ data.

Similar to the median filtering wavefield separation method, the K-L filtering isolates the $\mathbf{Z_{down}(-TT)}$ data from the **Z(-TT)** data. The filtering transforms the **Z(-TT)** into its principal components with the first (and largest) principal components representing the horizontally aligned downgoing events. The data are inverse transformed using only the first few principal components. Subtraction of the $\mathbf{Z_{down}(-TT)}$ data from the **Z(-TT)** data yields the separated upgoing events.

The F-K method transforms the **Z(FRT)** data into the F-K domain. In this domain, the upgoing events reside in the negative wavenumber quadrant and the downgoing events in the positive quadrant. Using quadrant or surgical F-K muting, the downgoing events are muted from the F-K domain. The F-K data are then inverse transformed to output the isolated upgoing events, $\mathbf{Z_{up}(FRT)}$.

In the F-K filtering section, F-K wavefield separation IPP and interactive F-K screen processing are reviewed. The problems encountered in F-K filtering with Rieber mixing (Hardage, 1985), spatial aliasing and events crossing within the F-K domain are addressed.

The τ-P filtering based wavefield separation method relies on the different slownesses of the up- and downgoing events to perform the separation (Hardage, 1992; Hu and McMechan, 1987). In this section, the τ-P filter is used to perform velocity filtering and spatial

interpolation (Hu and McMechan, 1987). The spatial interpolation is used in the separation step and as a pre-processing step for other wavefield separation methods (Hinds et al., 1994c).

One way to view the examples is to recognise the types of problems (such as random noise, tubewave and SV event contamination) present within each example dataset and then to look for similarities between industry data and the example VSP data. The second way is to compare the chapter 2 data once the data have been interpreted in the case histories. The way in which the various filtering methods shown in chapter 2 have aided or distorted the final interpretations is shown in chapters 3 to 6. The interpretations are not presented in depth in this chapter; however, the development of interpretive processing (IPP and interactive processing) and associated displays is stressed.

2.2.2 Median filtering

In this section, the wavefield separation method will use the median filter. The flowchart of the wavefield separation procedure using the median filter is shown in Flowchart 2. The median filter is used to isolate the downgoing events from the **Z(-TT)** data into the downgoing event data shown in the $\mathbf{Z_{down}(-TT)}$ panel. The isolated downgoing events are scaled and then subtracted from the up- and downgoing events of the **Z(-TT)** data resulting in the upgoing event data displayed in the $\mathbf{Z_{up}(-TT)}$ data panel. Following static shifting and further median filtering, the $\mathbf{Z_{up(med)}(+TT)}$ data are interpreted. The interpretation is then placed on all of the data panels starting from the **Z(FRT)** data to the $\mathbf{Z_{up(med)}(+TT)}$ data.

FLOWCHART - Wavefield separation using the median filter method

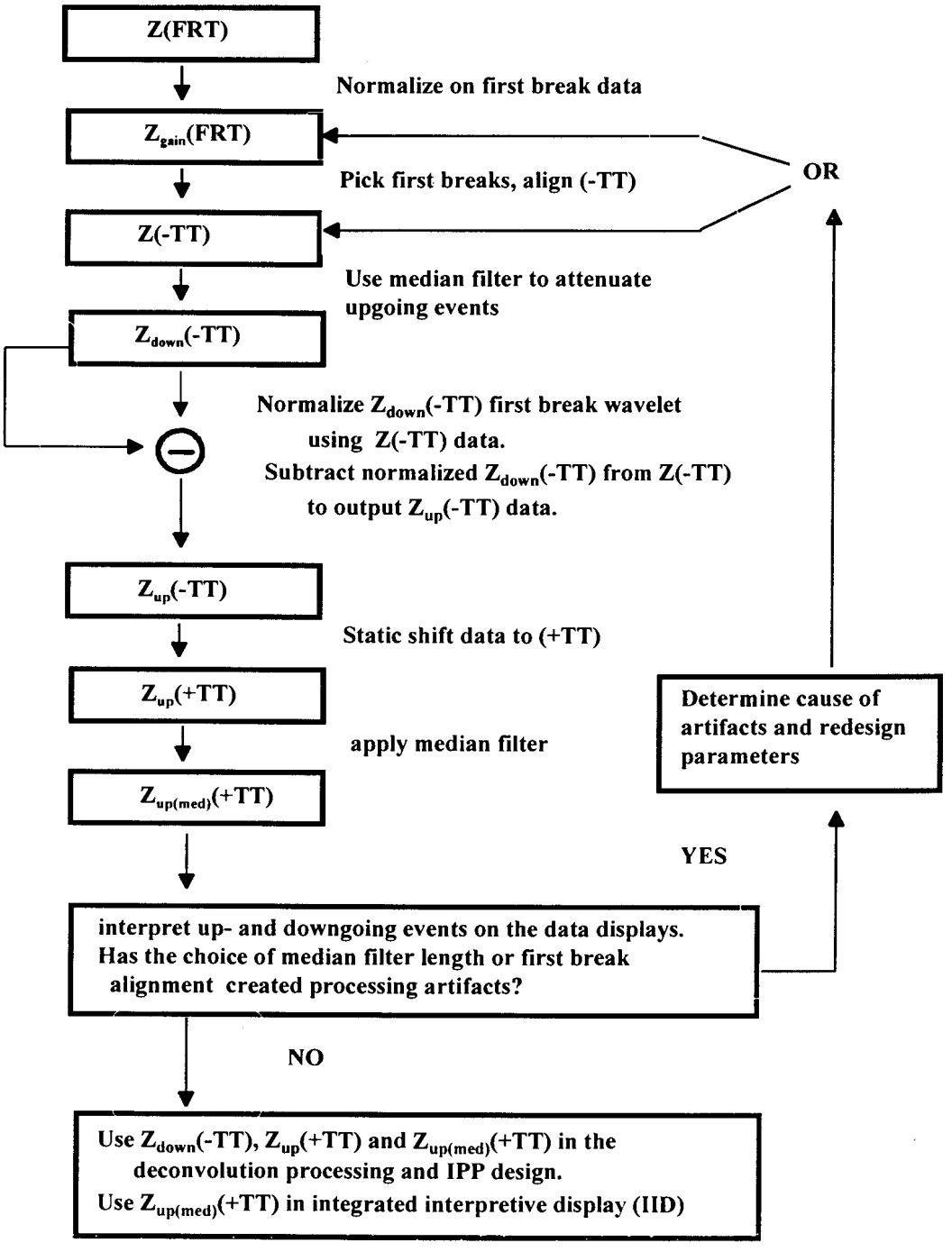

Flowchart 2: An example of the interpretive processing flowchart for the median filter plus subtraction wavefield separation processing (Hinds et al., 1989a).

An analysis of the effect of each processing step on the interpretation of the upgoing events is done. When using the median filter for wavefield separation, the two areas that are of concern are (1) the first break picking and (2) the length of the median filters used to perform upgoing event isolation and upgoing event enhancement. The first breaks times are repicked or lengths of the median filters applied are modified and the processing is repeated if improper first break picking or the wrong choice of median filter lengths have resulted in processing artifacts that adversely affect the interpretation. The use of the median filter within a wavefield separation IPP on multiple and tubewave contaminated data are shown in the sections below.

2.2.2.1 Review of the median filter

The theoretical basis of the one- and two-dimensional median filter has been reviewed in Arce et al. (1986), Fitch et al. (1984), Arce and McLoughlin (1984), Gallagher and Wise (1981) and Nodes and Gallagher (1982). Kommedal and Tjostheim (1989) and Hardage (1985) published studies that compared the median filter based wavefield separation methods to other wavefield separation methods.

The input data to the 1-D median filter is a window of data points from a series of depth traces for a single time value. The number of windowed data points can be an even or odd value, (2N or 2N+1). Since the median filter requires N points before and after the centre data point within the data window, data padding is done at the edge of the dataset (the shallowest and deepest data traces are repeated to perform the padding).

For an example, consider a 7 point median filter. During the filtering, the sliding constant time window would contain data values from 7 depth traces. These seven values are sorted according to magnitude with the centre value of the sort being termed the median value. That median value becomes the value for the fourth depth trace within the same window for the resultant output data. The median filter window keeps sliding across the data until all of the depth traces of the input data have been processed. All of the traces at the next time value are then processed.

For the odd numbered point filter, the median value at the centre of the sorted windowed time series becomes the new value of the output series. When N is even, the mean of the two middle median values is the output of the filter. The equations for the median filtering are discussed in the Appendix.

2.2.2.2 Median filtering and multiple contaminated VSP data

Figure 2.1 is the median filter based wavefield separation IPP for the multiple contaminated near offset data of the Fort St. John Graben case history (Hinds et al., 1991a; Hinds et al., 1993a and 1994b; Hinds et al., 1994c) discussed in detail in chapter 5. The raw **Z(FRT)** data are equalized using a window centred on the first break wavelets and the resultant data are shown in panel 1 of Figure 2.1. By inspection, it is clear that the downgoing waves are orders of magnitudes larger in amplitude than the upgoing waves (Hardage, 1985). The depth variable increases along the horizontal axis from left to right in panels 1-7 and traveltime increases downwards. Strong repetitious downgoing multiple wavetrains in panel

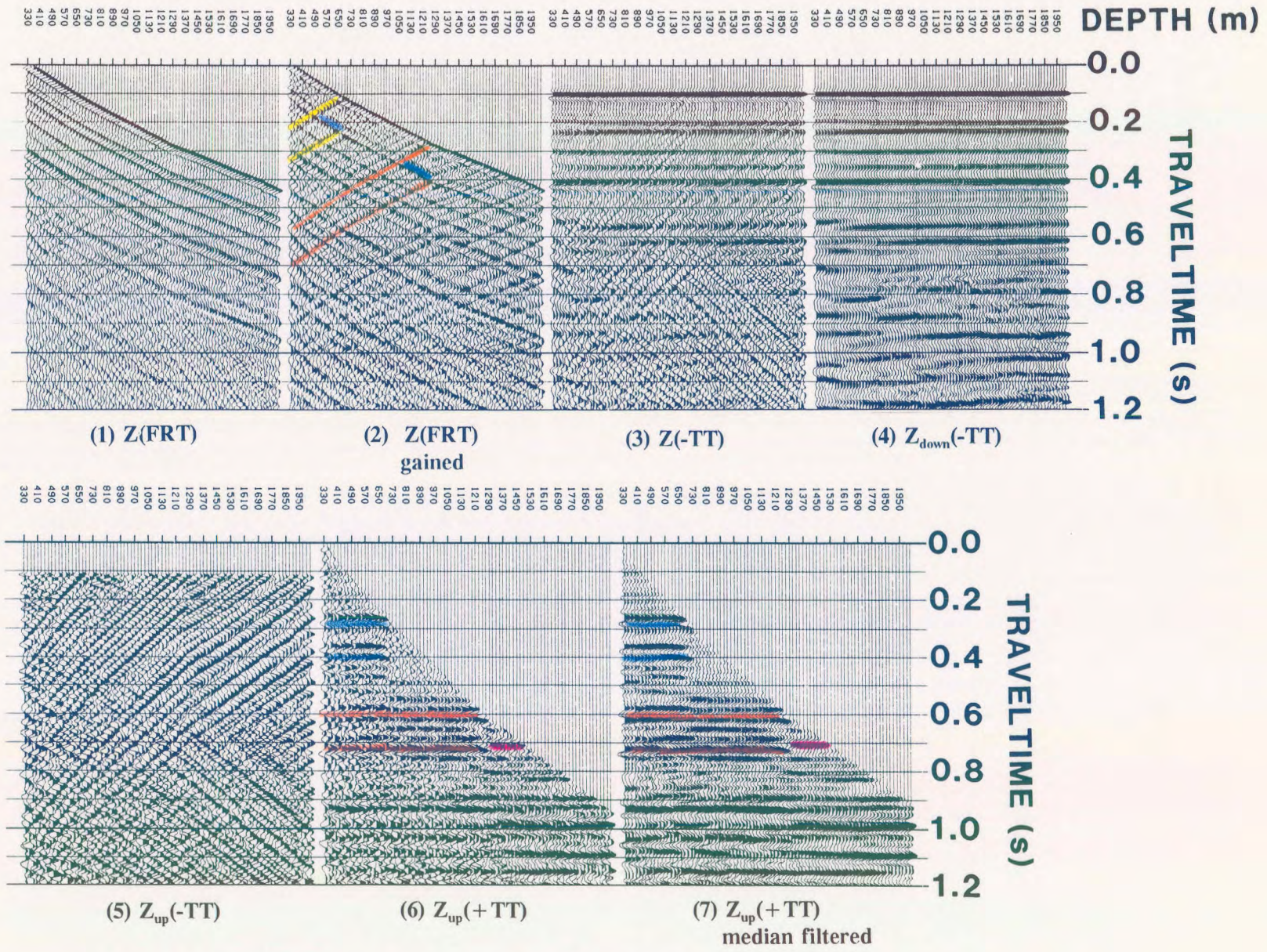

Figure 2.1 Wavefield separation IPP of the Fort St. John Graben case study (Hinds et al., 1993a) data using the median filter and subtraction method (Hinds et al., 1989a).

1 follow the first breaks.

In panel 2, the **FRT** data have been gained (a form of programmed gain control) to show the inter-relationship between the up- and downgoing multiples. One particular multiple represented by the series of reflections beginning with the reflected upgoing event (trough) generated at an interface at about 690 to 710 m (Spirit River Formation; see Chapter 5) can be tracked. The upgoing primary event is highlighted on panel 2. The upgoing event intersects the primary downgoing "curve" at about 0.115 s **FRT** traveltime between the 690 and 710 m traces. The upgoing event can be traced (increasing in traveltime with decreasing depth) back to the shallowest trace (at approximately 0.24-0.25 s). The intersection of the same event with the surface generated downgoing multiple occurs at 0.19 s on the trace for 470 m. The downgoing surface generated multiple (coloured blue) is opposite in polarity (a trough) to the primary downgoing wave (the same polarity as the upgoing primary). The intersection of the two waves is only noted to guide the reader; there is no physical significance to the intersection. If the highlighted portion of the downgoing multiple (coloured yellow) is followed deeper in time to 0.22 s on the 690-710 m trace, it is clear that the downgoing multiple reflects at the 690 m interface and creates an upgoing multiple (a peak). The highlighted upgoing multiple only exists on traces shallower than the 690 m trace (this can be seen more clearly in the absence of downgoing events on panels 5, 6 and 7). We have thus reached our first interpretive processing objective; namely, that this multiple described above must be preserved during the wavefield separation method such that the extent of the upgoing multiple event does not extend to traces deeper than 690 m.

What are the timing relationships? The time delay between the downgoing primary (peak)

and the first strong surface generated downgoing multiple (trough) is the same time delay as between an upgoing primary event (the Spirit River event of Chapter 5; Hinds et al., 1991a; Hinds et al., 1993a and Hinds et al., 1994c) which is a dominant trough at 0.28 s on panel 7 (coloured blue) and the corresponding upgoing multiple (a peak at 0.4 s on panel 7 coloured blue).

A clear upgoing event generated at about 1250 m depth (Nordegg Formation event described in Chapter 5) is highlighted (in orange) on panels 2, 7 and 8 and a set of associated upgoing multiples are generated in the same way as were the multiples described above for the Spirit River Formation interface (at 690 m). The first upgoing multiple of the Nordegg Formation interface resulting from the surface generated downgoing multiple is also highlighted in orange and occurs at approximately 0.725 s on panels 6 and 7. On panel 3, the **Z(FRT)** data are statically shifted to **Z(-TT)**. The first break is aligned at 100 ms so as not to lose any part of the first break wavelet. If the first break would have been picked as the dominant trough of the first break (following the strong peak) and was shifted to the time origin, then the data appearing before the trough would have effectively been muted.

In panel 4 of Figure 2.1, an 11 point median filter has been used to isolate the horizontally aligned downgoing wavefield events. The median filtering wavefield separation technique is really a three-part exercise. In **(-TT)** time, the method consists of:

1) separating the downgoing waves, $\mathbf{Z_{down}(-TT)}$, from the combined wavefield data, **Z(-TT)**;
2) amplitude balancing the separated downgoing waves, $\mathbf{Z_{down}(-TT)}$, with the combined

wavefield data, **Z(-TT)**; and

3) subtracting the amplitude balanced downgoing waves, $\mathbf{Z_{down}(-TT)}$ from the combined wavefield data, **Z(-TT)**, to obtain the upgoing events, $\mathbf{Z_{up}(-TT)}$.

The combined wavefield data, downgoing events, and separated upgoing events **(-TT)** are shown in panels 3, 4, and 5, respectively. The data are placed into **(+TT)** by first break time shifting (as shown in Fig. 1.4). At this stage, a second multiple problem that can be detected using interpretive processing can be seen on Figure 2.1 ! Amidst the upgoing multiples starting from 0.6 - 0.8 s on panels 6 and 7, there is an upgoing primary (since it intersects the first break curve in panel 2, 5, and 6 on the 1470-1490 m traces) at 0.7 s. This primary event which is highlighted in red on panel 7 of Figure 2.1 must be preserved during the deconvolution processing.

Through the use of interpretive processing, it can be determined that the median filter wavefield separation method has preserved the edge (lateral extent) of the upgoing multiples and has preserved the discontinuity between the primary from 1470 m and the multiples in which the primary is superimposed. The $\mathbf{Z_{up}(FRT)}$ data in panel 6 are enhanced using a short length median filter and the enhanced version is presented in panel 7 of Figure 2.1. This has turned out to be a classic multiple data example which can be used for the other wavefield separation methods.

2.2.2.3 Median filtering and tubewave contaminated VSP data

Another example of the median filter based wavefield separation IPP is shown in Figure 2.2 for tubewave contaminated data. Hardage (1981, 1985) gives a thorough description of the tubewave and its appearance on VSP data. The shallowest trace was recorded at 410 m depth so that the origin of the tubewave event could be traced to the surface. The tubewave is most likely due to the first arrival of the Rayleigh ground roll wave and the action of the wave at the wellhead causing vertical motion in the borehole fluid column (Hardage, 1985). This would be categorized as Hardage's Tubewave Mode 2 (Hardage, 1981). The questions are whether one needs to or can attenuate the tubewave in order to better interpret upgoing events that the noise event may be superimposed upon. On panel 2, the gained data reveal that the tubewave event is spatially aliased. Spatial aliasing is discussed in Yilmaz (1987) and Hardage (1985). The depth increment of 30 m was not adequate to sample the low velocity tubewave. The up- and downgoing tubewave events are highlighted on panels 1, 2 and 3.

In the $\mathbf{Z_{down}(-TT)}$ data shown in panel 4, much of the downgoing tubewave event has been eliminated from the combined wavefield data, **Z(-TT)**, shown in panel 3. This implies that the entire downgoing tubewave will not be subtracted out of the **Z(-TT)** data during the wavefield separation and the aliased part of the tubewave that appears to be upgoing events will remain in the $\mathbf{Z_{up}(-TT)}$ data . In panel 5, the gained separated upgoing data, $\mathbf{Z_{up}(-TT)}$, still contains the high amplitude tubewave event. The aliased tubewave event that has not been eliminated is highlighted in yellow on panels 5-8. The $\mathbf{Z_{up}(+TT)}$ and $\mathbf{Z_{up(med)}(+TT)}$ data in panels 6 and 7, respectively, show the interference of the tubewave with the upgoing

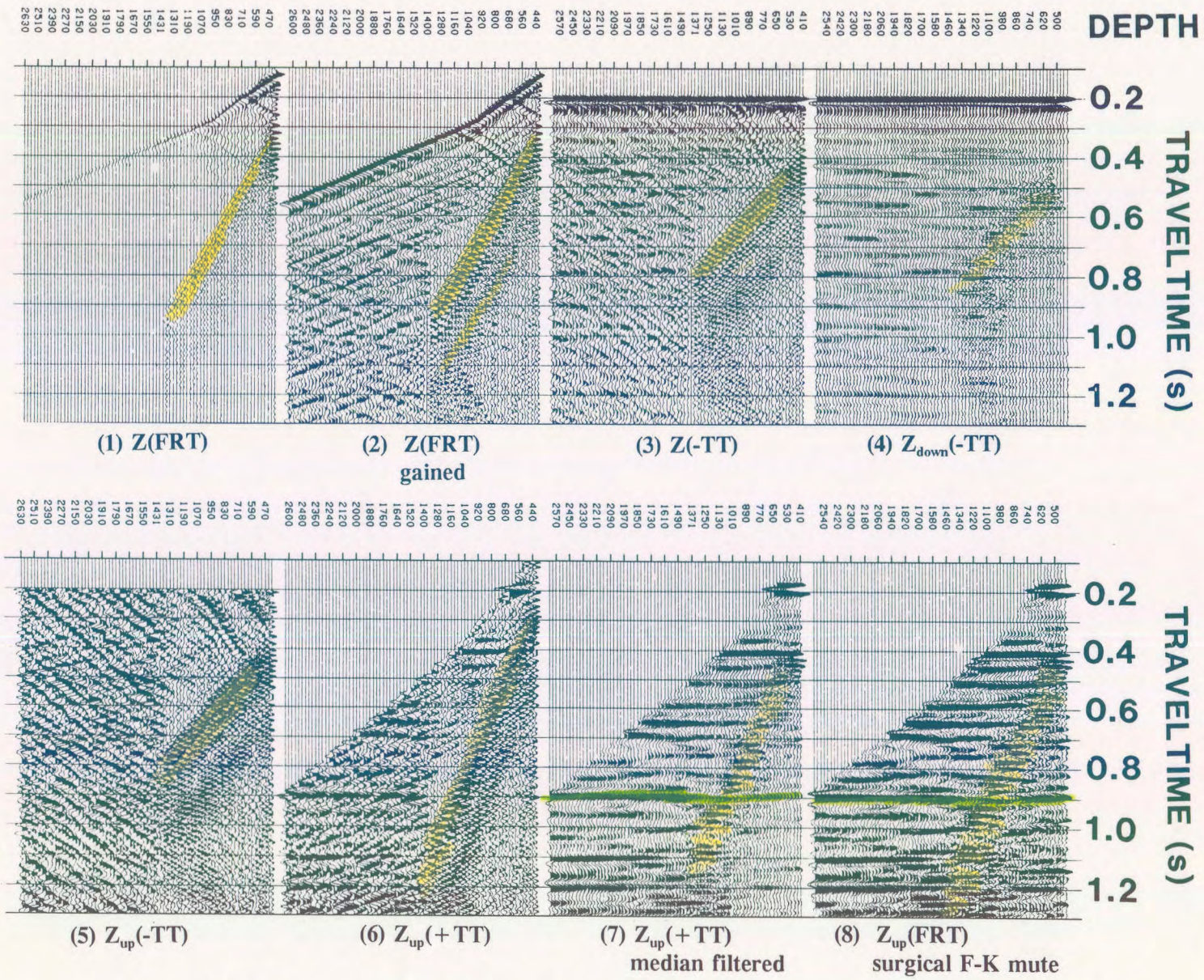

Figure 2.2 Wavefield separation IPP of the tubewave contaminated data using the median filter and subtraction method (Hinds et al., 1989a). The F-K domain plot of the surgical muting (panel 8) is displayed in Figure 2.17.

primary events. A striking example is the interference of the upgoing primary located at 0.9 s and highlighted (in green) on panels 7 and 8.

Panel 8 shows the upgoing events after surgical F-K muting of some of the aliased tubewave F-K response. The F-K plot of the data following the surgical muting is shown later in Figure 2.17. The events surrounding the tubewave event have been raised in amplitude; however, the tubewave event still inhibits the interpretation of the upgoing events along its path where the aliased (appearing as upgoing events "within" the tubewave event) portion of the tubewave event constructively and destructively interferes with the flat lying upgoing P-wave primary events. Using a longer length median filter in producing the $\mathbf{Z_{up(med)}(+TT)}$ data of panel 7 would eliminate more of the downgoing tubewave from the data; however, amplitude variations within the upgoing events would not be preserved.

2.2.2.4 Difference panels to aid in filter length determination

Do we have intermediate steps that can be used to choose the length of the median filter to be used? In panels 1-5 of Figure 2.3, a series of $\mathbf{Z_{down}(-TT)}$ data panels for a marine near offset VSP have been produced using a 3, 5, 7, 9, and 11 point median filter on the original **Z(-TT)** data, respectively. The separated downgoing waves appear similar with minor amounts of residual upgoing waves left in panels 1 and 2. In panels 6, 7, 8, and 9, the 11 point median $\mathbf{Z_{down}(-TT)}$ data have been subtracted from the 3, 5, 7, and 9 point median filter panels, respectively to form a difference panel. The amount of residual upgoing events left in the downgoing wavefield panels can be shown relatively simply through the use of the difference panels. The 3, 5, and 7 point median filters are not suitable for the wavefield

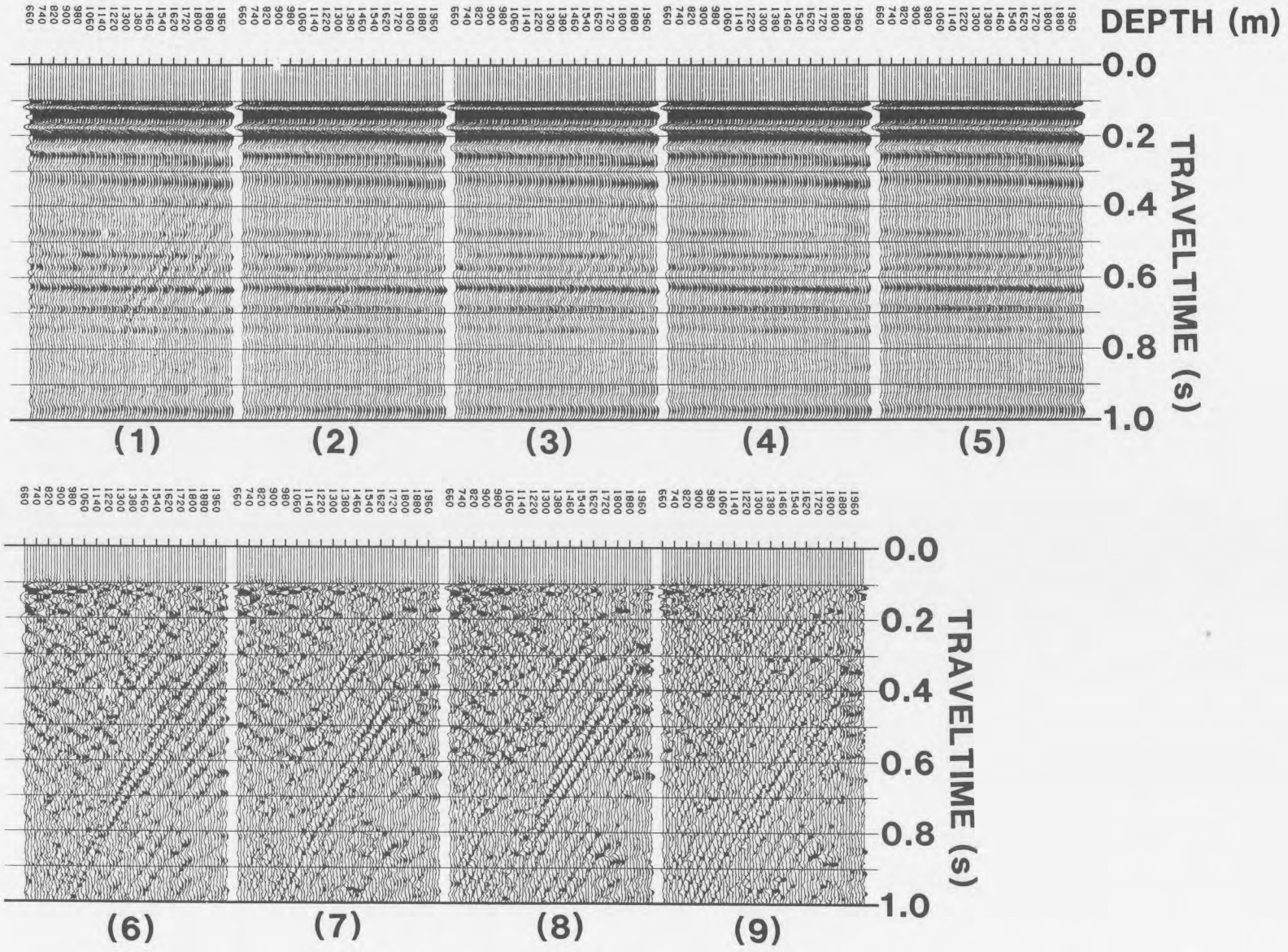

Figure 2.3 Downgoing event panels separated from **Z(-TT)** data using a 3, 5, 7, 9 and 11 point median filter (panels 1-5, respectively). Panels 6-9 display the subtraction of the data in panel 5 from the data and 1, 2, 3 and 4, respectively.

separation technique with this particular VSP dataset. This exercise is important because any residual upgoing wave events left in the $\mathbf{Z_{down}(-TT)}$ data will be subtracted out of the **Z(-TT)** during wavefield separation and can never be recovered.

2.2.3 Karhunen-Loeve (K-L) filtering

In this section, the wavefield separation method will use the K-L transform. Flowchart 3 shows the wavefield separation procedure using the K-L transform. The gained **Z(-TT)** data are K-L transformed; the K-L domain consists of principal components which are related to the eigenvectors of the data autocovariance matrix (see Appendix for details). The eigenvalues associated with the eigenvectors are indicative of horizontal coherency within the data. As shown in the flowchart, the data are reconstructed (inverse K-L transformed) excluding the principal components that represent the horizontally aligned downgoing events. The data within the K-L IPP are interpreted and if processing artifacts have been introduced into the data, those processing steps that introduced the artifacts are modified and repeated until the interpretation of the data is unaffected.

FLOWCHART - Wavefield separation using the K-L transform method

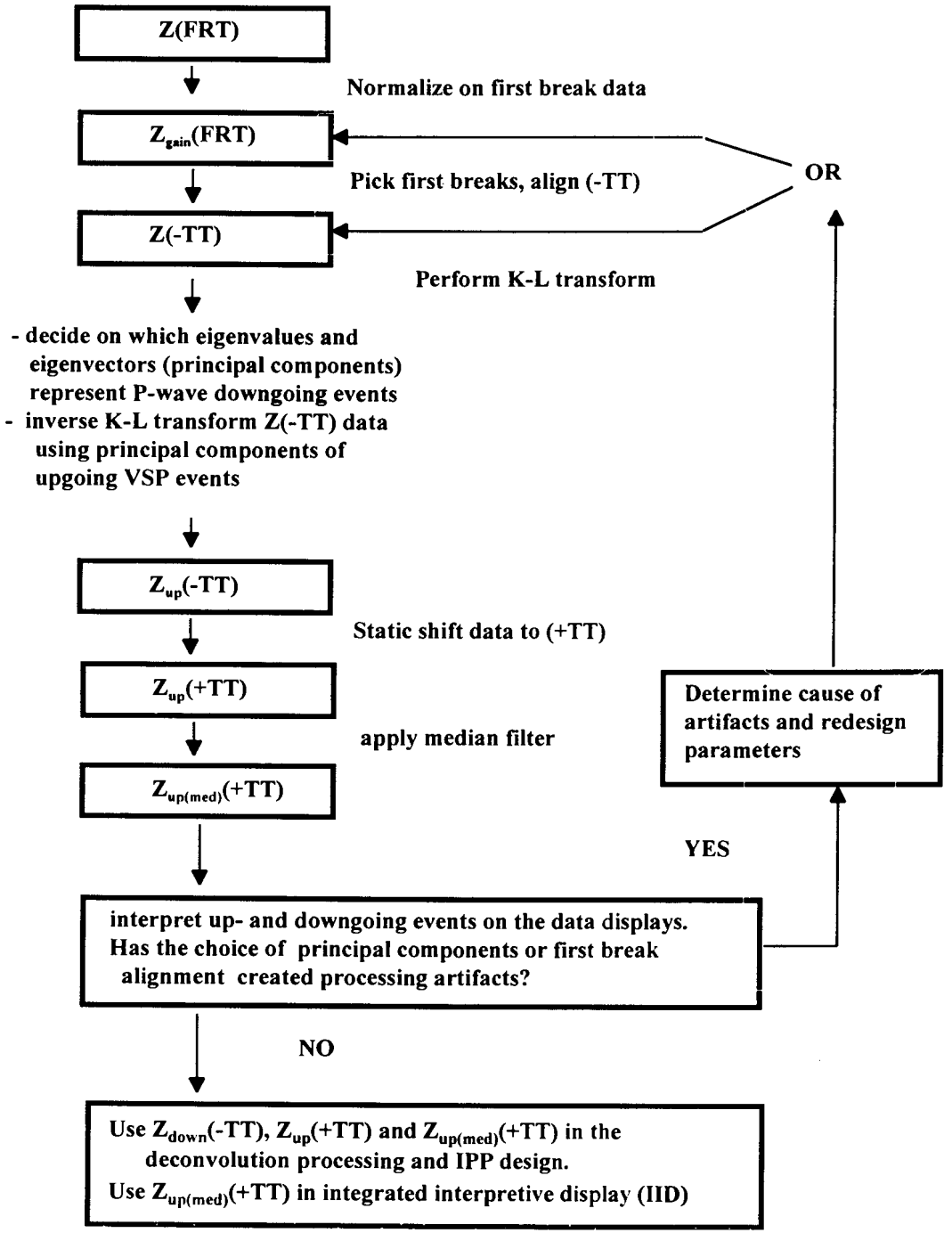

Flowchart 3: An example of the interpretive processing flowchart for the K-L transform wavefield separation processing (Hinds et al., 1994c).

2.2.3.1 Review of the K-L transform

The simplest of assumptions involving the **Z(-TT)** data is that the downgoing P-wave event is horizontally aligned and that the downgoing multiples are time-delayed from the primary downgoing event but are similarly "strictly" horizontally aligned during the **(-TT)** time alignment. This assumption has enabled processors to use the Karhunen-Loeve transform (Hotelling, 1933; Karhunen, 1947; Loeve, 1948, 1955; Watanabe, 1965; Kramer and Mathews, 1956) to selectively evaluate which eigenvectors and eigenvalues are to be used during the data reconstruction (inverse K-L transform) to isolate the upgoing wavefield events (Freire and Ulrych, 1988; Hinds et al., 1986) .

Both the singular value decomposition method (SVD, see Freire and Ulrych, 1988) and the K-L transform use the magnitude of eigenvalues computed through an SVD operation to choose a data reconstruction based on the lateral coherency of the data. Following an eigenanalysis of the autocovariance matrix of the input VSP data (Jackson et al., 1991; Jones and Levy, 1987; Jones, 1985), the largest eigenvalues (Hardage, 1992) will represent the principal components having the greatest amount of coherent energy (Jones and Levy, 1987). The output data are reconstructed using selected principal components (see Appendix). Some of the principal components associated with the largest eigenvalues are not used in the **Z(-TT)** data reconstruction. These principal components are interpreted by the processor to represent the downgoing wave events. Leaving out these principal components during the inverse K-L transform results in the $\mathbf{Z_{up}}$**(-TT)** data.

This method has been used whenever it is possible to isolate data into linearly coherent

versus linearly non-coherent data. In surface seismic processing, multiple attenuation of CDP gathers can be effected by applying NMO using the multiple velocity and then using the K-L transform to reconstruct pre-stack events that are not linearly coherent (Jones, 1985; Jones and Levy, 1987; Hinds and Durrheim, 1993 and 1994). Conversely, the interpreted primary events can be aligned using NMO corrections with the "best" primary velocity function. Following the K-L transform, the principal component data are transformed back into CDP gathers using the principal components reflecting the largest eigenvalues. In VSP processing, the -**TT** downgoing waves are aligned to make the downgoing wavefield data the events that possess the greatest amount of linearly coherent energy (Freire and Ulrych, 1988; Hinds et al., 1986). Following the eigenanalysis, data reconstructed using only the principal components associated with the largest eigenvalues would yield the separated downgoing events. An excellent review of the use of the K-L transform on VSP (and crosswell tomography) data is given in Hardage (1992).

In Jones (1985), it was shown that the application of the K-L transform can preserve the original lateral extent of events as well as separate events based on their linear coherency. This is important whenever one deals with up- and downgoing multiple events. The interpretation of the interbed downgoing multiple depends on showing that the downgoing multiple does not exist on all of the depth traces. The top generating interface (the interface that reflects an upgoing event to create a downgoing multiple event) of the multiple is interpreted as the shallowest trace that the downgoing interbed multiple exists on.

2.2.3.2 K-L filtering and multiple contaminated data

The K-L wavefield separation IPP is displayed in Figure 2.4. Panel 1 displays the data that have been normalized using a calculation window around the primary downgoing event. This normalization of the input data to the SVD step is crucial to the success of the method (Freire and Ulrych, 1988; Hardage, 1992). Another normalization step imbedded in the method can be the normalization of the eigenvalues themselves following the SVD step.

The **Z(-TT)** data are displayed in panel 2. The trace-to-trace amplitude variation of the separated downgoing events, $\mathbf{Z_{down}(-TT)}$, in panel 3 is not seen in the separated downgoing events using the median filter wavefield separation (panel 3 of Fig. 2.1). Panel 3 was constructed using only the first two eigenvalues (related to the first two principal components) created during the K-L transformation. The use of the median filter to separate the downgoing events from the combined wavefield data (section 2.2.2.2) tended to smear and distort downgoing event amplitudes. The K-L separated downgoing events do not require the balancing of the separated downgoing events with the combined wavefield data prior to the subtraction process, $\mathbf{Z_{down}(-TT)}$ from **Z(-TT)**, as much as the median filter based wavefield separation.

By subtracting the data in panel 3 from the **Z(-TT)** data in panel 2, the separated upgoing events, $\mathbf{Z_{up}(-TT)}$ data, are output (panel 4). In panel 5, the $\mathbf{Z_{up}(FRT)}$ data are shown and an enhanced version of panel 5 using a second K-L filter is presented in panel 6. As a comparison, a 5-point median was also used to enhance the upgoing events contained in $\mathbf{Z_{up}(+TT)}$ data and are shown in panel 7. The enhanced upgoing events in panels 6 and 7

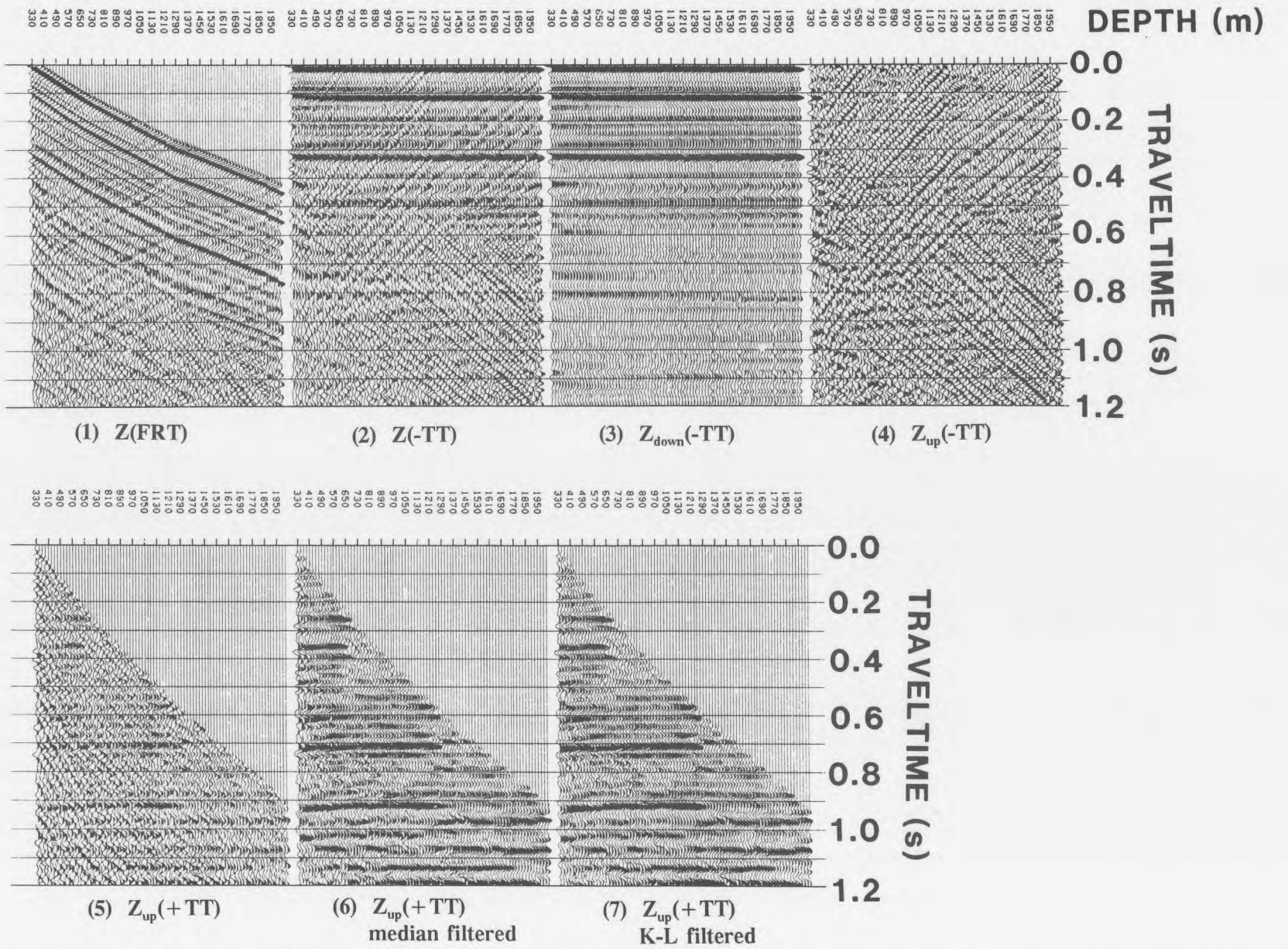

Figure 2.4 Wavefield separation IPP of the Fort St. John Graben case study (Hinds et al., 1993a) data using the K-L filter and subtraction method (Hinds et al., 1986).

are similar (using a 5-point median filter is not a severe application). The primary upgoing event that is embedded in the contaminating multiples appearing beyond the 1210 m depth trace is adequately preserved for interpretation purposes.

The K-L transform method should be used when amplitude preservation is critical and when interbed multiples are being investigated within the separated downgoing events.

2.2.4 2-D Fourier Transform filtering

In this section, the use of F-K domain filtering within the wavefield separation processing will be discussed. In the depth-time domain, the up- and downgoing events cross and interfere with each other; however, the upgoing events in the F-K domain separate from the downgoing events (Hardage, 1985). By attenuating the values of specific portions of the F-K domain representation of the **Z(FRT)** data, the downgoing events can be eliminated from the inverse F-K transformation. The resultant depth-time data, $\mathbf{Z_{up}(FRT)}$, will contain the separated upgoing events. Two types of F-K domain processing are currently available within interpretive processing (Hinds et al., 1994c):

(1) designing the F-K mute parameters, implementing the parameters within a processing runstream and evaluating the F-K domain wavefield separation IPP; and

(2) using interactive screen processing to compare the input and outputs of the F-K filtering step, evaluating the success of the single step of processing and modifying the F-K filtering parameters until any processing artifacts are minimized.

The term "F-K muting" is used to describe the lowering of F-K domain values within a specific mute window (piece of the F-K domain) in order to attenuate the depth-time events that are represented within that F-K mute window. The boundary between the "window" of data designed to be muted and the remainder of the F-K domain data is usually not a sharp cutoff. The difference in values along the F-K boundary of the muted and non-muted F-K data is gradually "sloped" in order to minimize the 2-D version of Gibb's phenomena. Before the introduction of software packages which accepted polygonal definitions of the F-K zones to be muted, two "input" velocity values would specify the familiar pie-slice (velocity filter) mute (Kanasewich, 1981).

2.2.4.1 Review of F-K filtering

The **Z(FRT)** data contain up- and downgoing events that respectively map into the negative and positive quadrants of the F-K domain after 2-D Fourier transformation. A linear event in the depth-traveltime **(FRT)** domain maps as a linear event in the F-K domain. As shown in Hardage(1985), the up- and downgoing P and SV events become separate linear events in the F-K domain.

The relationship between frequency (ω), spatial wavenumber (k_z) and apparent velocity (v) is $\omega = k_z \cdot v$. This means that linear events in the **Z(FRT)** data map into linear events in the F-K domain passing through the F-K domain origin. The slope of the transformed linear events within the F-K domain is equal to the event's apparent velocity in the depth-time domain. Excellent reviews of the F-K domain processing are presented in Hardage (1985, 1992), Hatton et al. (1986), and Yilmaz (1987).

To show the different VSP events in both the depth-time **(FRT)** and F-K domains, the Fort St. John Graben case study near offset **Z(FRT)** data (Hinds et al., 1991a; Hinds et al., 1993a; and Hinds et al., 1994c) are shown in Figure 2.5A and B in the depth-time and F-K domains, respectively. Some of the VSP events within the **Z(FRT)** data are labelled for clarity. The labelled events on Figure 2.5A and B are:

(1) downgoing P-wave events (positive K quadrant);

(2) upgoing P-wave events (negative K quadrants);

(3) downgoing tubewave events; and

(4) upgoing tubewave events.

For the downgoing tubewave events, the non-aliased data are between 0-35 Hz in the positive K quadrant and the aliased energy "wraps around" between 35-60 Hz in the negative K quadrant (Fig. 2.5B). The part of the downgoing tubewave events that contain frequencies above 35 Hz will visually appear to be upgoing events in the depth-time domain due to spatial aliasing. The cause of the aliasing is the choice of depth increments between the VSP

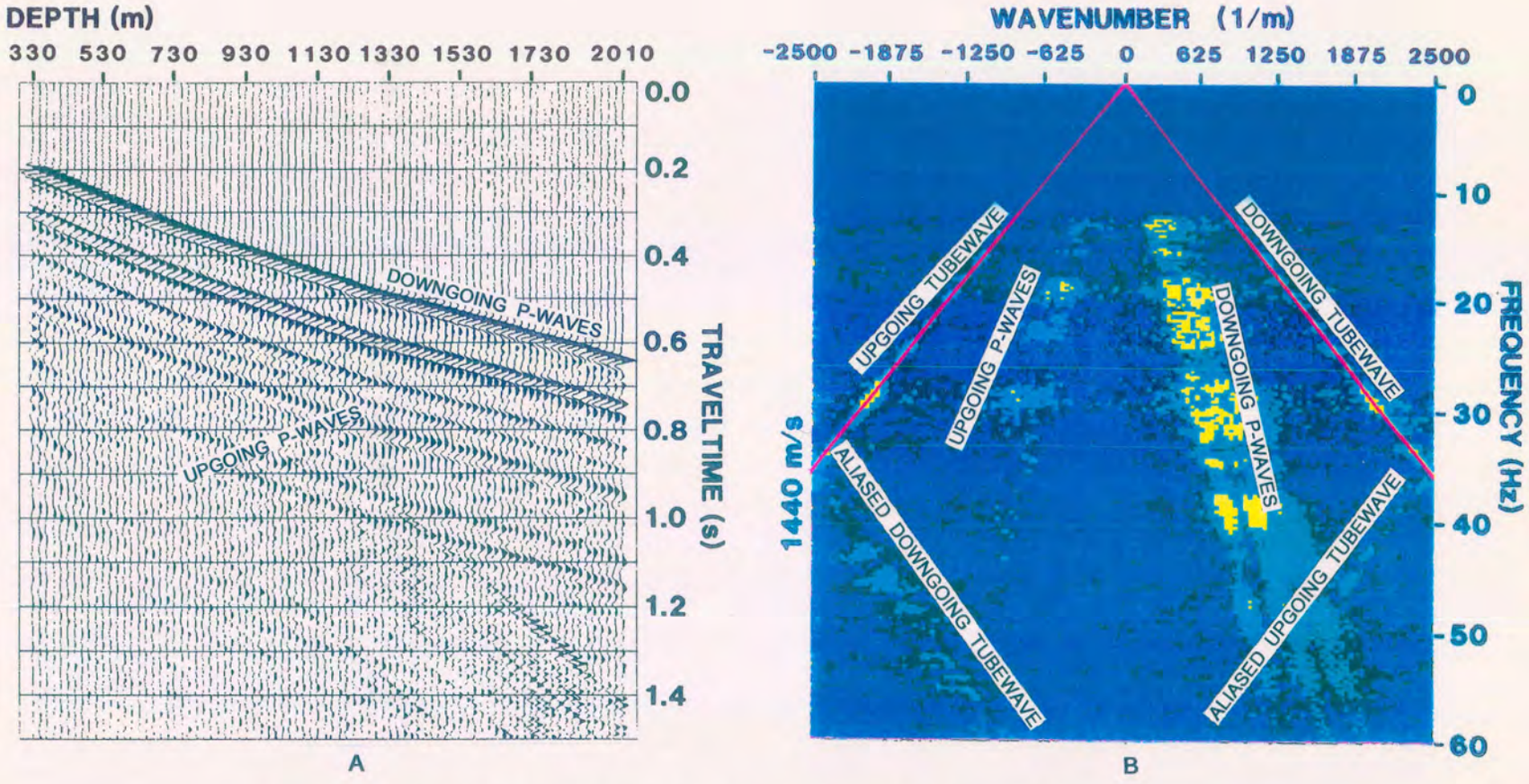

Figure 2.5 Depth-FRT time and F-K domain plots for the Fort St. John Graben case study (Hinds et al., 1993a) near offset data. The up- and downgoing P-wave events separate in the F-K domain. The up- and downgoing tubewave events alias at 35 hz back into the opposite F-K quadrants.

sonde recording levels. Although P-wave events do not appear to "wrap around" in F-K space, the depth recording interval was too coarse to properly record all of the tubewave events for the F-K processing. Similarly, for the upgoing tubewave events, the non-aliased energy is between 0-35 Hz in the negative K quadrant and the aliased energy "wraps around" between 35-60 Hz in the positive K quadrant. An excellent review on tubewave aliasing is given in Hardage (1981).

It can be noted that the aliased downgoing tubewave event intersects the upgoing P-wave events at approximately 55 Hz in the negative K quadrant.

In Figure 2.6, the different types of F-K mutes which will be reviewed in more detail later are shown. The muting procedures used in this thesis are:

(1) F-K quadrant attenuation (the data in one of the K quadrants are muted; Fig. 2.6A);

(2) Polygon or narrow "reject" zone (similar to pie-slice filtering discussed in March and Bailey, 1983) muting (Fig. 2.6B);

(3) Polygon or narrow "accept" zone muting (Fig. 2.6C); and

(4) the interactive polygonal muting (more than one polygon within the F-K domain is specified) shown in Figures 2.6D and E.

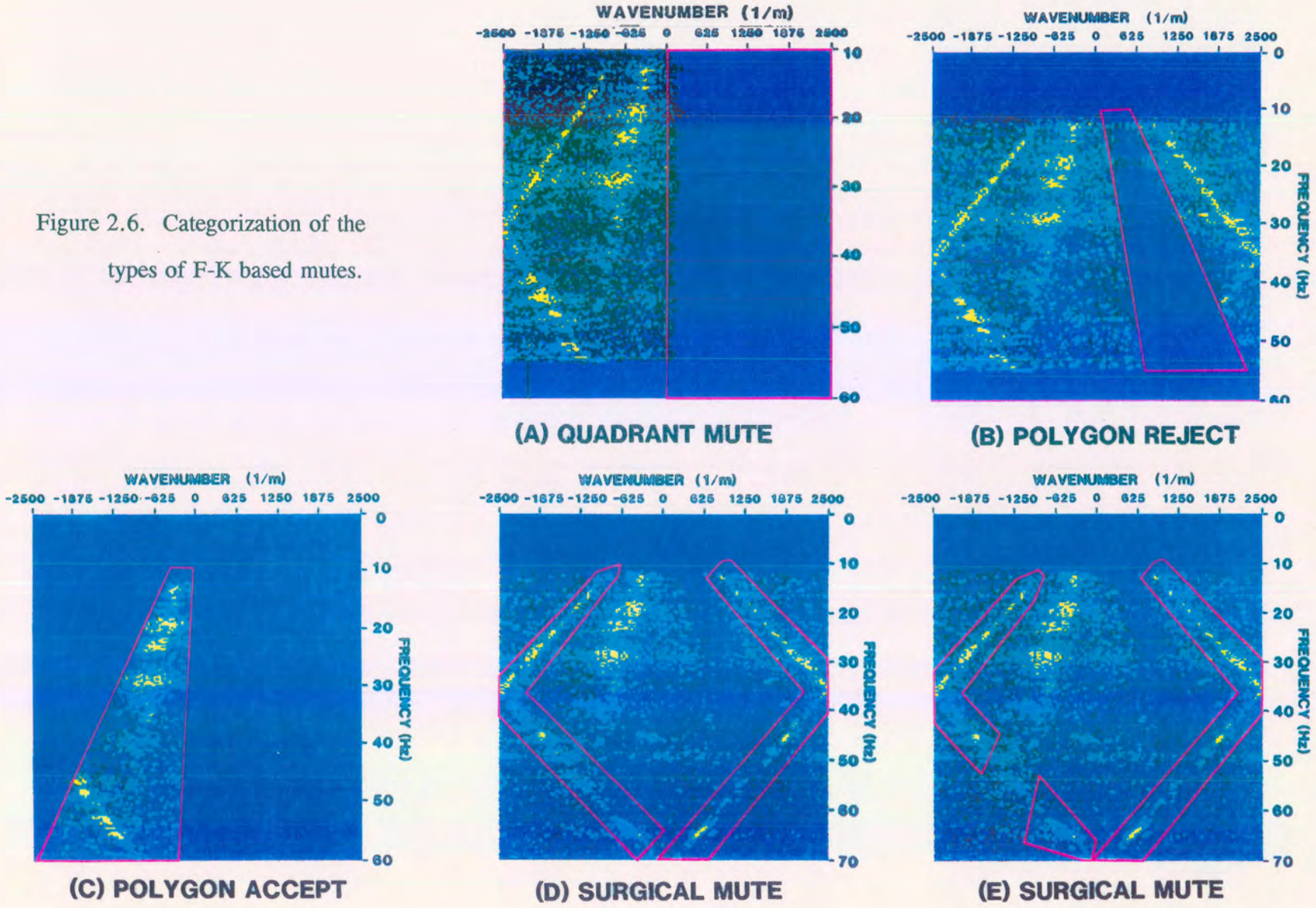

Figure 2.6. Categorization of the types of F-K based mutes.

The interpretation of the separated upgoing events resulting from the use of the different types of F-K filters will be shown below for multiple and tubewave contaminated **Z(FRT)** VSP data. The F-K mute applications will have an effect on the isolation of primary, multiple and tubewave (aliased and non-aliased) events which will be seen using the F-K domain IPP (Hinds et al., 1994c).

2.2.4.2 F-K filtering and multiple contaminated VSP data

The wavefield separation results obtained following the application of various types of F-K filtering on the near offset Fort St. John Graben case study (Hinds et al., 1991a; Hinds et al., 1993a and 1994b; Hinds et al., 1994c) multiple contaminated **Z(FRT)** VSP data are shown in Figures 2.7 through 2.13. By examining the suite of resultant $\mathbf{Z_{up}(FRT)}$ data in the depth-time domain, interpretation problems caused by the F-K filtering methods can be investigated. The input **Z(FRT)** data and corresponding F-K plot are presented in panel 1 of Figure 2.7 and Figure 2.8, respectively. The horizontal axis on Figure 2.8 is the wavenumber axis labelled with negative and positive spatial frequencies. The spatial frequencies are in units of 1/m and the labelled values have been multiplied by 10^5 for diagram clarity. The vertical axis is the frequency axis with values in hertz (Hz).

The dominant VSP events represented in the F-K plot of Figure 2.8 are the downgoing P waves shown in the positive K (wavenumber) quadrant. The downgoing tubewave within the depth-time domain appears in panel 1 of Figure 2.7 as the highlighted dispersive wavetrain emerging on the 1310 to 1650 m traces at 1.2 s (**FRT**). On the F-K plot of Figure 2.8, the

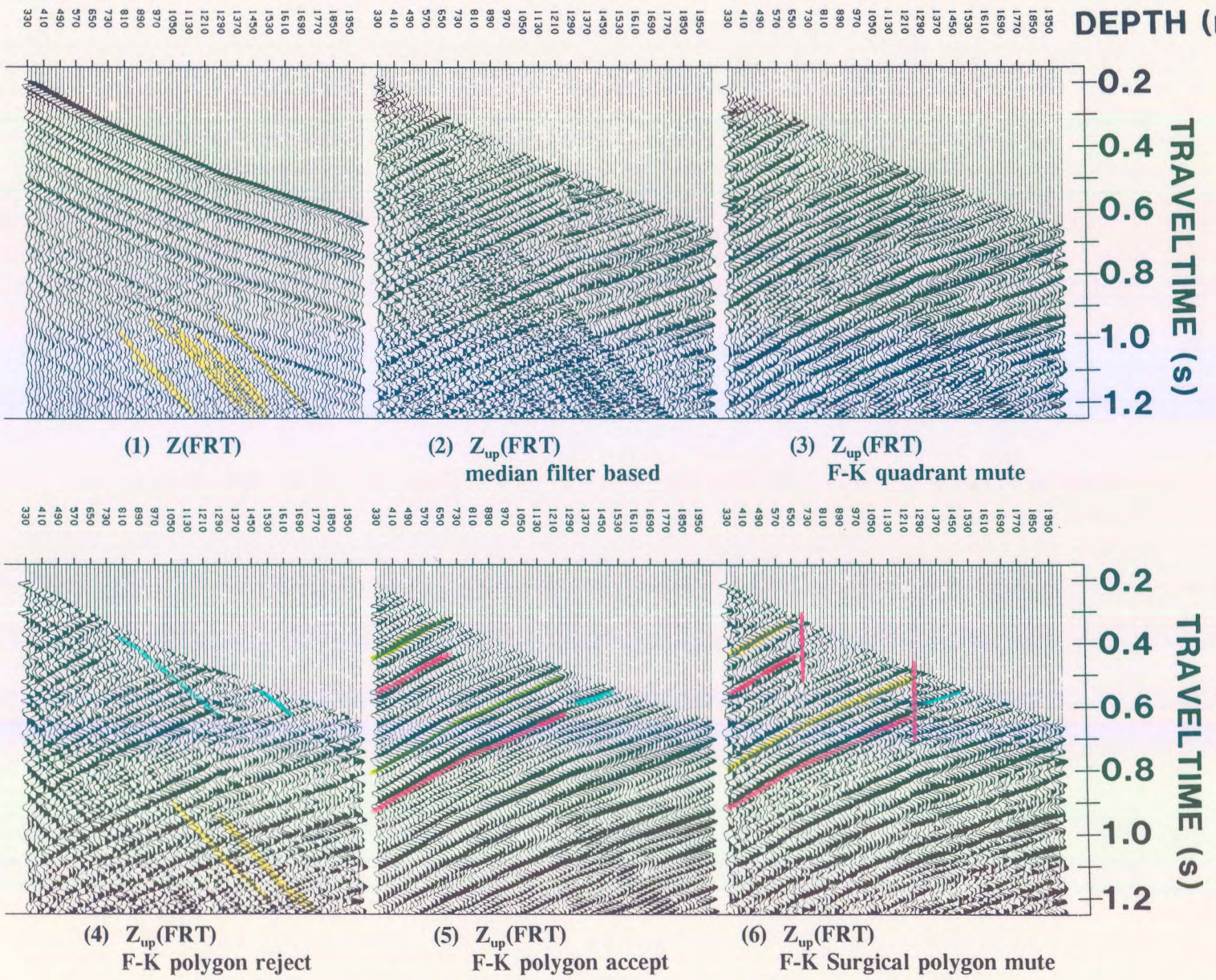

Figure 2.7 **Z(FRT)** and $\mathbf{Z_{up}(FRT)}$ data wavefield separated using the median filter and various F-K operations for the Fort St. John Graben data (Hinds et al., 1993a) near offset multiple contaminated data. The mute designs are shown in Figure 2.6.

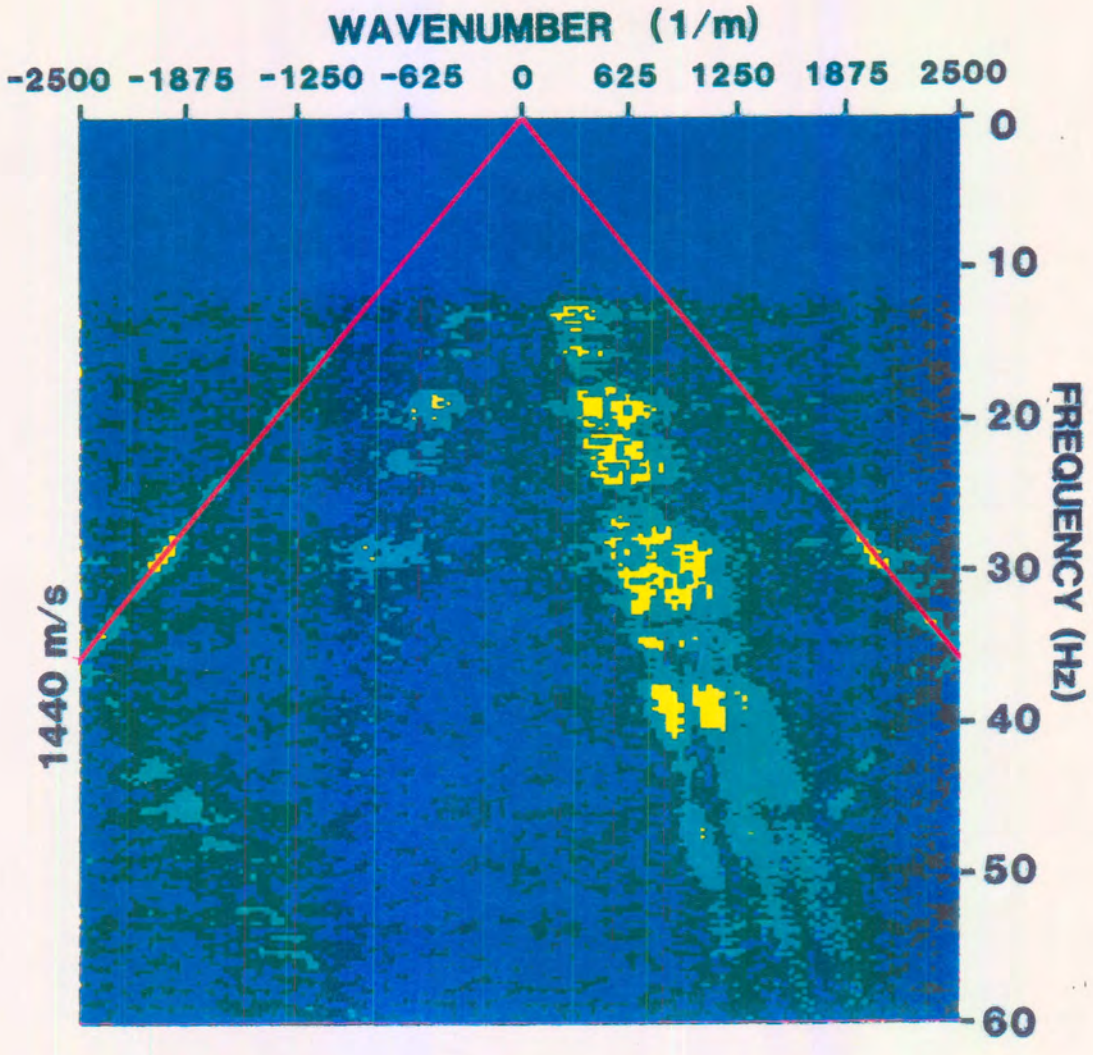

Figure 2.8 F-K plot of the **Z(FRT)** Fort St. John Graben case study data (Hinds et al., 1993a) shown in panel 1 of Figure 2.7. The annotated red lines define the slope (velocity) of the up- and downgoing tubewave F-K events. Note that the tubewave events alias back into the oppositely-signed F-K quadrants after the linear events exceed the Nyquist K (spatial) frequencies.

downgoing tubewave F-K trend in the positive K quadrant has a slope of approximately 1440 m/s. The unaliased portion is comprised of the F-K amplitudes along a linear trend which starts at the F-K origin and ends at a frequency of 35 Hz and a wavenumber value of 2500 ($*10^{-5}$) m^{-1}. The unaliased portions of both the up- and downgoing tubewave events are highlighted in red in Figure 2.8. The "wrap around" occurs at the positive (for downgoing) and negative (for upgoing) Nyquist spatial frequency of $1 / 2 \Delta z$ (= -1/40 m = 0.025 m^{-1}). The "wrapped around" parts of the aliased tubewave have been described above.

There is an upgoing tubewave event resulting from the reflection of the downgoing tubewave at the bottom of the borehole (not shown in panel 1 of Fig. 2.7 since only 1.3 s of the original 3 s of data have been plotted). This upgoing tubewave event is seen unaliased in the negative F-K quadrant from 0 to 35 Hz and the aliased portion "wraps back" into the positive F-K domain at higher frequencies. The aliased downgoing tubewave F-K events intersect the upgoing P-wave F-K events at 55-60 Hz in the negative F-K quadrant; however, the bulk of the upgoing P-wave energy resides at lower frequencies.

The median filter wavefield separation result is shown in panel 2 of Figure 2.7 and is used for comparison with the F-K filtering based wavefield separation results of panels 3 to 6. The downgoing tubewave event in the $\mathbf{Z_{up}(FRT)}$ data of panel 2 are not appreciably attenuated. An F-K plot (Fig. 2.9) of the $\mathbf{Z_{up}(FRT)}$ data in panel 2 shows that only a narrow zone immediately around the downgoing P-wave display has been attenuated. Any attenuated downgoing tubewave data in panel 2 of Figure 2.7 would a result of the application of a post-median filter bandpass filter applied to eliminate the median filter "whiskers" (Hardage, 1985).

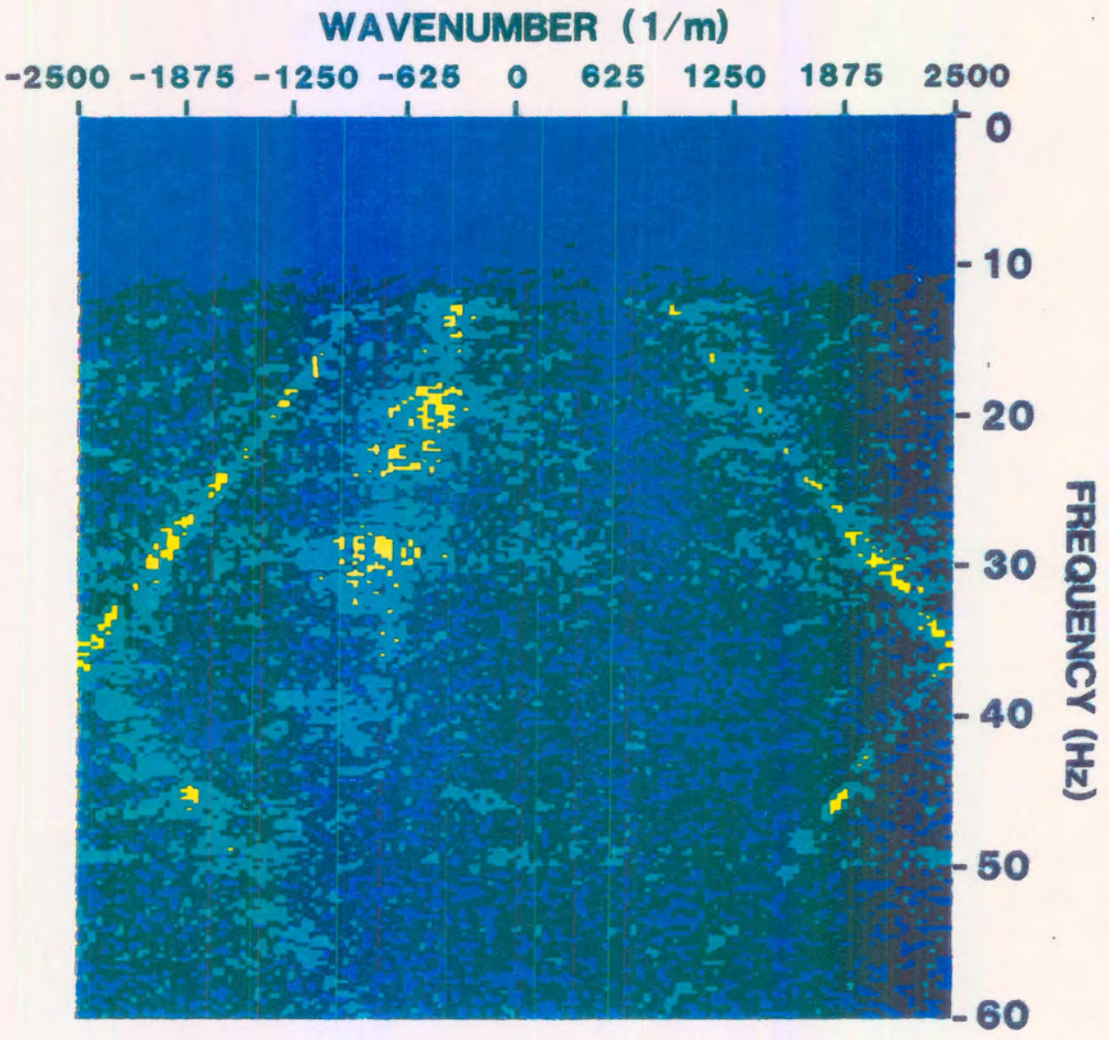

Figure 2.9 F-K plot of the median filter and subtraction method derived $\mathbf{Z_{up}(FRT)}$ data (shown in panel 2 of Figure 2.7). The method has rejected the downgoing P-wave events; however, the up- and downgoing tubewave F-K events are relatively unaffected.

Panel 3 of Figure 2.7 displays the result of the simplest and most commonly used type of F-K filtering; namely the masking of the entire positive K quadrant. To evaluate the effect of the F-K quadrant elimination processing on the **Z(FRT)** data (panel 1 of Fig. 2.7), the F-K plot of the **Z(FRT)** data (Fig. 2.8) can be compared to the F-K plot of the $\mathbf{Z_{up}(FRT)}$ data in panel 3 of Figure 2.7 (F-K plot shown in Fig. 2.10). The downgoing tubewave frequency content below 35 Hz has been attenuated in Figure 2.10; however, the aliased downgoing tubewave (appearing between 36-60 Hz) and the unaliased parts of the upgoing tubewave (between 0-35 Hz) will remain in the $\mathbf{Z_{up}(FRT)}$ data. There is a band of energy associated with a broad k_z range centred at 30 Hz in Figure 2.7 which may be sonde resonance.

In panel 4 of Figure 2.7, the result of attenuating the content of a surgical F-K mute polygon zone around the downgoing P-wave F-K events is shown. The F-K mute zone is highlighted in the F-K domain plot (shown in Fig. 2.11) of the $\mathbf{Z_{up}(FRT)}$ data of panel 4 (Fig. 2.7). Downgoing mode-converted shear waves are retained in the $\mathbf{Z_{up}(FRT)}$ data and are highlighted (in blue) on panel 4. The downgoing mode-converted shear wave events (shown in blue on panel 4) display a similar dip or apparent velocity to that of the downgoing tubewave events (displayed in yellow on panel 4). The upgoing mode-converted shear wave events would plot between the region of the upgoing P-wave and tubewave events in the F-K domain. From an inspection of panel 4 of Figure 2.7, the bulk of the mode-conversions occur at the 690-730 m interface. The surgical mute zone seen in the F-K plot of Figure 2.11 does not encompass the tubewave and mode-converted SV-wave events within the F-K domain resulting in the appearance of these events in the $\mathbf{Z_{up}(FRT)}$ data after the surgical mute wavefield separation procedure.

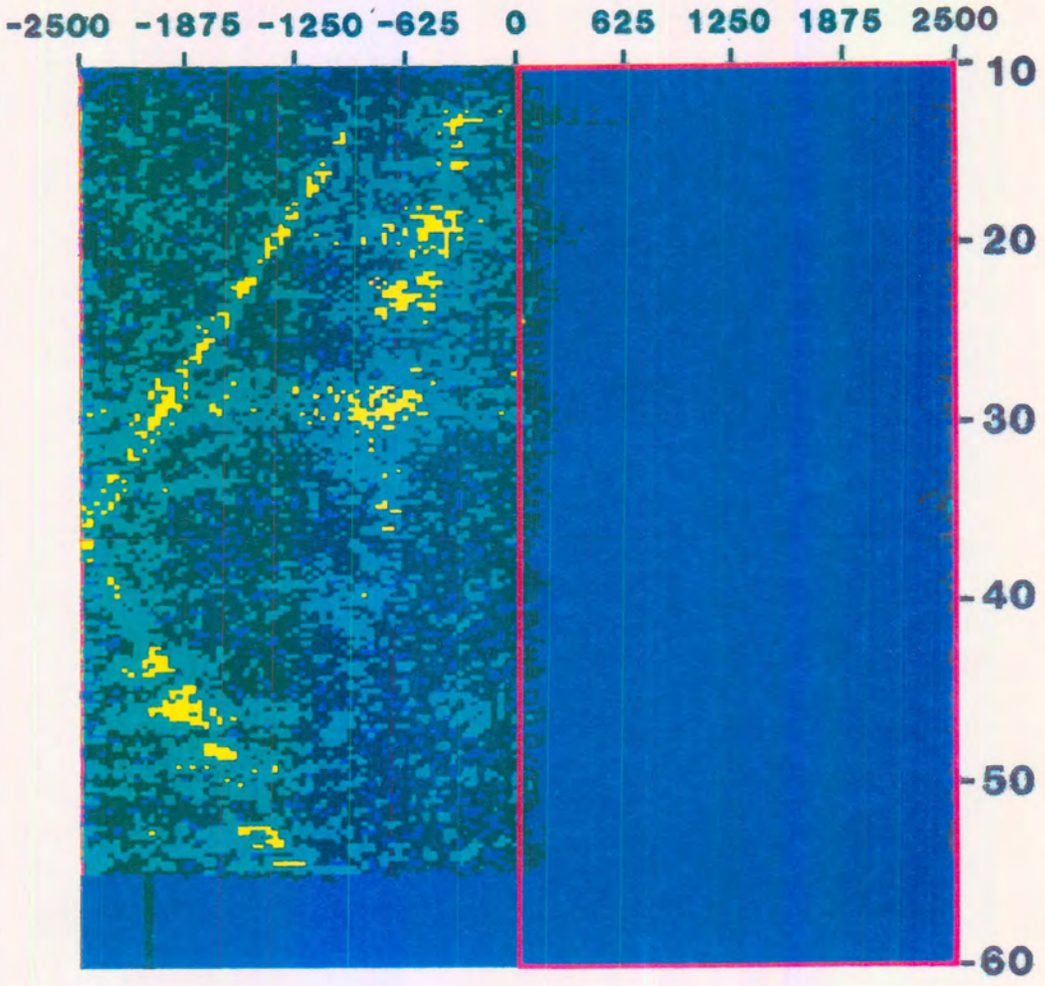

Figure 2.10 F-K plot of the $\mathbf{Z_{up}(FRT)}$ data shown in panel 3 of Figure 2.7. The positive spatial wavenumber (K) quadrant has been attenuated. The upgoing and aliased downgoing F-K tubewave events have not been attenuated since these events exist in the retained negative K quadrant.

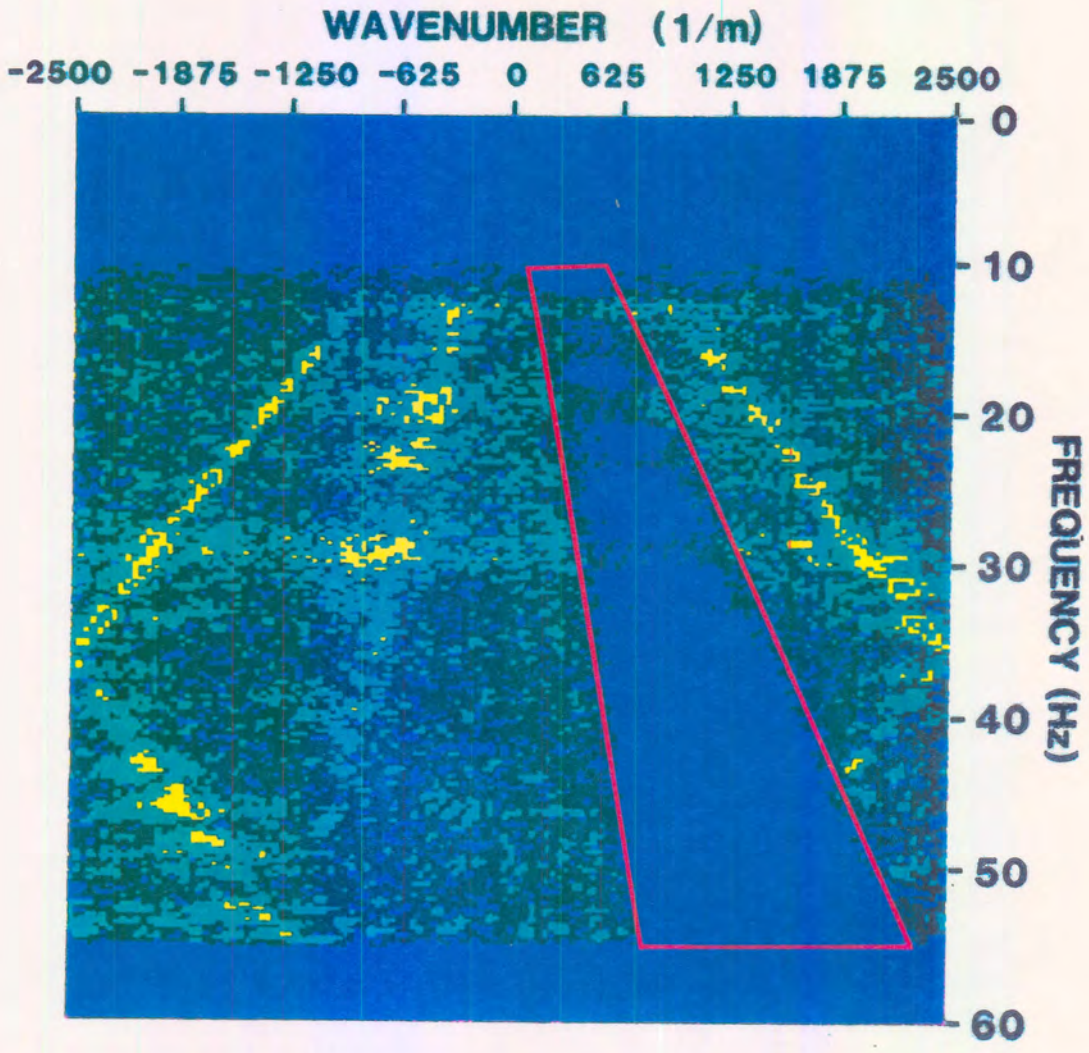

Figure 2.11 F-K plot of the $\mathbf{Z_{up}(FRT)}$ data shown in panel 4 of Figure 2.7. A spatially limited reject polygon has been used to attenuate the downgoing P wave F-K events. The applied mute does not appreciably affect the up- and downgoing tubewave F-K events.

The results of applying a "narrow accept" F-K mute filter to the **Z(FRT)** data are shown in the $\mathbf{Z_{up}(FRT)}$ data in panel 5 of Figure 2.7. The F-K response showing the highlighted boundaries of the zone within the F-K domain which was retained is displayed in Figure 2.12. The $\mathbf{Z_{up}(FRT)}$ data in panel 5 resulting from the use of the narrow accept F-K muting within the wavefield separation processing is a visual example of Rieber mixing as explained in Hardage (1985). The narrow range of spatial frequencies in the F-K pass zone results in a broad expression of the events in the depth-time domain (also termed F-K smearing).

This can be seen by examining the Spirit River and Nordegg Formation primary and multiple events. The events of the $\mathbf{Z_{up}(FRT)}$ resultant data shown in panel 5 (Fig. 2.7) are smeared and the Spirit River multiple (coloured red) event does not truncate sharply at the 690-710 m traces. The Spirit River primary event has been coloured green in panel 5. Amplitude preservation from trace to trace has not been accomplished due to the Rieber mixing. Another example is the primary event (shown in blue) imbedded in the zone of multiples (colored orange) originating from the 1250 m interface (Nordegg Formation) is barely distinguishable as a separate event. The multiple and primary event have been highlighted in panel 5. The cursor in Figure 2.12 is placed at the intersection of the aliased downgoing tubewave and the upgoing P-wave events.

The application of the surgical F-K mute polygon "reject zones" to the **Z(FRT)** data results in the $\mathbf{Z_{up}(FRT)}$ data shown in panel 6 of Figure 2.8. The surgical F-K mutes are highlighted in red within the F-K plot shown in Figure 2.13. The surgical mutes were designed to attenuate the downgoing P-wave and the up- and downgoing tubewave events. Two examples of the lateral truncation of the multiples below their respective primaries are

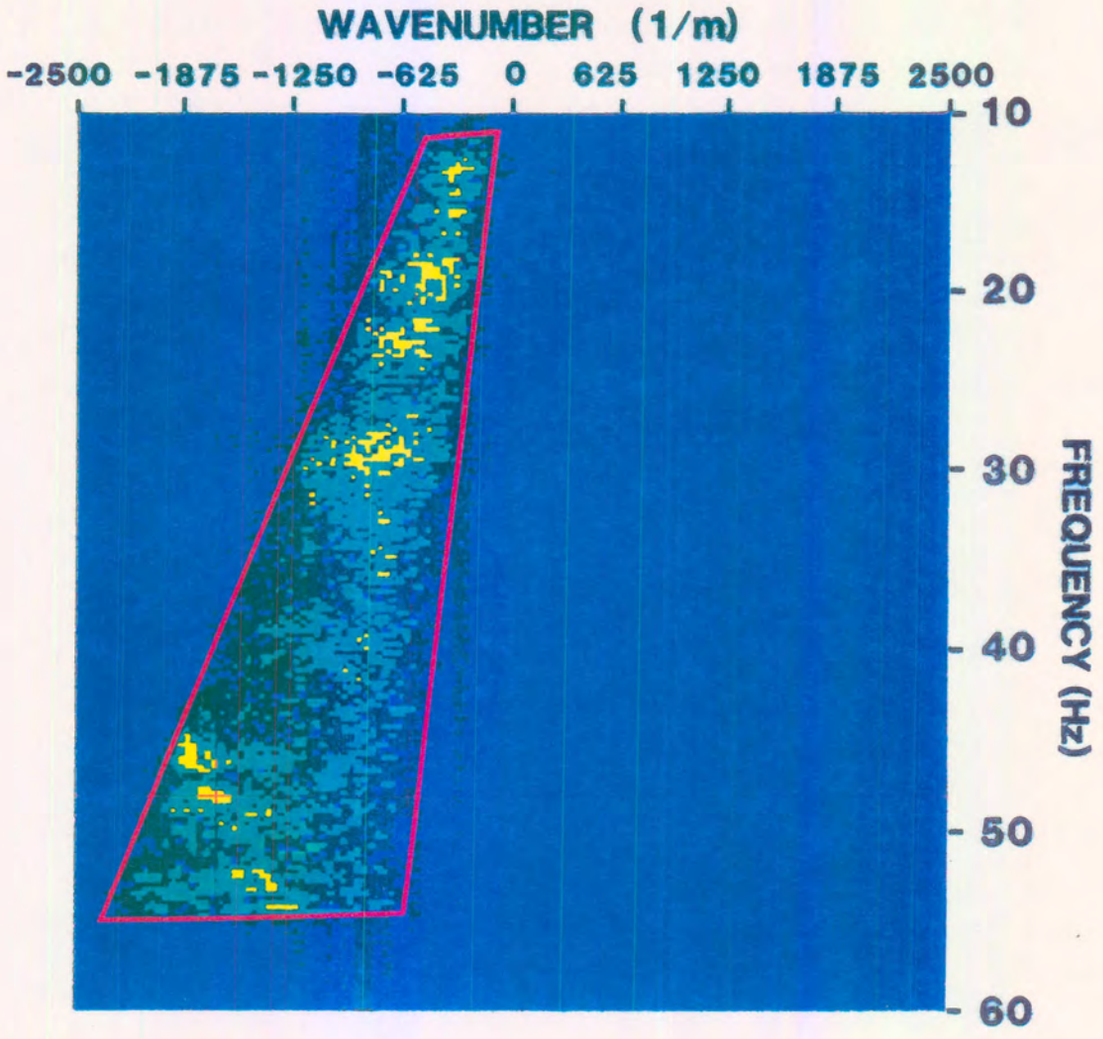

Figure 2.12 F-K plot of the $\mathbf{Z_{up}(FRT)}$ data shown in panel 5 of Figure 2.7. A spatially limited F-K accept polygon has been used to isolate and retain the upgoing P wave F-K events. Due to the spatially narrow accept zone, the filtering results in Reiber mixing in the depth-time domain.

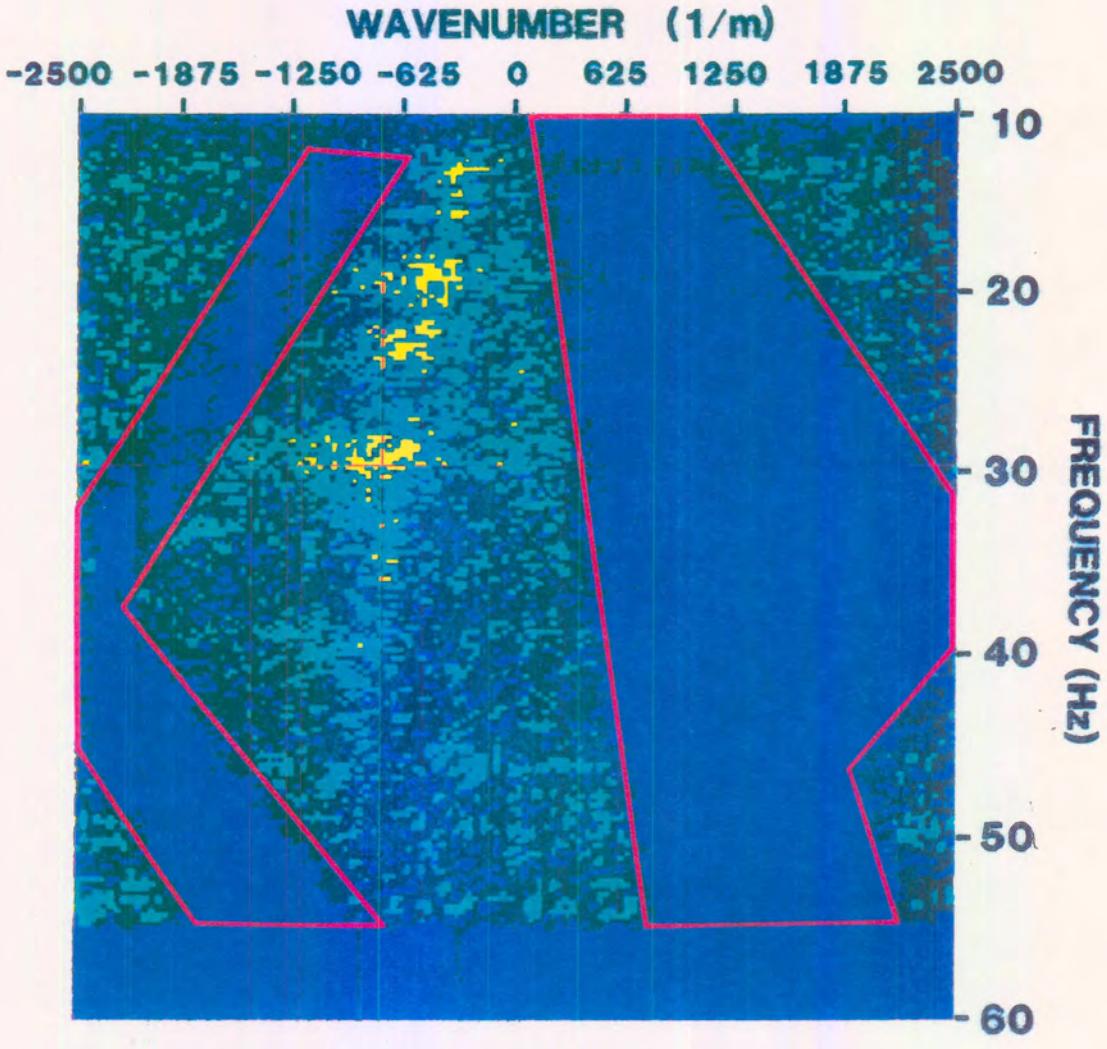

Figure 2.13 F-K plot of the $\mathbf{Z_{up}(FRT)}$ data shown in panel 6 of Figure 2.7. F-K polygons outlined in red show the surgically muted reject zones in the F-K domain designed to attenuate the downgoing P wave F-K events and the aliased and non-aliased tubewave F-K events.

shown in panel 6 of Figure 2.7. The primaries are highlighted in yellow and the multiple events are shown in red. The multiple events are not smeared onto traces beyond the depths where the primary events associated with the multiples were generated. To illustrate this, a vertical line in pink has been drawn for both sets of primaries and multiples showing the lateral extent of the events. The surgical F-K muting has attenuated both the downgoing P and up- and downgoing tubewaves and has succeeded in preserving the trace-to-trace amplitude variations (as was done for the median filtered $\mathbf{Z_{up}(FRT)}$ data shown in panel 2).

The acceptable types of F-K filtering for the multiple contaminated data shown in panel 1 of Figure 2.7 (the near-offset data from the Fort St. John Graben case study; Hinds et al., 1991a; Hinds et al., 1993a and 1994b; Hinds et al., 1994c) would appear to be the F-K quadrant attenuation (Fig. 2.10) and the surgical F-K muting (Fig. 2.13). What is of concern in the interpretive processing of multiple contaminated data is the lateral truncation of the multiple events and the trace-to-trace amplitude preservation.

2.2.4.3 F-K filtering and tubewave contaminated VSP data

In this section, the interpretive processing panel (IPP) for the F-K based wavefield separation procedure will be introduced using tubewave contaminated **Z(FRT)** data. The two IPP's shown below will result from the use of:

(1) surgical F-K domain mutes (Fig. 2.14);

(2) the attenuation of the positive F-K quadrant (Fig. 2.15).

The tubewave contaminated **Z(FRT)** data are shown in panel 1 of the IPP in Figure 2.14. The normalized **Z(FRT)** data contains a dominant aliased downgoing tubewave. The tubewave is highlighted in yellow in panel 1. Panel 2 contains the $\mathbf{Z_{up}(FRT)}$ data resulting from the use of the median filter based separation method (Fig. 2.2). The upgoing wave data highlighted in red in panel 2 are low in amplitude in comparison to the tubewave amplitude shown in yellow. Panel 3 contains the $\mathbf{Z_{up}(FRT)}$ data resulting from the application of surgical muting in the F-K domain which was designed to suppress the downgoing and tubewave events. The aliased downgoing tubewave F-K events which intersected the upgoing P-wave events in the F-K domain were not included in the surgical mute design. The $\mathbf{Z_{up}(+TT)}$ and median filter (3 point) enhanced $\mathbf{Z_{up}(+TT)}$ data are shown in panels 4 and 5, respectively. The upgoing events in the data are easily recognizable after the use of F-K surgical muting wavefield separation.

The IPP for the F-K based wavefield separation method which mutes the positive F-K

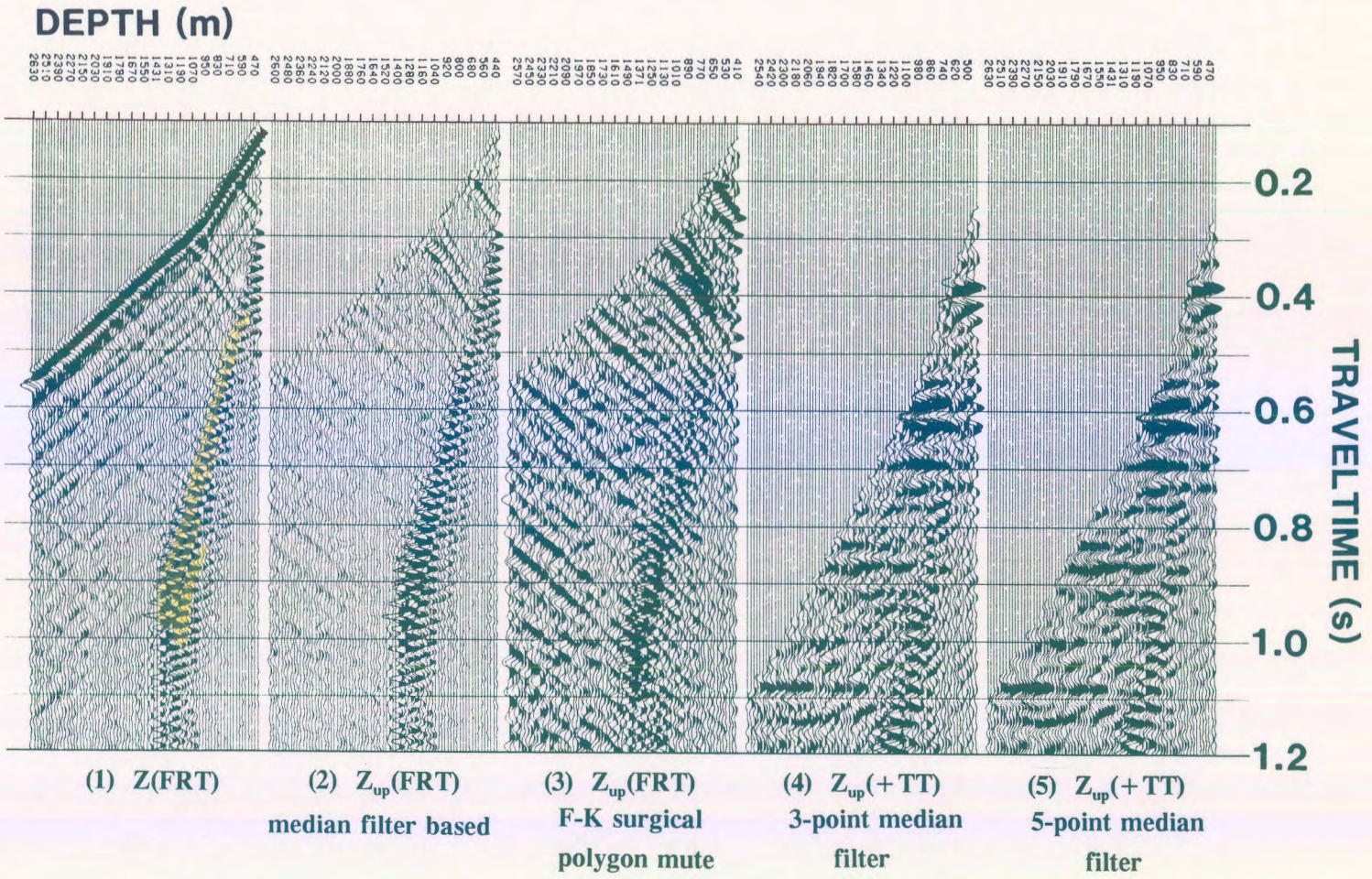

Figure 2.14 F-K based wavefield separation IPP of the tubewave contaminated data using surgical muting of both the downgoing P-wave and tubewave F-K events. Panel 2 is **Z_{up}(FRT)** data resulting from the median filter and subtraction wavefield separation (included for comparison purposes).

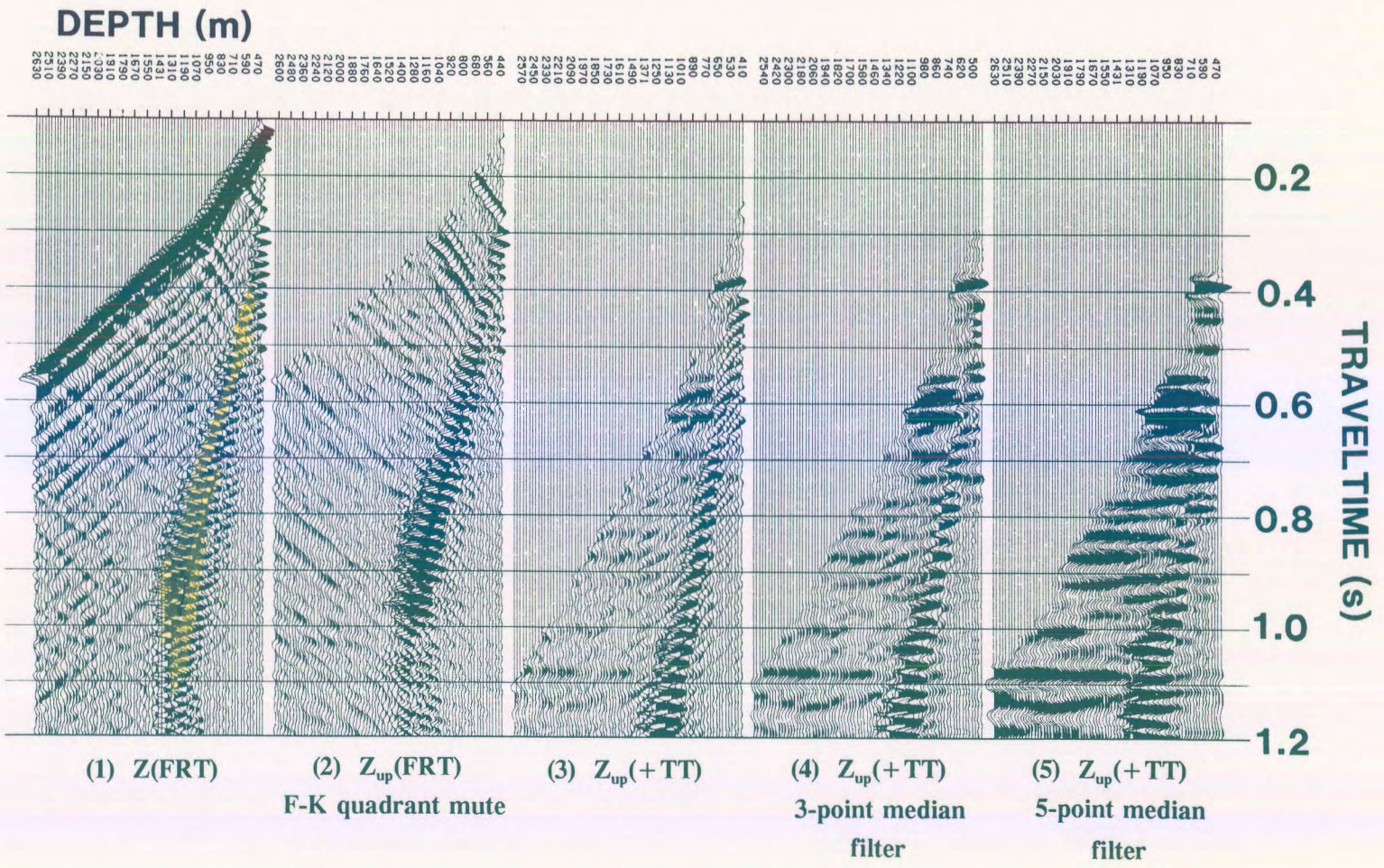

Figure 2.15 F-K based wavefield separation IPP of the tubewave contaminated data using F-K quadrant attenuation.

quadrant (containing the downgoing wave events) is shown in Figure 2.15. The $\mathbf{Z_{up}(FRT)}$ data shown in panel 2 contains the aliased downgoing tubewave events (that appear as upgoing events). The $\mathbf{Z_{up}(+TT)}$ data are shown in panel 3. The $\mathbf{Z_{up}(+TT)}$ data were median filtered using 5- and 11-point median filters and respectively displayed in panels 4 and 5. The quadrant attenuation F-K filtering of the tubewave contaminated data (panel 1) does not solve the problem of the elimination of the aliased tubewave.

This can be seen by comparing the $\mathbf{Z_{up(med)}(+TT)}$ data in panel 5 of Figure 2.14 to the $\mathbf{Z_{up(med)}(+TT)}$ data of panel 5 of Figure 2.15. The tubewave event has been better attenuated using the F-K surgical muting processing shown in the IPP of Figure 2.14.

The results of wavefield separation of the tubewave contaminated **Z(FRT)** using the various F-K filtering methods are shown in Figure 2.16. The tubewave contaminated **Z(FRT)** data are shown in panel 1 (Fig. 2.16). The $\mathbf{Z_{up}(FRT)}$ data shown in the remainder of the panels of Figure 2.16 result from the median filter based wavefield separation method (panel 2), F-K quadrant attenuation (panel 3), narrow F-K reject zone muting (panel 4), narrow F-K accept filter muting (panel 5) and surgical F-K muting (panel 6). The IPP in Figure 2.16 has been designed to enable the evaluation of the different types of F-K filtering wavefield separation methods and the median filter method. The surgical muting method resulting in the $\mathbf{Z_{up}(+TT)}$ data in panel 6 is the optimum method to be used to enhance the interpretation of the upgoing events. The upgoing events must still be interpreted bearing in mind the tubewave event interference in the upgoing P-wave events. The surgical muting has preserved the upgoing events and has successfully attenuated both the up- and downgoing tubewave (aliased and non-aliased parts) during the wavefield separation procedure.

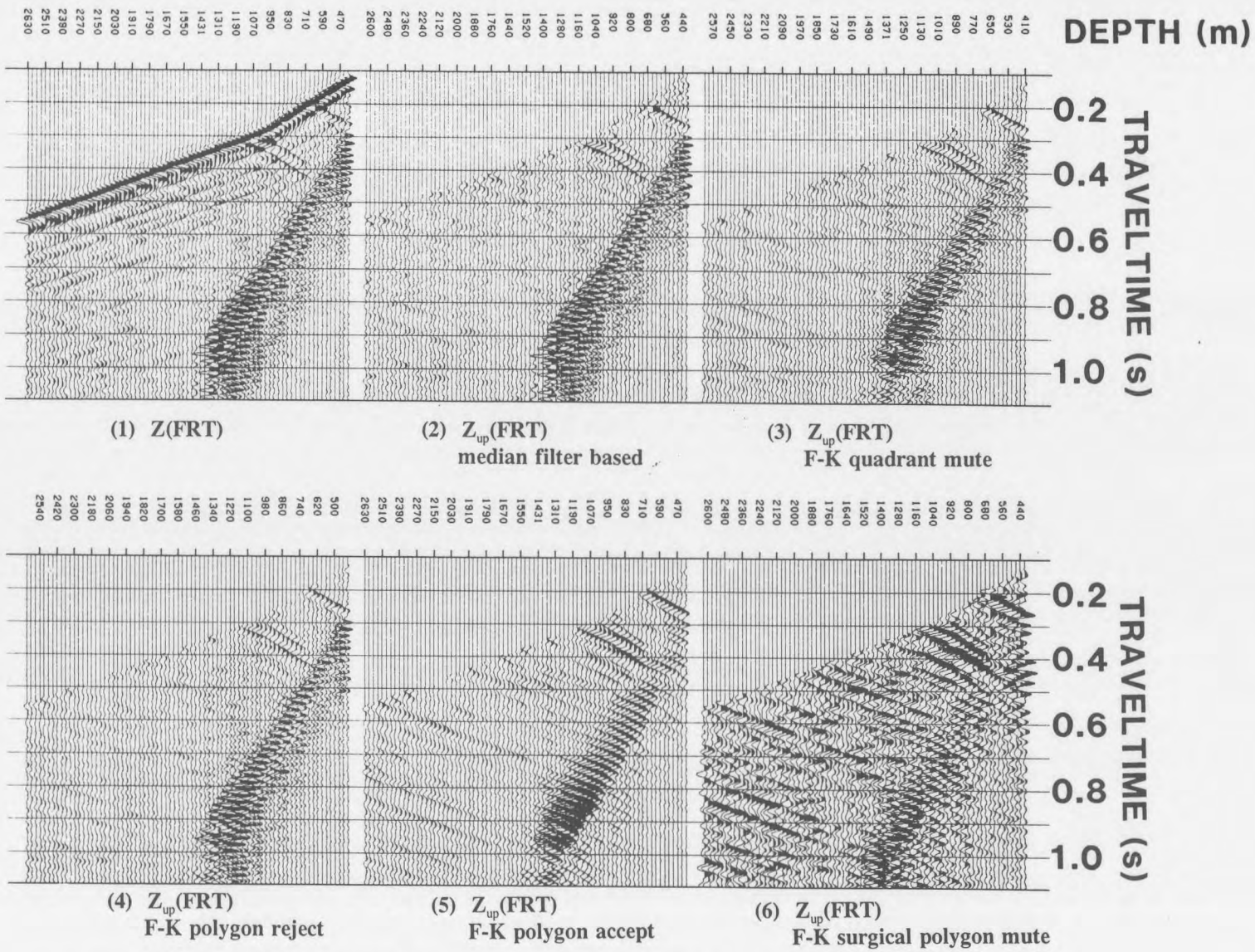

Figure 2.16 **Z(FRT)** (panel 1) and $\mathbf{Z_{up}(FRT)}$ wavefield separated data using the median filter plus subtraction method (panel 2) and the various F-K muting methods (panels 3-6) on the **Z(FRT)** tube wave contaminated data.

2.2.4.4 F-K filtering in other wavefield separation methods

In section 2.2.2.3, the median filter based wavefield separation of the tubewave contaminated **Z(FRT)** data was reviewed. In panels 6 and 7 of Figure 2.2, the $\mathbf{Z_{up}(+TT)}$ data resulting from the use of the median filter are shown. Surgical F-K muting was applied to the $\mathbf{Z_{up}(FRT)}$ following the median filter wavefield separation and these F-K filtered data are shown in panel 8 of Figure 2.2. Figure 2.17 is the F-K plot of the resultant data. The surgical mute used during the filtering was designed to attenuate the tubewave; however, the muted zone of the F-K domain did not include the portion of the aliased tubewave which intersected the upgoing P-wave F-K events.

This is an example of how the F-K filter surgical muting can be combined with other wavefield separation methods.

2.2.4.5 F-K filtering using interactive screen processing

In this section, interactive screen processing will be shown for surgical mute processing in the F-K domain. These examples will illustrate the single step interpretive processing. The input data are shown on one of the bit planes of the interactive monitor display. A bit plane is one of the screen displays within modern graphics systems that can be chosen for display using mouse or keyboard commands. On another bit plane, the F-K domain plot of the input data is displayed and mute zones are interactively chosen within the F-K plot. The result of applying the F-K mutes to the input data is then displayed on yet another bit plane. By

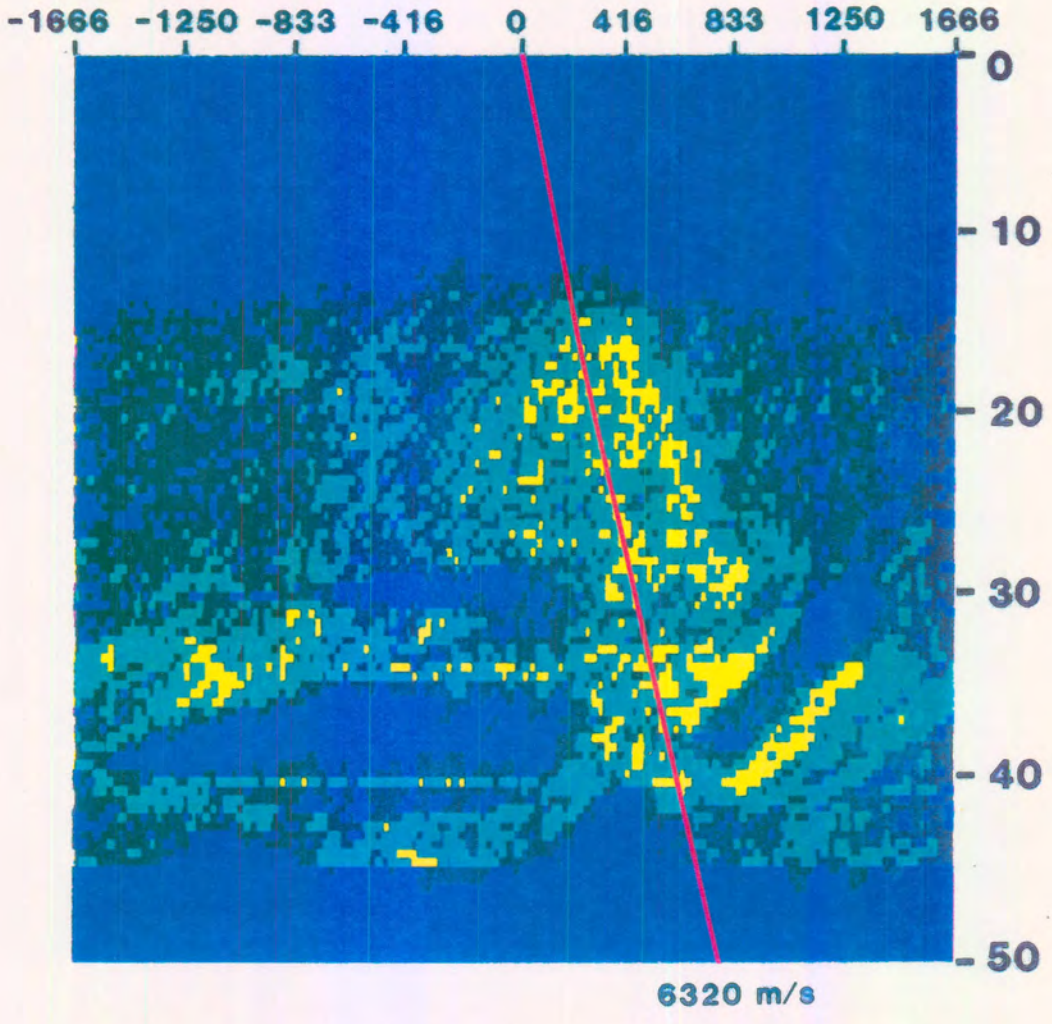

Figure 2.17 F-K plot of data resulting from the application of F-K surgical muting to the median filter-based wavefield separation results (prefiltered data is shown in panel 6 of Figure 2.2). The depth-time equivalent of the displayed F-K data is shown in panel 8 of Figure 2.2.

comparing the input and F-K filtered data, the effect of the application of the surgical muting on interpretation can be evaluated. Once any F-K filtering induced artifacts are minimized, the current F-K mute parameters are then output for use in the wavefield separation runstream.

The two examples will use interactive F-K filtering to:

(1) interpret up- and downgoing event content on **Z(FRT)** data; and

(2) enhance $\mathbf{Z_{up}(FRT)}$ data.

2.2.4.5.1 Using interactive F-K filtering to wavefield separate

The processing decisions used in the wavefield separation by interactive F-K processing are shown in Flowchart 4. The **Z(FRT)** data of the near offset VSP survey of the Fort St. John Graben case study (Hinds et al., 1991a; Hinds et al., 1993a and 1994b; Hinds et al., 1994c) are shown in Figure 2.18. The F-K transformed plot of the same data is shown in Figure 2.19. A surgical F-K polygonal mute zone is designed using on-screen menu commands. The designed mute zone is highlighted in red in Figure 2.19. The F-K data within the mute zone can either be "rejected" (left out of the inverse F-K transformation) or "accepted" (the F-K data outside of the polygonal mute zone is not used in the inverse transform). The resultant $\mathbf{Z_{up}(FRT)}$ data that results from choosing the "rejection" mode is shown in Figure 2.20. The resultant data are plotted onto another bit-plane within the graphics system.

FLOWCHART - Interactive F-K processing (for up- and downgoing event identification)

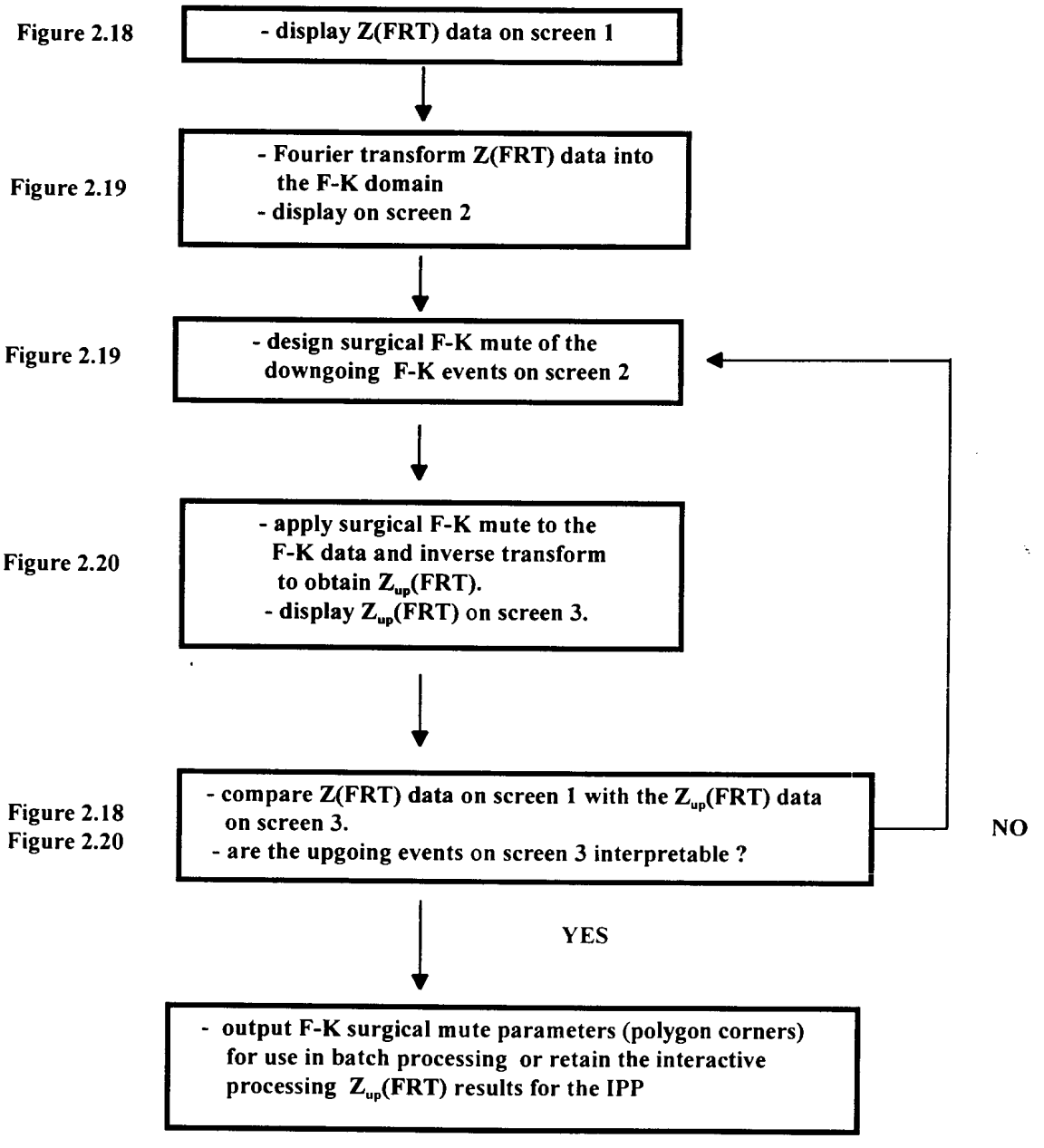

Flowchart 4: An example of the interpretive processing flowchart of the interactive F-K processing used for event identification (Hinds et al., 1994c).

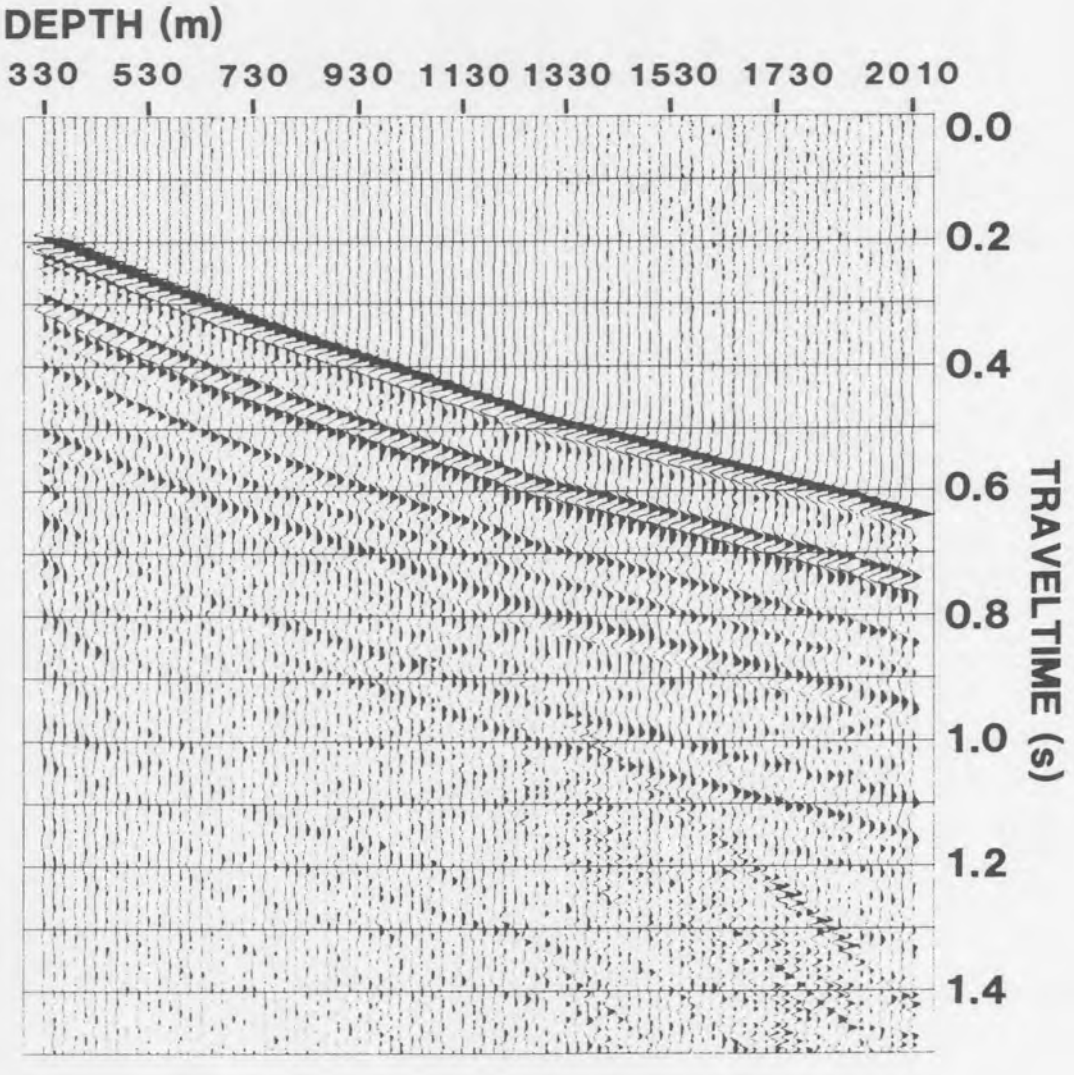

Figure 2.18 Single operation interpretive processing initial screen display showing the input **Z(FRT)** data of the Fort St. John Graben case study (Hinds et al., 1993a). The objective of the interactive processing (seen in Figs. 2.18 to 2.20) is to understand the different types of up- and downgoing wave events within the data.

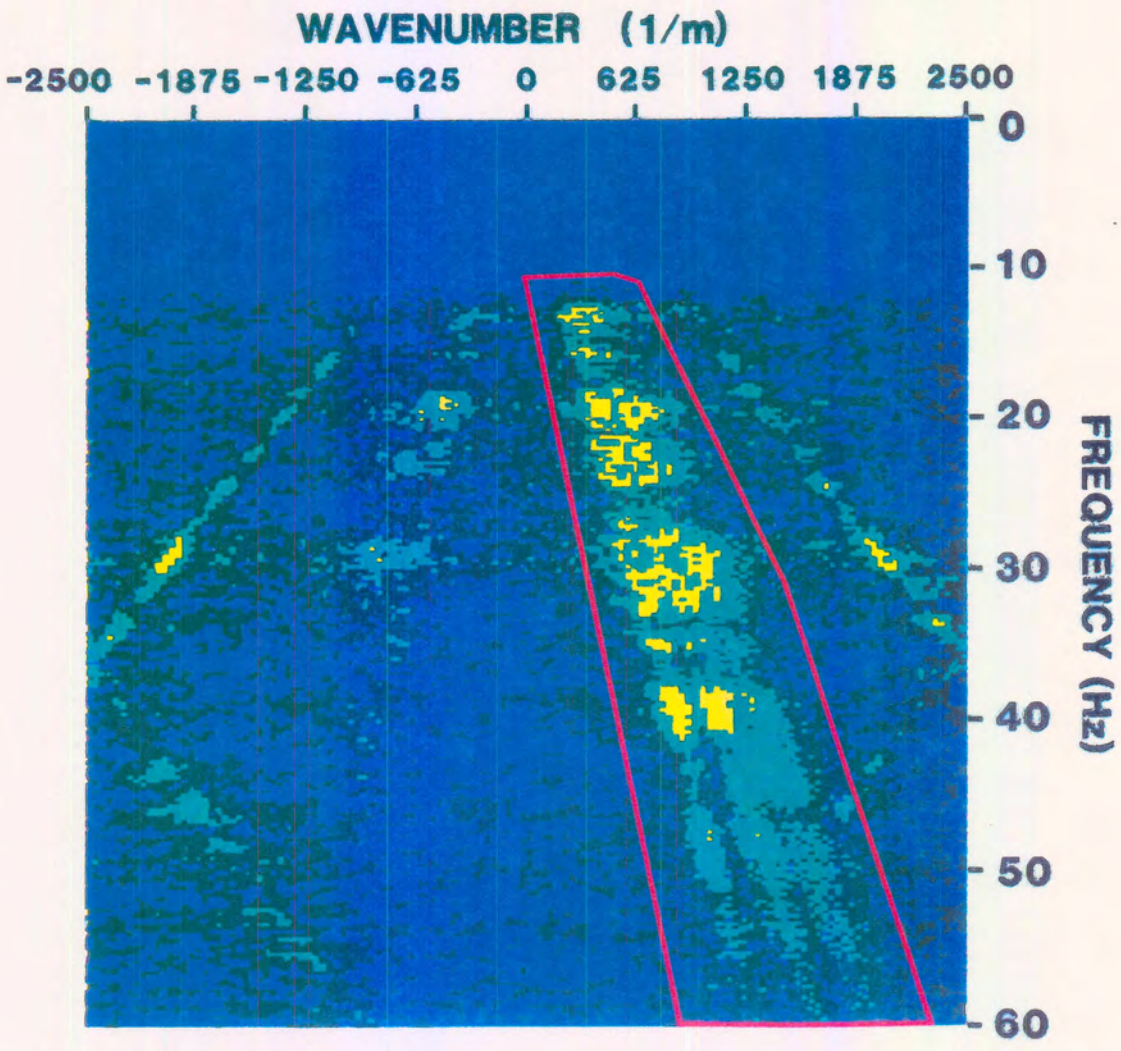

Figure 2.19 F-K plot of the data shown in Figure 2.18. This is the next interactive processing display following the screen presentation of Figure 2.18. A surgical mute polygon is interactively designed and the F-K events within the polygon can either be attenuated or preserved.

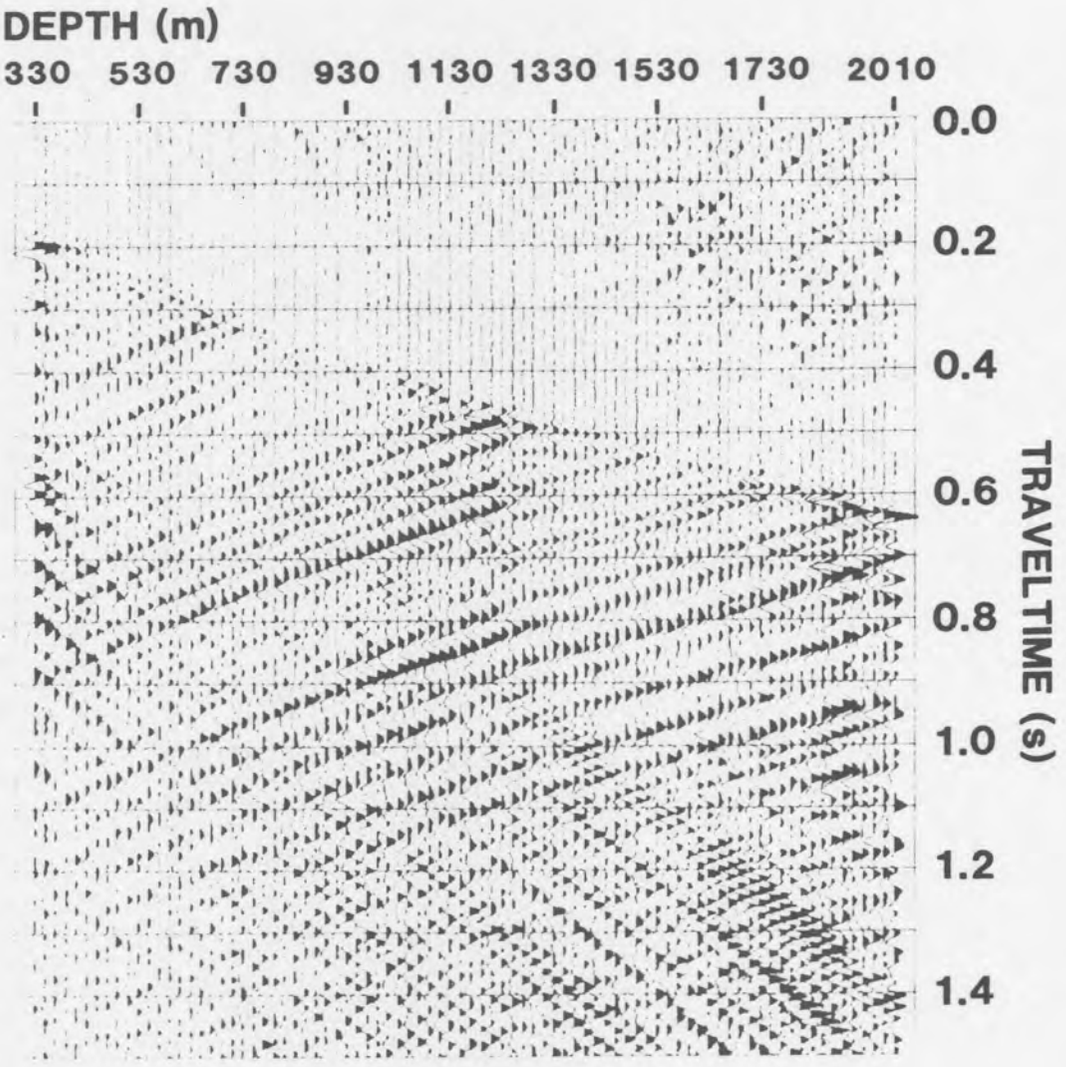

Figure 2.20 The "results" interactive processing display following the muting (reject filtering) of the F-K data inside the mute polygon shown in Figure 2.19. One can flip between the screen images using a mouse-controlled menu to evaluate the application of the polygon surgical mute. The upgoing P-wave and tubewave content of the **Z(FRT)** data seen in the initial screen display (Fig. 2.18) can now be interpreted.

Through the use of on-screen menu commands, the screen can alternatively display the **Z(FRT)** shown in Figure 2.18 or the filtered data, $\mathbf{Z_{up}(FRT)}$, shown in Figure 2.20. The interpretation of the upgoing events can be started using the $\mathbf{Z_{up}(FRT)}$ data. Moreover, by changing the vertices of the polygon F-K mute within the F-K plot bit-plane display, the effect of the mute design on the interpretation of the upgoing events can be determined. This interactive processing begins to get the processor/interpreter familiar with the wavefield content of the input **Z(FRT)** data.

2.2.4.5.2 The effect of changes in the F-K mute zones

In this section, the effect of the mute design on a particular segment of the VSP data is examined through the use of F-K interactive processing. The processing decisions made during this interactive F-K processing are shown in Flowchart 5. The example described below encompasses the series of plots in Figures 2.21 to 2.25. The segment of the F-K domain of concern is the aliased portion of the downgoing tubewave in the Fort St. John Graben near offset $\mathbf{Z_{up}(FRT)}$ VSP data (Hinds et al., 1991a; Hinds et al., 1993a and 1994b; Hinds et al., 1994c) which crosses the upgoing P-wave events within the F-K domain (as can be seen in Fig. 2.9).

The input data to the interactive processing are the $\mathbf{Z_{up}(FRT)}$ data resulting from the median filter wavefield separation method (Fig. 2.21). The downgoing tubewave is still evident within the data. The F-K representation of this data is shown in Figure 2.22. The up- and downgoing tubewaves are within the first mute zone polygons outlined in red. The aliased

FLOWCHART - Interactive F-K processing (for F-K mute zone design)

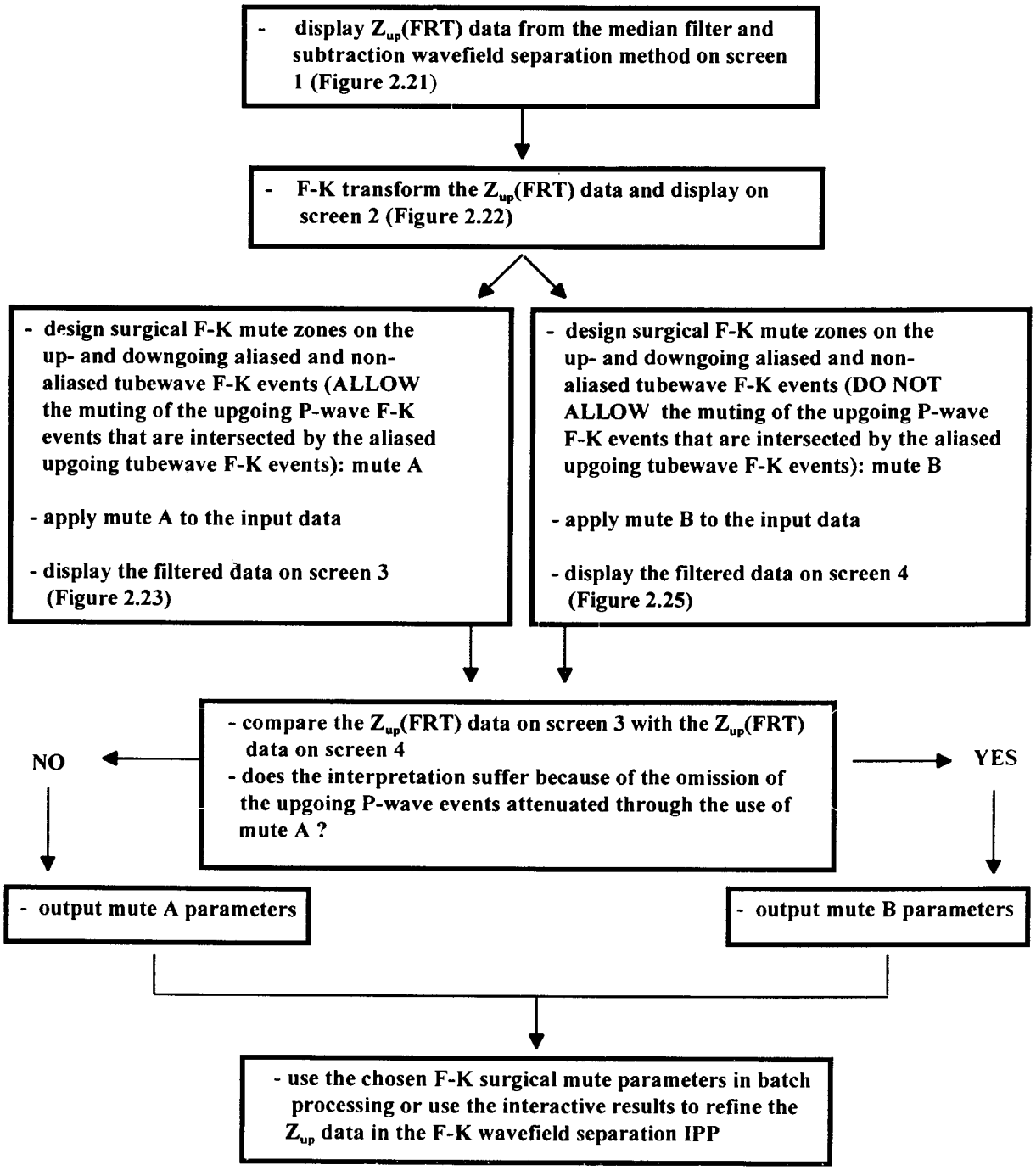

Flowchart 5. An example of the interpretive processing flowchart of the interactive F-K processing used for the attenuation of tubewave events on Z_{up}(FRT) data (Hinds et al., 1994c).

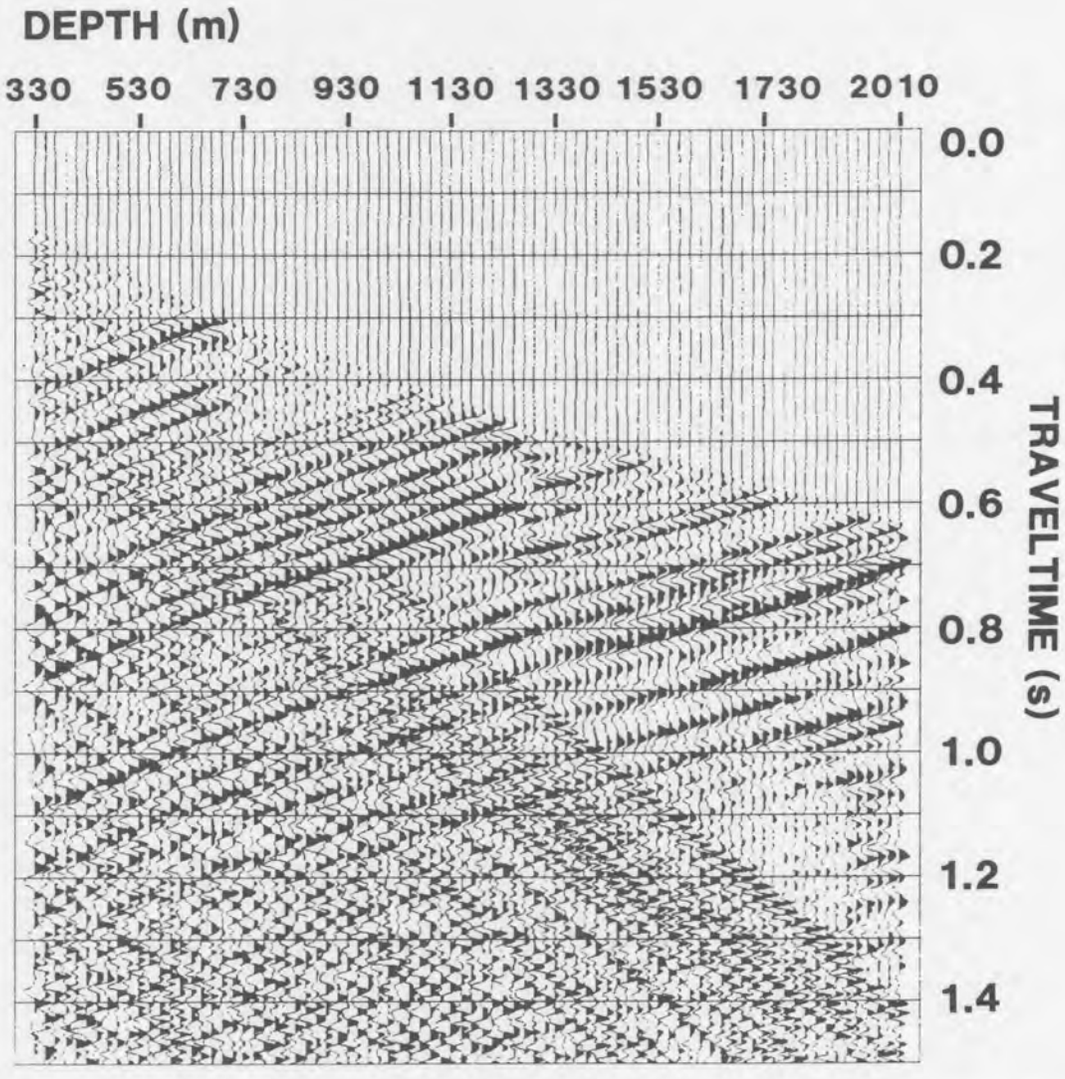

Figure 2.21 The Fort St. John Graben Z_{up}(FRT) data (Hinds et al., 1993a) resulting from median filter-based wavefield separation (plus subtraction). The downgoing tubewave aliased back into the data as an upgoing event. A question that the single operation interactive processing can answer is "how does one design the surgical F-K mute for the attenuation of the tubewave events and what effects, if any, does the design have on the upgoing P-wave events ?".

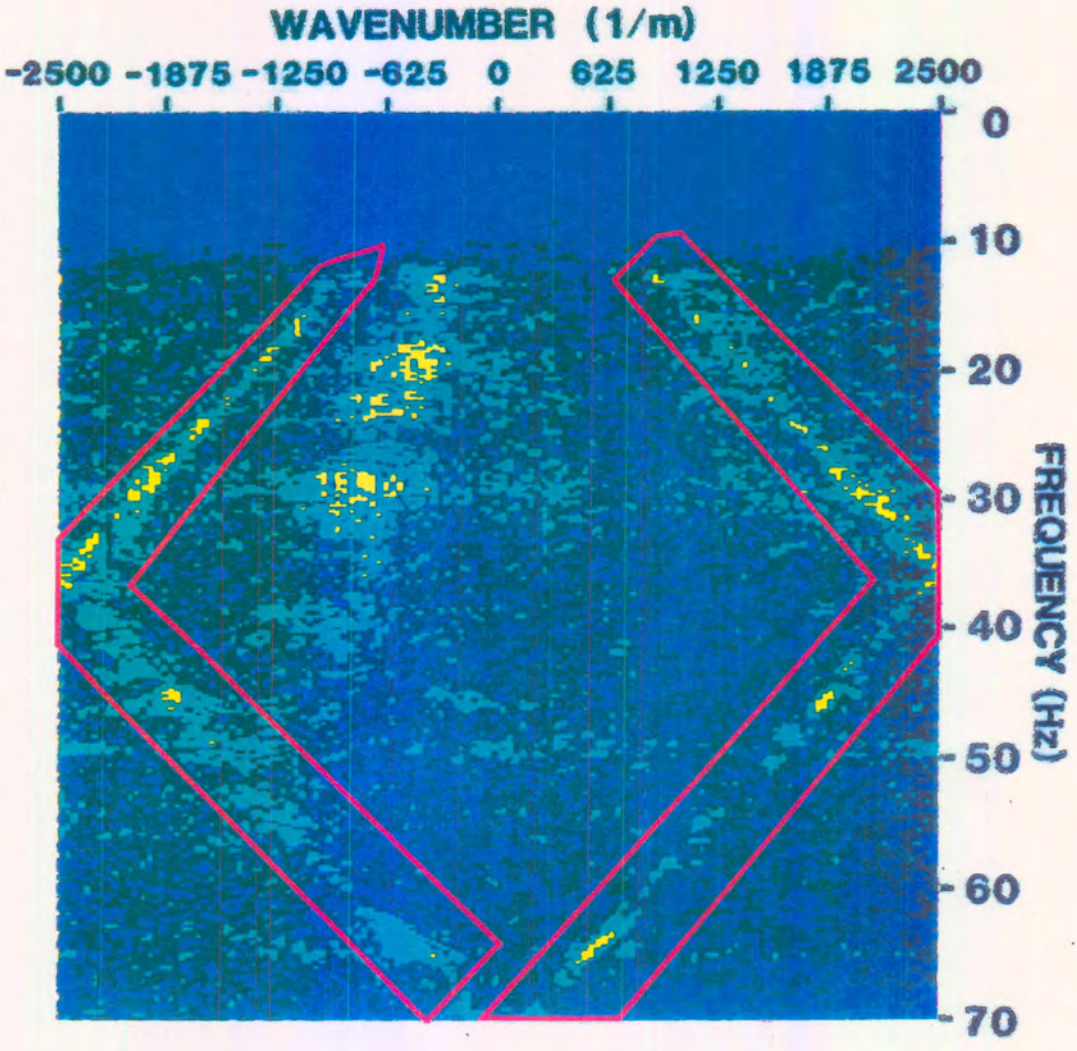

Figure 2.22 F-K plot of the data shown in Figure 2.19 illustrating the surgical mute reject polygons enveloping both the up- and downgoing F-K events (aliased and non-aliased portions included). The polygon in the negative K quadrant intersects the upgoing P-wave F-K events.

part of the downgoing tubewave events in the F-K domain crosses the upgoing P-wave events at approximately -1250 (10^{-5} m^{-1}) on the wavenumber axis and 55 Hz on the frequency axis.

How can the surgical mute F-K polygon be best designed to attenuate this tubewave? The designed F-K surgical mute polygons shown in Figure 2.22 also intersect some of the upgoing P-wave F-K events. Muting the F-K data within these reject zones would eliminate any upgoing P-wave events within the same zones. Would the application of the F-K polygon mutes adversely affect the interpretation of the upgoing P-waves in the depth-time domain? The application of the F-K reject mode of the polygons results in the $\mathbf{Z_{up}(FRT)}$ data shown in Figure 2.23. The downgoing and aliased tubewave events have been attenuated.

By returning to the F-K plot of the original data (Fig. 2.22) and redefining the F-K mute zone to not intersect the upgoing P-wave data, the effect on the interpretation on the upgoing P-wave data by the previous F-K filtering (Figs. 2.22 and 2.23) can be ascertained. The surgical mute polygons are updated to be the same as the design shown in Figure 2.22 except that the portion of the tubewave F-K event intersecting the upgoing F-K P-wave events are not attenuated (Fig. 2.24). This new set of surgical mutes yields the results shown in Figure 2.25. The results in Figures 2.23 and 2.25 can be compared to evaluate the effect of muting the upgoing event F-K data that lie in the 50-60 Hz range of the F-K domain during the effort to attenuate all of the tubewave events. The upgoing events in Figures 2.23 and 2.25 are similar and the interpretation of the upgoing events will not be degraded by using the F-K mute shown in Figure 2.22. The F-K procedures shown using Figures 2.18 through to 2.25 is another type of interpretive processing that the "interpreter/processor" can use.

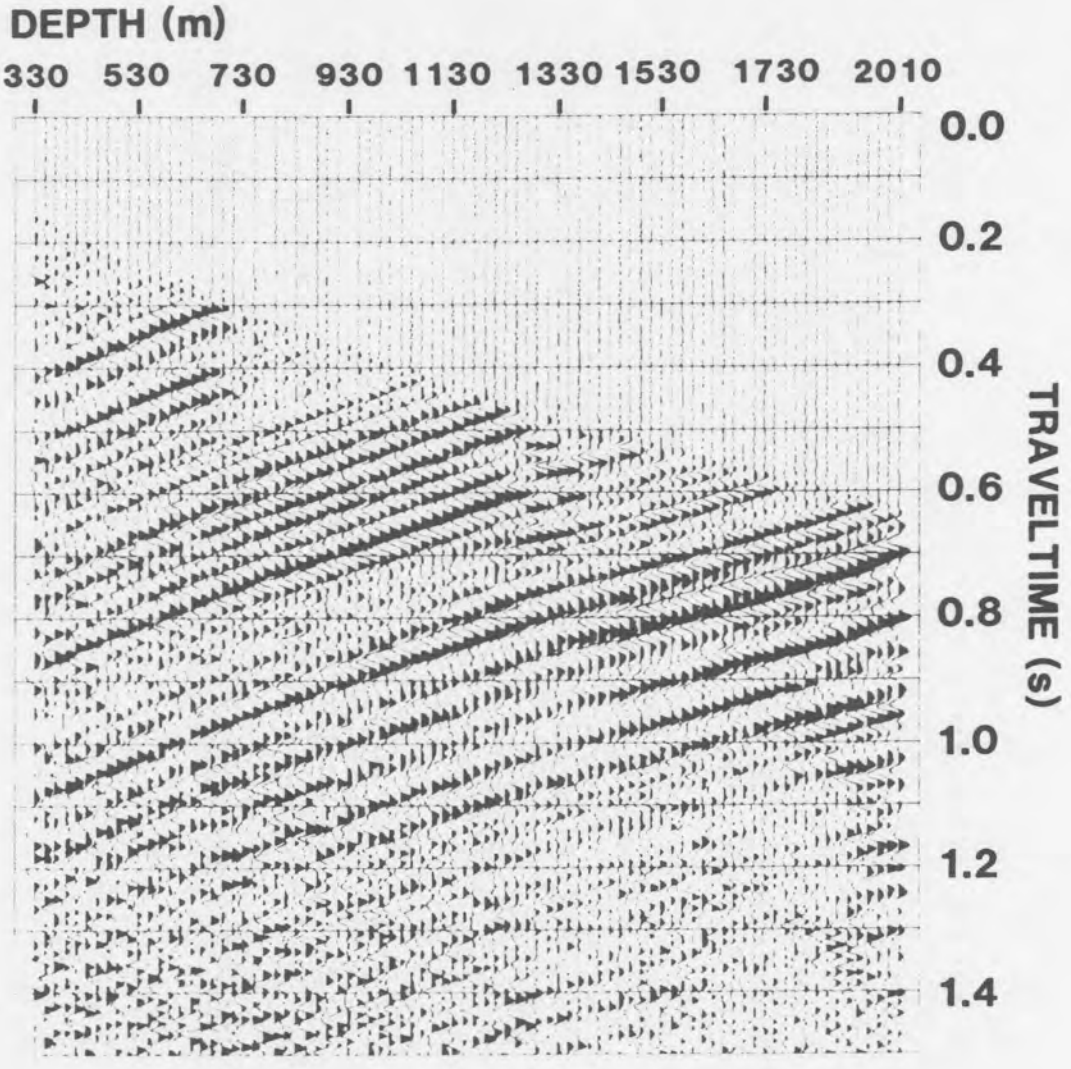

Figure 2.23 The filtered output of the data in Figure 2.21 following the application of the F-K polygon surgical mutes shown in Figure 2.22. The aliased and non-aliased portions of the tubewave events have been attenuated. The next question is "what effect would the application of F-K mute polygons which do not intersect the upgoing F-K events have on the filtered output?".

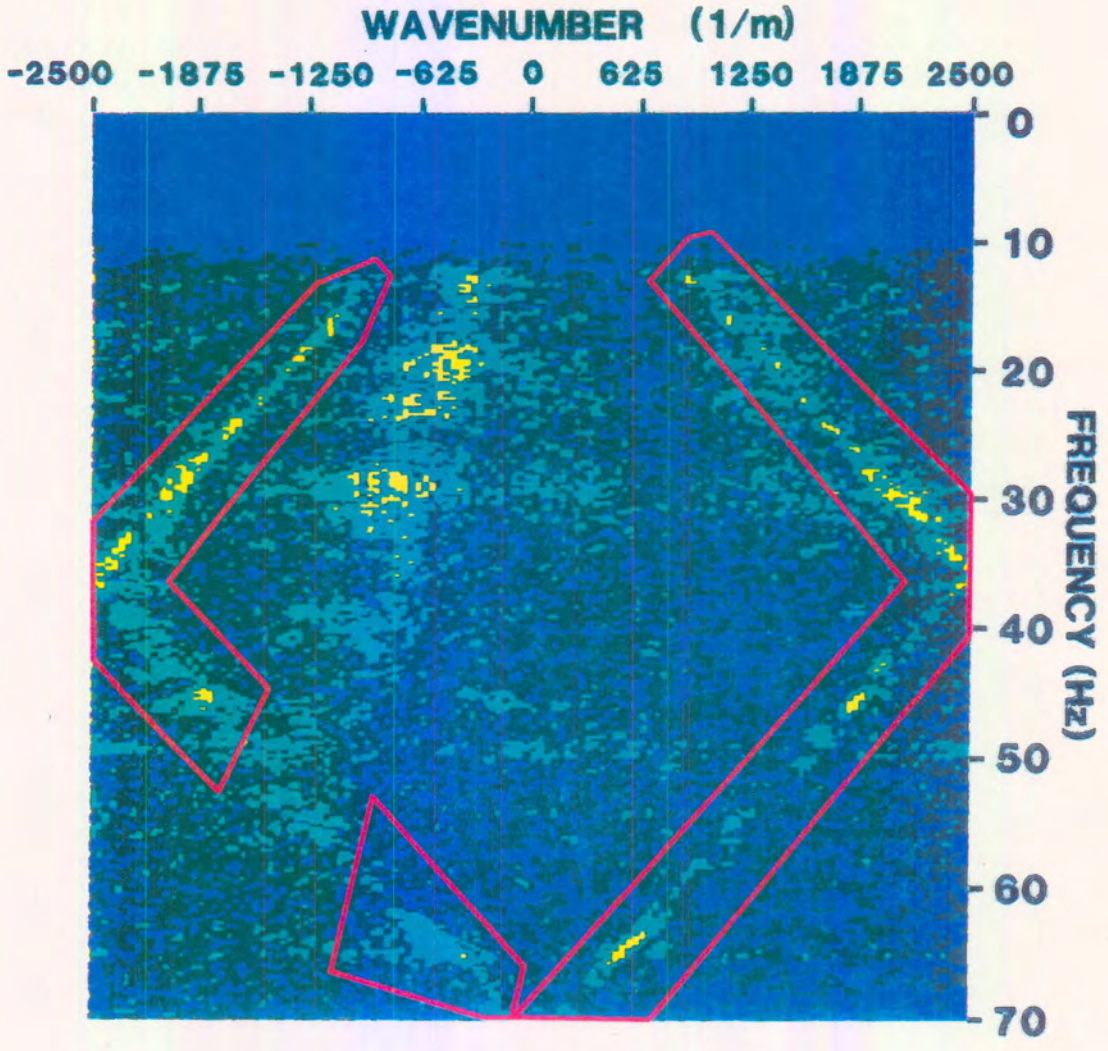

Figure 2.24 F-K plot of the data shown in Figure 2.21 illustrating the surgical mute reject polygons enveloping both the up- and downgoing tubewave F-K events (aliased and non-aliased portions included), however, excluding the muting of any upgoing P-wave F-K events.

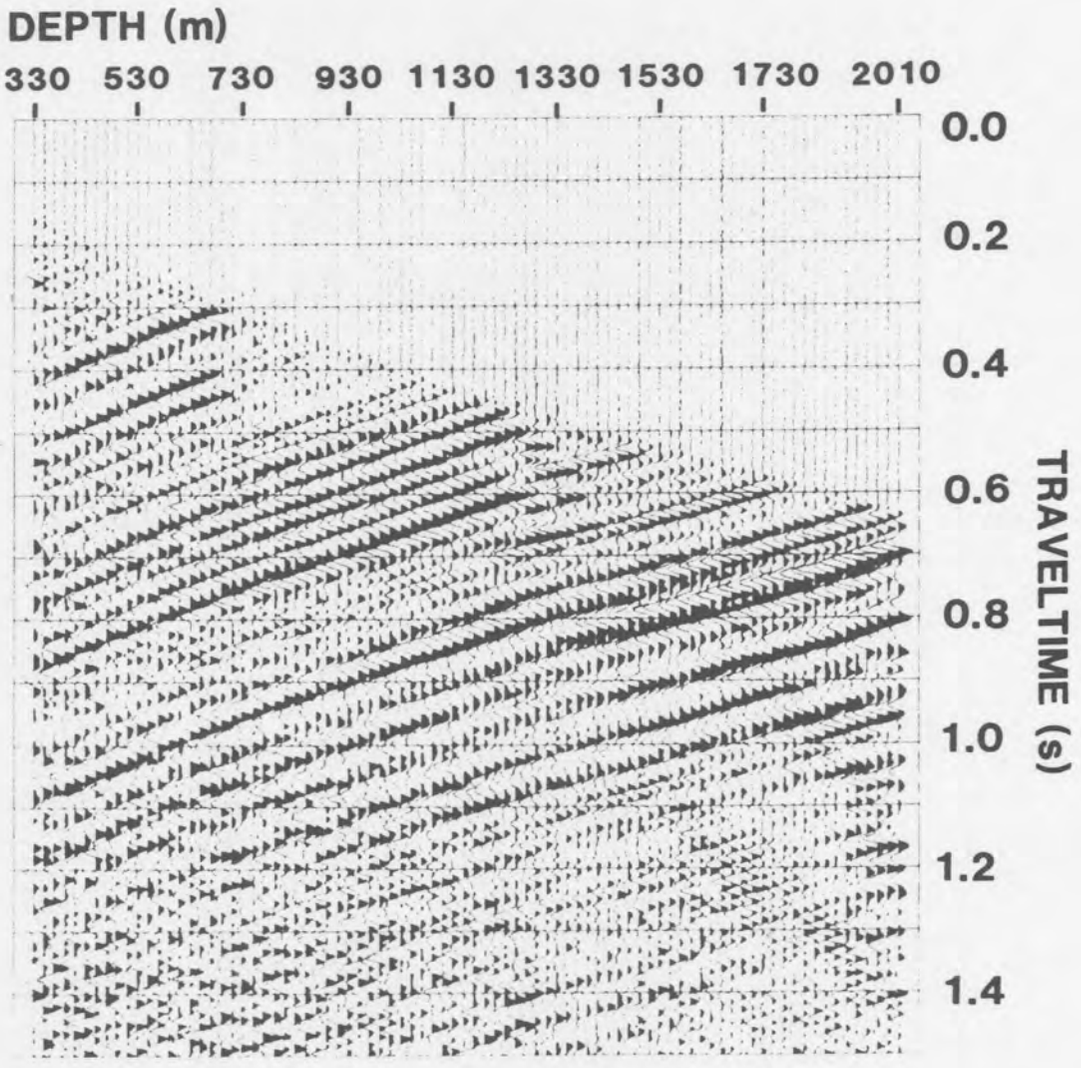

Figure 2.25 The filtered output of the data in Figure 2.21 after the application of the polygon surgical mutes shown in the F-K plot of Figure 2.24. A minor amount of the aliased downgoing tubewave event has been retained in the filtered output.

2.2.5 τ-P filtering

In this section, the use of the τ-P or Radon transform (Robinson, 1983; Deans, 1983; Durrani and Bisset, 1984; Turner, 1990, Hu and McMechan, 1987, Moon et al., 1986) within wavefield separation processing will be discussed.

Four routes will be examined in which the τ-P transform is used in wavefield separation. The routes are summarized in Flowchart 6 and consist of (Hinds et al., 1994c)

(1) Route A: τ-P transform the **Z(FRT)** data with upgoing event slownesses (P is the inverse of velocity), inverse τ-P transform to output $\mathbf{Z_{up}(FRT)}$ data;

(2) Route B: τ-P transform the **Z(FRT)** data with downgoing event slownesses, inverse τ-P transform to output $\mathbf{Z_{down}(FRT)}$ data, subtract the $\mathbf{Z_{down}(FRT)}$ from the **Z(FRT)** data to output the $\mathbf{Z_{up}(FRT)}$ data;

(3) Route C: τ-P transform the **Z(FRT)** data with upgoing event slownesses, inverse τ-P transform using a depth interval parameter of half the original depth spacing to spatially interpolate the $\mathbf{Z_{up}(FRT)}$ data; and

(4) Route D: τ-P transform the **Z(FRT)** over both up- and downgoing event slownesses, inverse τ-P transform using half the original depth increment, wavefield separate the

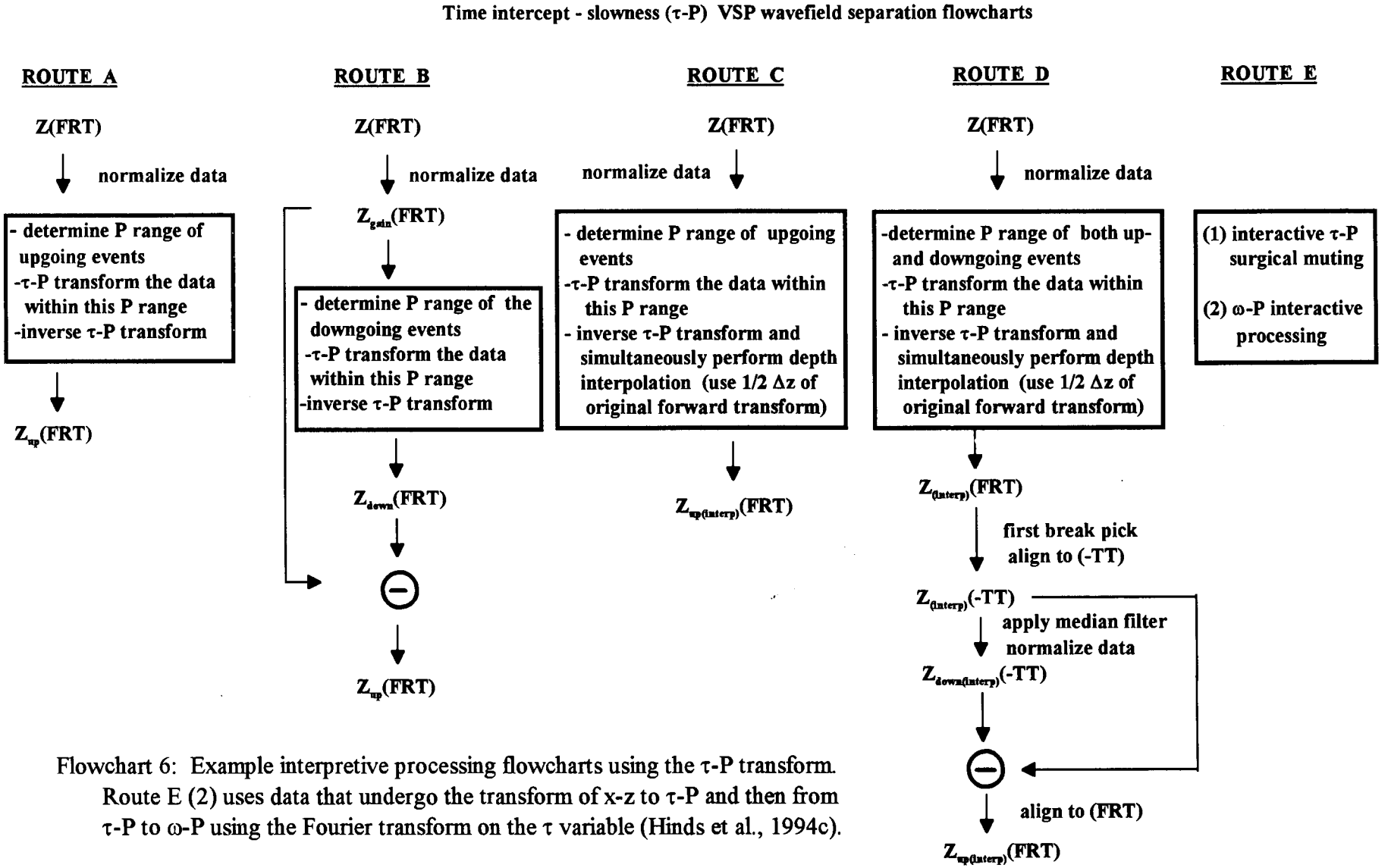

Flowchart 6: Example interpretive processing flowcharts using the τ-P transform. Route E (2) uses data that undergo the transform of x-z to τ-P and then from τ-P to ω-P using the Fourier transform on the τ variable (Hinds et al., 1994c).

$\mathbf{Z_{(interp)}(FRT)}$ data using median filter based wavefield separation to output $\mathbf{Z_{up(interp)}(FRT)}$ data.

The τ-P transform based wavefield separation routes will be applied to both the multiple contaminated and tubewave contaminated **Z(FRT)** data used in the previous sections. The multiple contaminated data will be used to illustrate the route A processing since Rieber mixing may occur using this processing flow. The preservation of the lateral extent of the multiple events in the $\mathbf{Z_{up}(FRT)}$ data will be examined. The three other routes of τ-P processing will use the tubewave contaminated **Z(FRT)** data. The tubewave events in these data are spatially aliased and the effect of the processing schemes on the spatially aliased tubewave will be examined.

2.2.5.1 Review of τ-P filtering

A conceptual explanation of the τ-P transform is illustrated in Figure 2.26 (Hardage, 1992; Fig. 136). The τ variable refers to the time intercept of the lines of integration in the time-depth (or time-offset for CDP gathers) domain. The P variable refers to the slowness (inverse of velocity) values associated with the lines of integration. In Figure 2.26A, two lines with different slopes are shown intersecting the example time-depth data point. Integration of the time-depth data along each line, $t=p_1x+\tau_1$ and $t=p_2x+\tau_2$, would yield two values in the τ-P domain as seen in the lower half of Figure 2.26A. The different slopes of the lines refer to different P or slowness values.

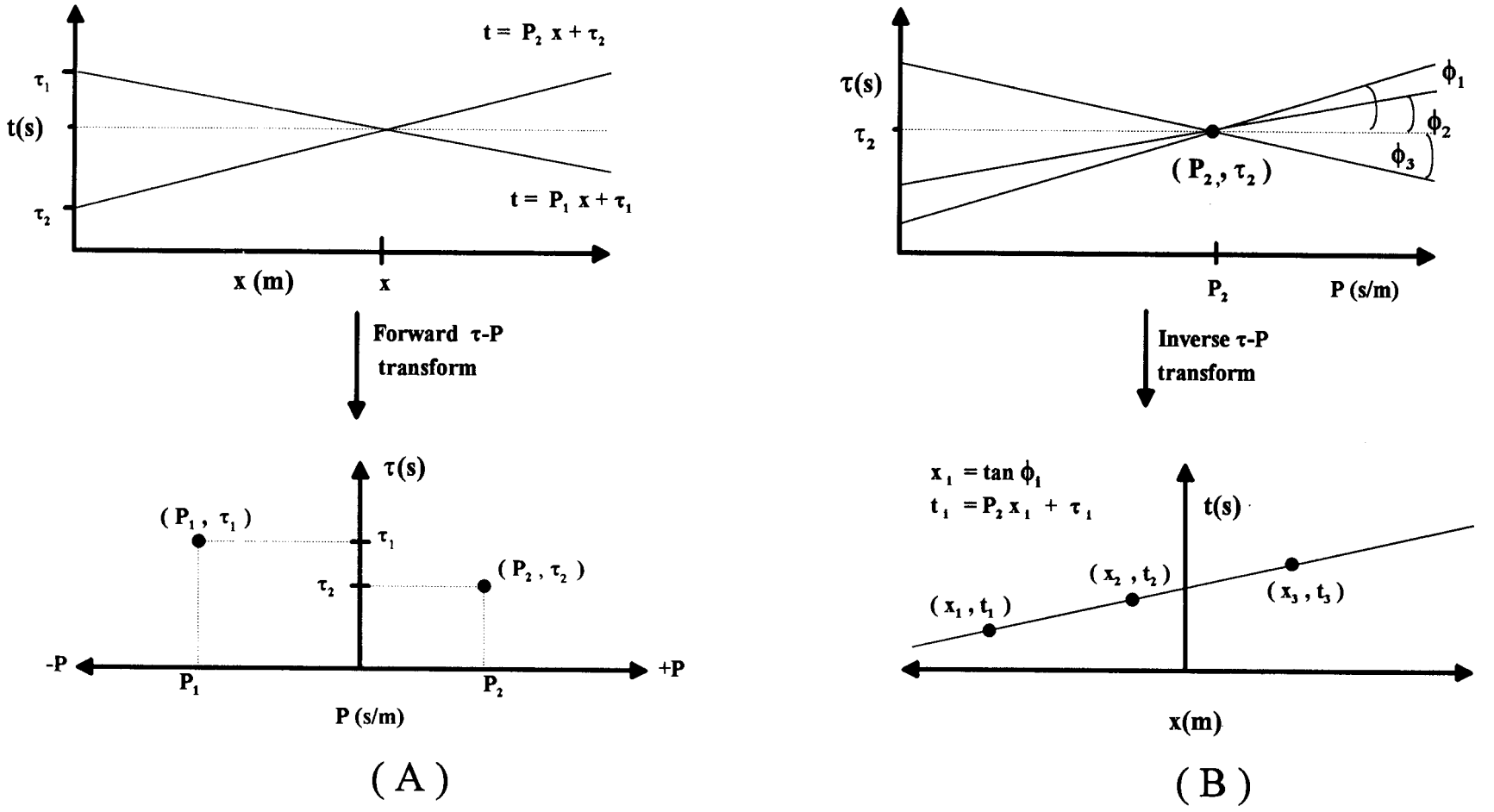

Figure 2.26 The concept of the forward and reverse τ–P transform. The forward transform (Part A) maps a line into a point and the reverse transform (Part B) maps a line in τ–P domain back to a point in the time-offset (depth) domain (from Hardage, 1985).

To perform the inverse τ-P transform (Kappus et al., 1990), the same procedure is done within the τ-P domain. As shown in the top part of Figure 2.26B, three lines of integration through a single point in the τ-P domain results in the values for three points along a straight line in the time-depth domain.

Whereas the F-K transform mapped a line in the time-depth domain into a line intersecting the origin of the F-K domain, the τ-P transform maps a line in the time-depth domain into a point in the τ-P domain. The two transforms are linked through the P or inverse velocity parameter. The Rieber mixing present in the F-K filtering exists in τ-P filtering since the τ-P filtering is based on velocity.

For surface seismic data, the hyperbolic-shaped reflection events on a common depth point (CDP) gather map into ellipses in the τ-P domain (Stoffa et al., 1981). The CDP gather can be transferred into the X^2-T^2 domain and τ-P transformed to enable multiple attenuation in the surface seismic data. Following interpolation in the X^2-T^2 domain, the hyperbolic reflection events of the X-T data become linear events in the X^2-T^2 domain and subsequently "points" in the τ-P domain. The points are smeared due to truncation effects resulting from the transform of finite events (the offset range is not infinite) and the representation of the events with near-zero spatial frequencies (near-offset events at the apex of the reflection hyperbolas). Muting in the τ-P domain results in multiple attenuation (Hinds and Durrheim, 1993 and 1994).

Instead of the hyperbolic events seen in the CDP gather of surface seismic data, the depth-time events of the **Z(FRT)** data are linear. The purpose of the X^2-T^2 processing of the CDP

gathers in Hinds and Durrheim (1993, 1994) was to transform the hyperbolic events into linear events. Similarly to that work, the VSP linear events will be transformed into "points" following the τ-P transformation. The up- and the downgoing VSP events will map into different quadrants of the τ-P domain because the events have oppositely signed apparent velocities. Wavefield separation can then be realized through the attenuation of the amplitude data in the τ-P domain containing the downgoing events (Hardage, 1992; Hu and McMechan, 1987).

2.2.5.2 Route A: τ-P transformation of only the upgoing events

Rieber mixing may become a factor in τ-P wavefield separation due to the equivalence of the slowness range and F-K narrow pie-slices. To illustrate this, the multiple contaminated **Z(FRT)** data from the Fort St. John Graben case study (Hinds et al., 1991a; Hinds et al., 1993a; Hinds et al., 1994c) will be used in the Route A processing. The effect of the τ-P filtering will be shown in the F-K domain to illustrate the equivalence of the two methods, τ-P and F-K.

The τ-P wavefield separation IPP for Route A is shown in Figure 2.27. The processing runstream for the Route A τ-P processing is shown in Flowchart 6A. The input data to the forward τ-P transform is limited to be the VSP data with velocities similar to the upgoing events.

The normalized and gained **Z(FRT)** data are shown in panels 1 and 2, respectively, of Figure 2.27. The $\mathbf{Z_{up}(FRT)}$ data shown in panel 3 was a result of the inverse τ-P transformation

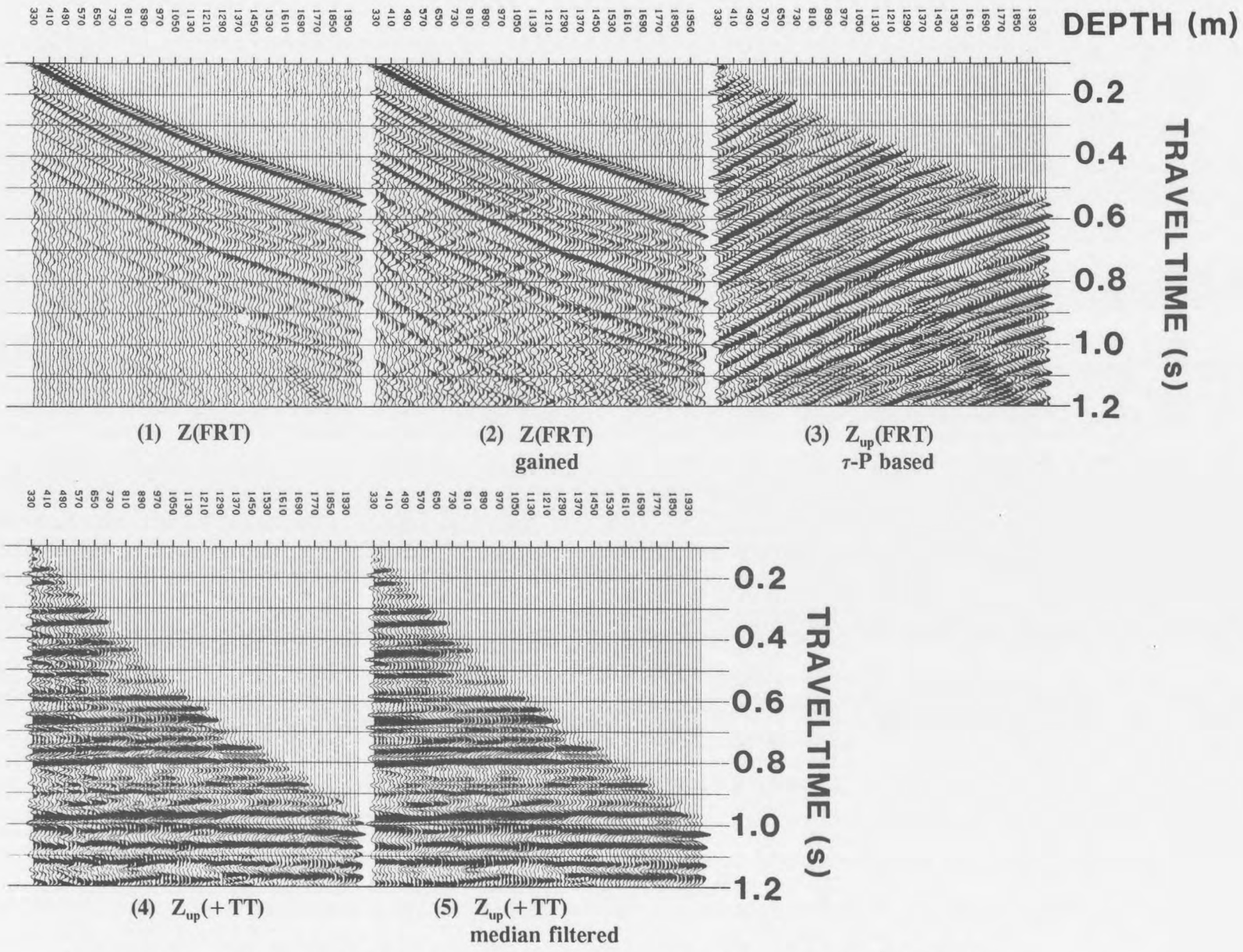

Figure 2.27 τ-**P** (route A) based wavefield separation IPP of the Fort St. John Graben (Hinds et al., 1993a) multiple contaminated data.

of the isolated upgoing events from the forward τ-P transform of the **Z(FRT)** data. The forward τ-P transform of the **Z(FRT)** data did not include the slowness values of the downgoing VSP events.

The slowness range in the forward τ-P transformation of the **Z(FRT)** data were from near-zero (about -24,000 m/s) to -0.0000035 s/m (-2400 m/s). The F-K plot of the $\mathbf{Z_{up}(FRT)}$ data from panel 3 of Figure 2.27 is shown in Figure 2.28. The two slowness values define linear cut-offs in F-K space filtering.

The $\mathbf{Z_{up}(FRT)}$ in panel 3 can be compared to the F-K filtered $\mathbf{Z_{up}(FRT)}$ data in panel 5 of Figure 2.7. The upgoing event data in panel 5 of Figure 2.7 was isolated from the **Z(FRT)** data using the narrow "accept" zone seen in Figure 2.12. The equivalent "accept" zone used in the τ-P processing is larger than the zone used for the F-K wavefield separation. As a result, the $\mathbf{Z_{up}(FRT)}$ data shown in panels 3,4, and 5 of Figure 2.27 exhibit a lesser degree of Rieber mixing than similar data seen in Figure 2.7.

The two IPP panels (Figs. 2.7 and 2.27) are opposite in polarity. In panels 4 and 5 of Figure 2.27, the highlighted (in orange) isolated trough at 0.755 s appearing on the depth traces between 1270 m and the first break curve is the primary event that is embedded within the series of multiples. The same primary upgoing event appears as a peak (highlighted in blue) in panel 5 of Figure 2.7; however, the trace to trace amplitude contrasts in Figure 2.7 have been smeared by Rieber mixing.

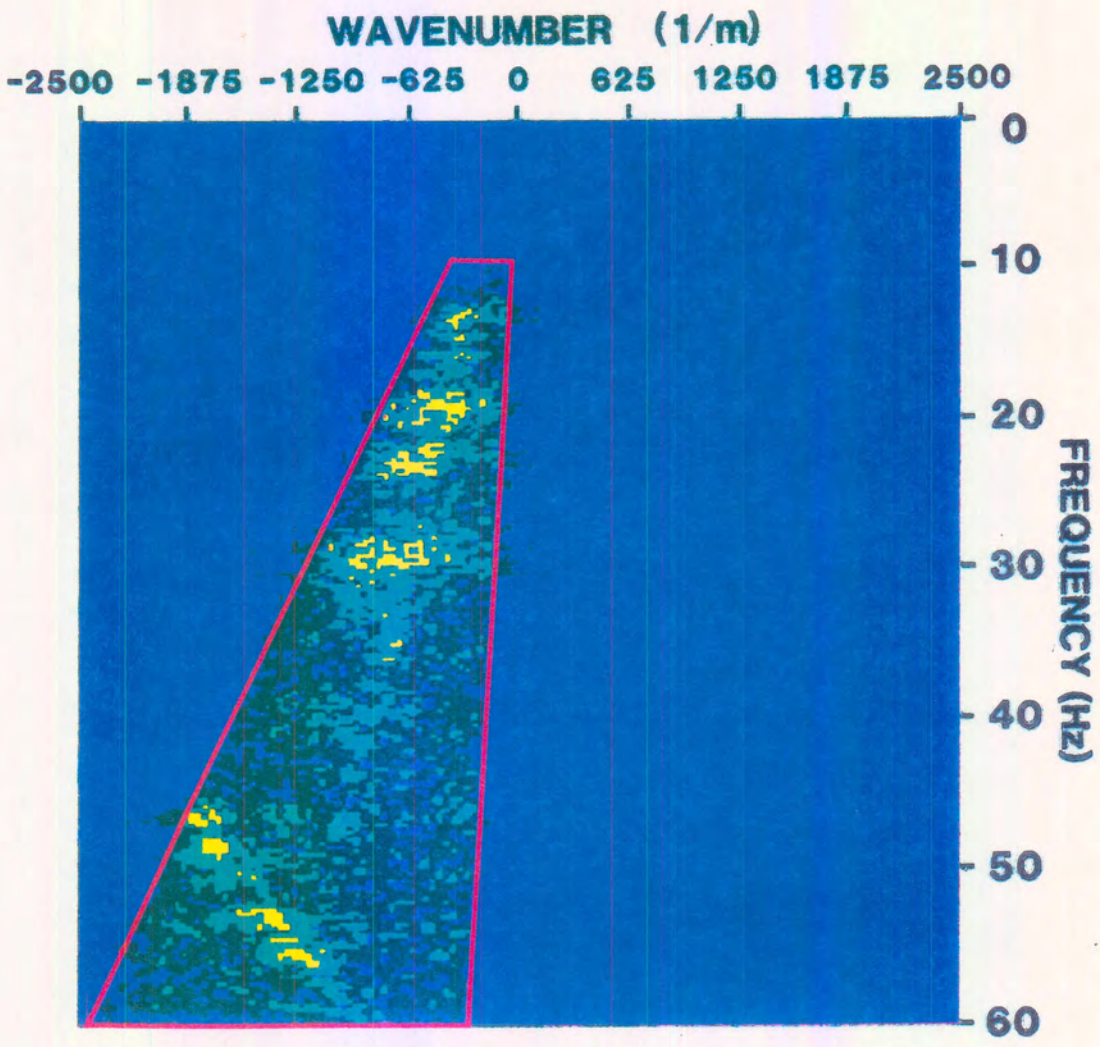

Figure 2.28 The equivalent F-K surgical mute pass zone to the τ-P filter used to create the resultant data in panel 3 of Figure 2.27. This can be compared to the F-K narrow pass zone shown in Figure 2.12.

2.2.5.3 Route B: Subtraction of Z_{down}(FRT) from the Z(FRT) data

In this section, the downgoing events are isolated from the **Z(FRT)** data using the τ-P transform. The $\mathbf{Z_{down}(FRT)}$ data are then subtracted from the **Z(FRT)** data to yield the $\mathbf{Z_{up}(FRT)}$ results.

The wavefield separation IPP for this approach using the tubewave contaminated Z(FRT) data example is shown in Figure 2.29. The $\mathbf{Z_{down}(FRT)}$ data, shown in panel 3, are isolated using τ-P filtering and following scaling, the data are subtracted from the **Z(FRT)** data (shown in panel 2 of Fig. 2.29) to output the separated upgoing event data, $\mathbf{Z_{up}(FRT)}$, shown in panel 4. This is similar to the results obtained using the median filter based wavefield separation method shown in Figure 2.2. The aliased downgoing tubewave (appearing as upgoing events and highlighted in panel 4) have not been attenuated. This processing route avoids possible Rieber mixing because the action of the τ-P filter is now similar to the use of a narrow "reject" F-K filter to attenuate the upgoing events.

2.2.5.4 Route C: τ-P spatial interpolation during wavefield separation

In this section, the upgoing events are separated from the **Z(FRT)** data during the transformation to the τ-P domain by using selected slownesses. Trace depth interpolation to a finer depth sampling is performed during the inverse transform. The effect that the spatial interpolation has on the inverse τ-P transformed aliased tubewave will be examined.

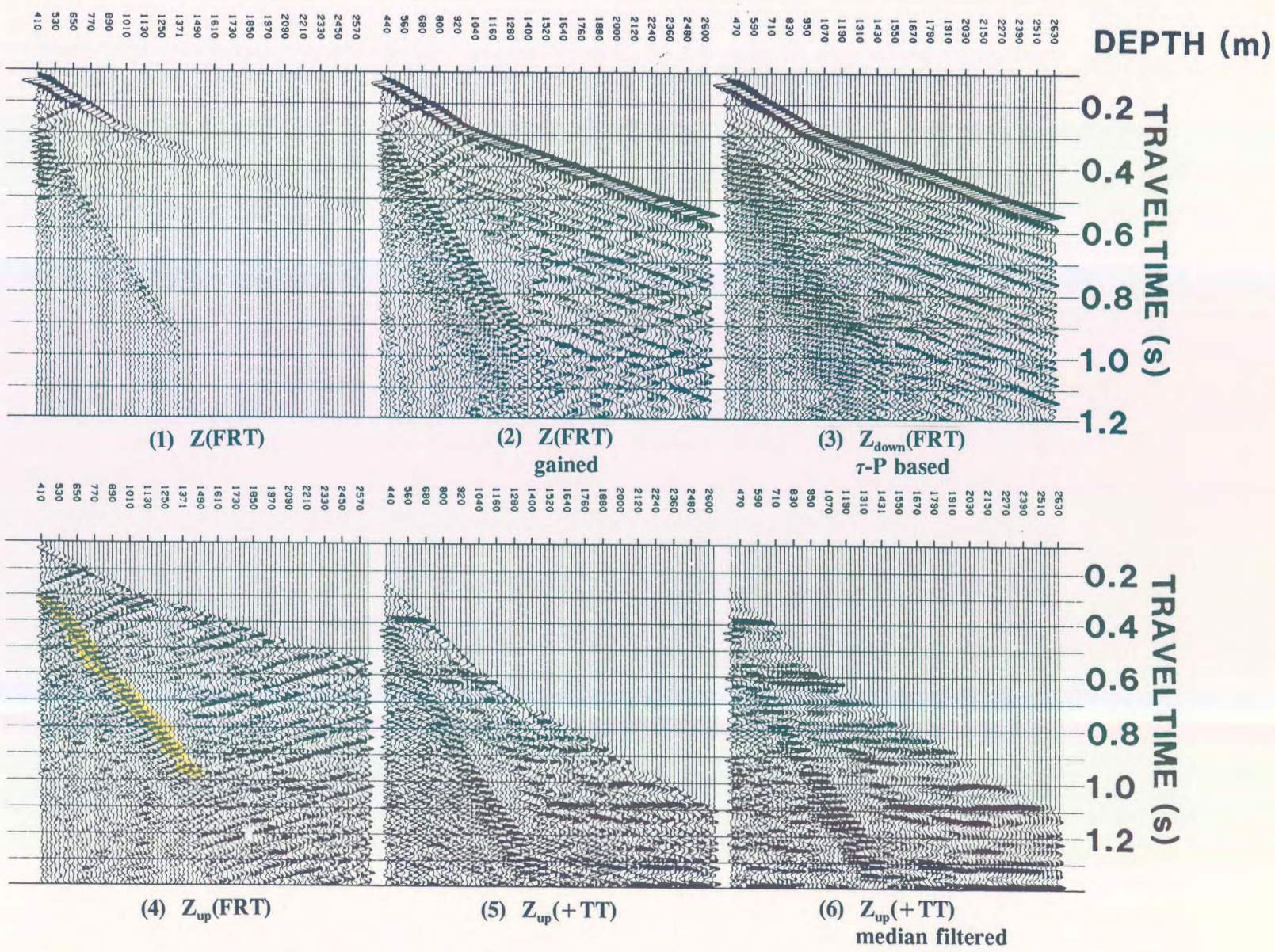

Figure 2.29 **τ-P** (route B) based wavefield separation IPP of the tubewave contaminated data using **τ-P** downgoing event separation and then subtraction of the $\mathbf{Z_{down}(FRT)}$ from the **Z(FRT)** to output the $\mathbf{Z_{up}(FRT)}$ data.

Figure 2.30 shows the F-K plot of the tubewave contaminated **Z(FRT)**. The downgoing P-wave events are shown in the negative k_z quadrant because the **Z(FRT)** data came from an early stage of preprocessing. The depth interval for the traces is 30 m and the downgoing tubewave aliases back into the upgoing events. The centre of the intersection is about at 37 Hz and 833 ($*10^{-5}$) m^{-1} on the k_z axis. The intersection of the aliased downgoing tubewave with the upgoing P-wave F-K events is highlighted in Figure 2.30 at the cursor location.

The **Z(FRT)** data are forward τ-P transformed using the slowness range of the upgoing events only. The aliased downgoing tubewave F-K events will also be "retained" during the forward transformation since these events appear in the same slowness range as the upgoing P-wave events due to aliasing. During the inverse transform, the trace spacing sampling interval is redefined to be 15 m. The $\mathbf{Z_{up(interp)}(FRT)}$ data at the interpolated trace spacing of 15 m are displayed in panel 2 of Figure 2.31. The aliased downgoing tubewave events preserved during the inverse τ-P transformation are highlighted in panel 2.

The interpolation performed during the inverse τ-P transform has faithfully interpolated even the aliased tubewave (as is shown in the $\mathbf{Z_{up(interp)}(FRT)}$ F-K plot in Fig. 2.32). The upgoing F-K events are shown in the negative F-K quadrant of Figure 2.32. The intersection of the interpolated aliased tubewave with the interpolated upgoing F-K events is still at 37 Hz and at 833 ($*10^{-5}$) m^{-1}! This is the same location as the tubewave event intersection with the upgoing events in the F-K domain before interpolation. The major change in the F-K plot is that the K_z Nyquist values have doubled in size from 1666 to 3333 $*10^{-5}$ m^{-1}.

Do the $\mathbf{Z_{up}(FRT)}$ data look markedly different without the interpolation? To answer this, the

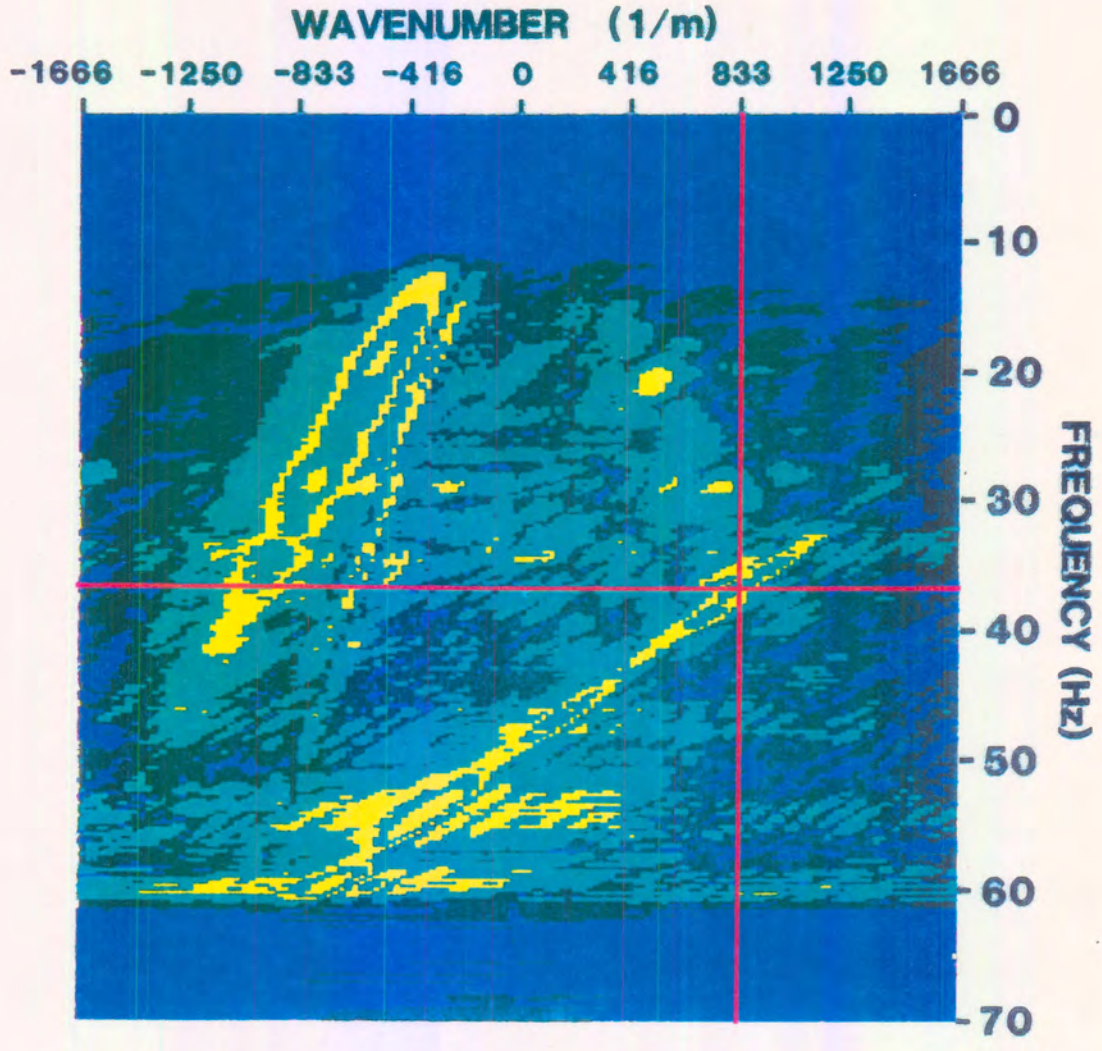

Figure 2.30 F-K plot of the tubewave contaminated data showing the aliased tubewave F-K event intersecting (at the crossing of the red lines) the upgoing P-wave F-K event at 0.00833 m^{-1} spatial frequency (K) and 37 hz.

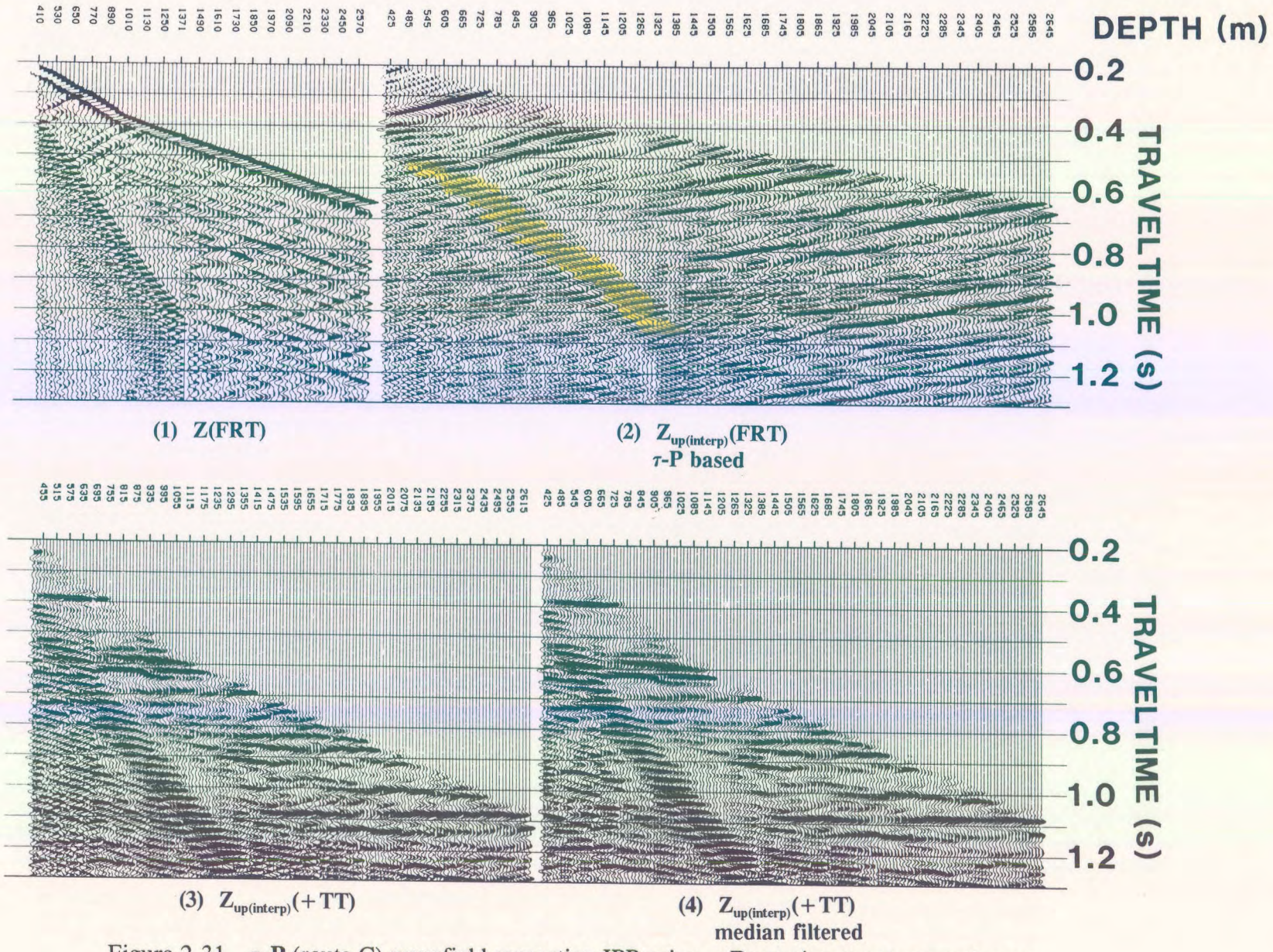

Figure 2.31 τ-**P** (route C) wavefield separation IPP using τ-**P** upgoing event separation on **Z(FRT)** with 30 m trace separation and inverse τ-**P** transformation using trace interpolation to create 15 m trace spacing.

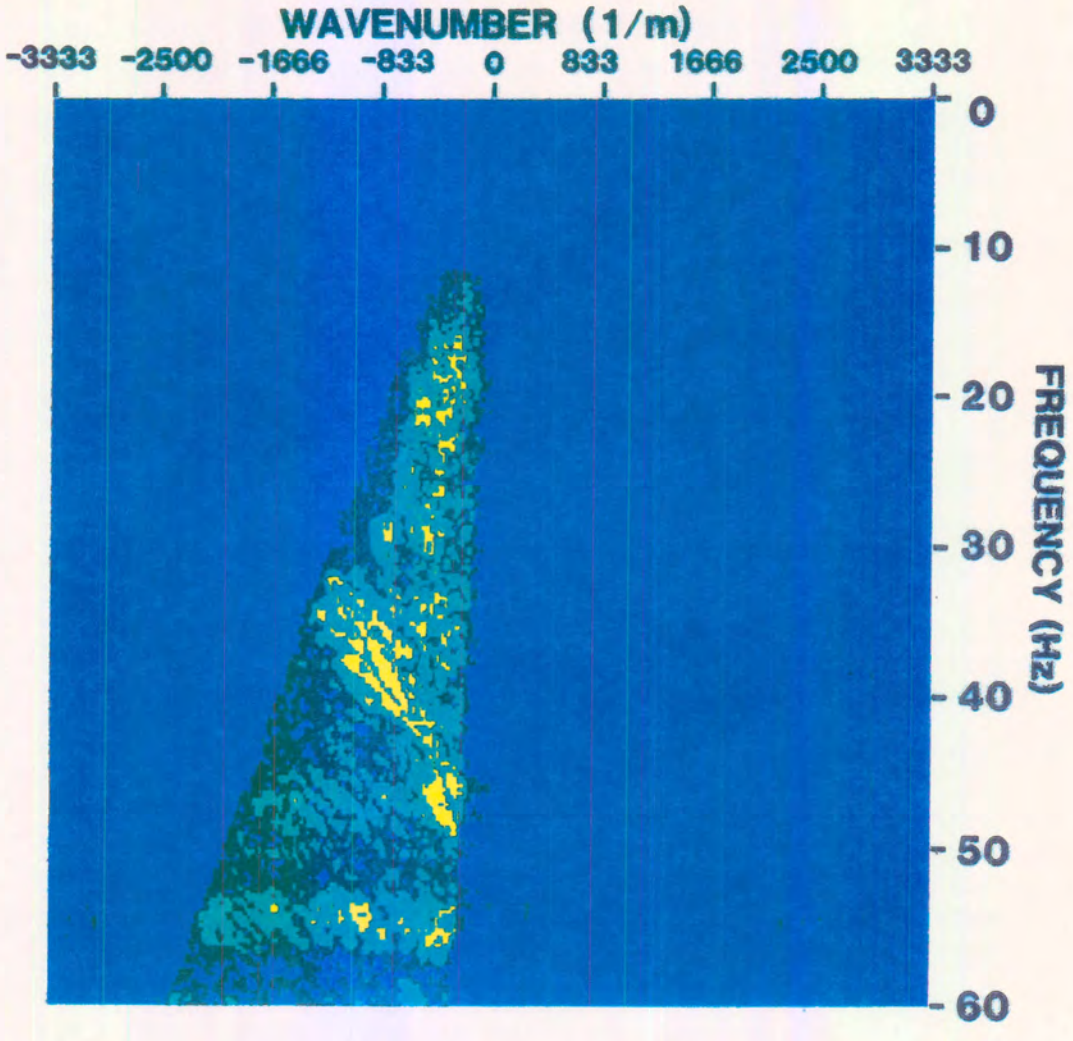

Figure 2.32 F-K plot of the interpolated tubewave contaminated $Z_{up(interp)}$(FRT) data where the aliased tubewave F-K event intersects the upgoing P-wave F-K event at 0.00833 m^{-1} spatial frequency (K) and 37 hz. The range of the wavenumber (K) axis has doubled in value (due to the 15 m trace spacing), however, the intersection of the aliased tubewave and upgoing P-wave F-K events remains the same as in Figure 2.30.

tube wave contaminated **Z(FRT)** was wavefield separated using the τ-P filtering but without trace interpolation. The resultant $\mathbf{Z_{up}(+TT)}$ data are shown in the IPP of Figure 2.33. By inspection, it is evident that the $\mathbf{Z_{up(interp)}(+TT)}$ interpolated data in panel 4 of Figure 2.31 is similar to the non-interpolated $\mathbf{Z_{up}(+TT)}$ data in panel 4 of Figure 2.33.

2.2.5.5 Route D: τ-P spatial interpolation of Z(FRT) before wavefield separation

In this section, both the up- and downgoing events of the **Z(FRT)** data are preserved during the forward τ-P transform. Spatial interpolation is performed during the inverse transform and wavefield separation is then performed using median filtering on the $\mathbf{Z_{(interp)}(FRT)}$ data. This procedure would be useful when processing a dataset which had irregular depth spacing and required interpolation. Although the tubewave contaminated **Z(FRT)** data do have regular spacing, the IPP is presented showing median filter wavefield separation using τ-P trace interpolated data.

The spatially interpolated data are shown in panel 1 of Figure 2.34. The results of using the $\mathbf{Z_{(interp)}(FRT)}$ data in a median filter based wavefield separation procedure method are shown in panels 2, 3, 4 and 5. In panel 5, the $\mathbf{Z_{up(interp)}(-TT)}$ data with 15 m depth spacing are shown. The $\mathbf{Z_{up(interp)}(+TT)}$ and $\mathbf{Z_{up(interp;med)}(+TT)}$ data are shown in panels 6 and 7, respectively.

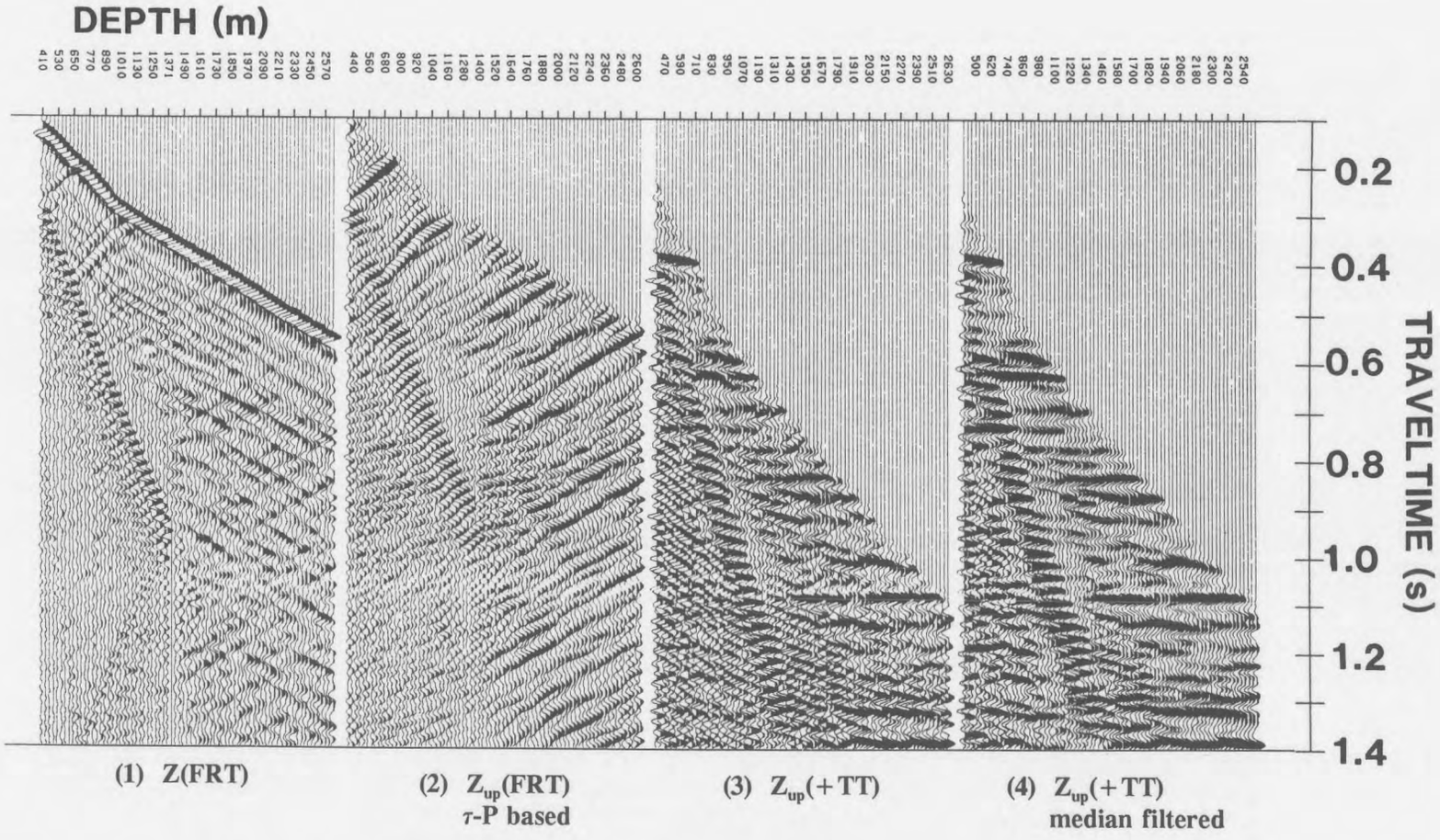

Figure 2.33 **τ-P** based wavefield separation IPP of the tubewave contaminated data using **τ-P** upgoing wave isolation (filtering out P values outside the range of the upgoing P-wave events).

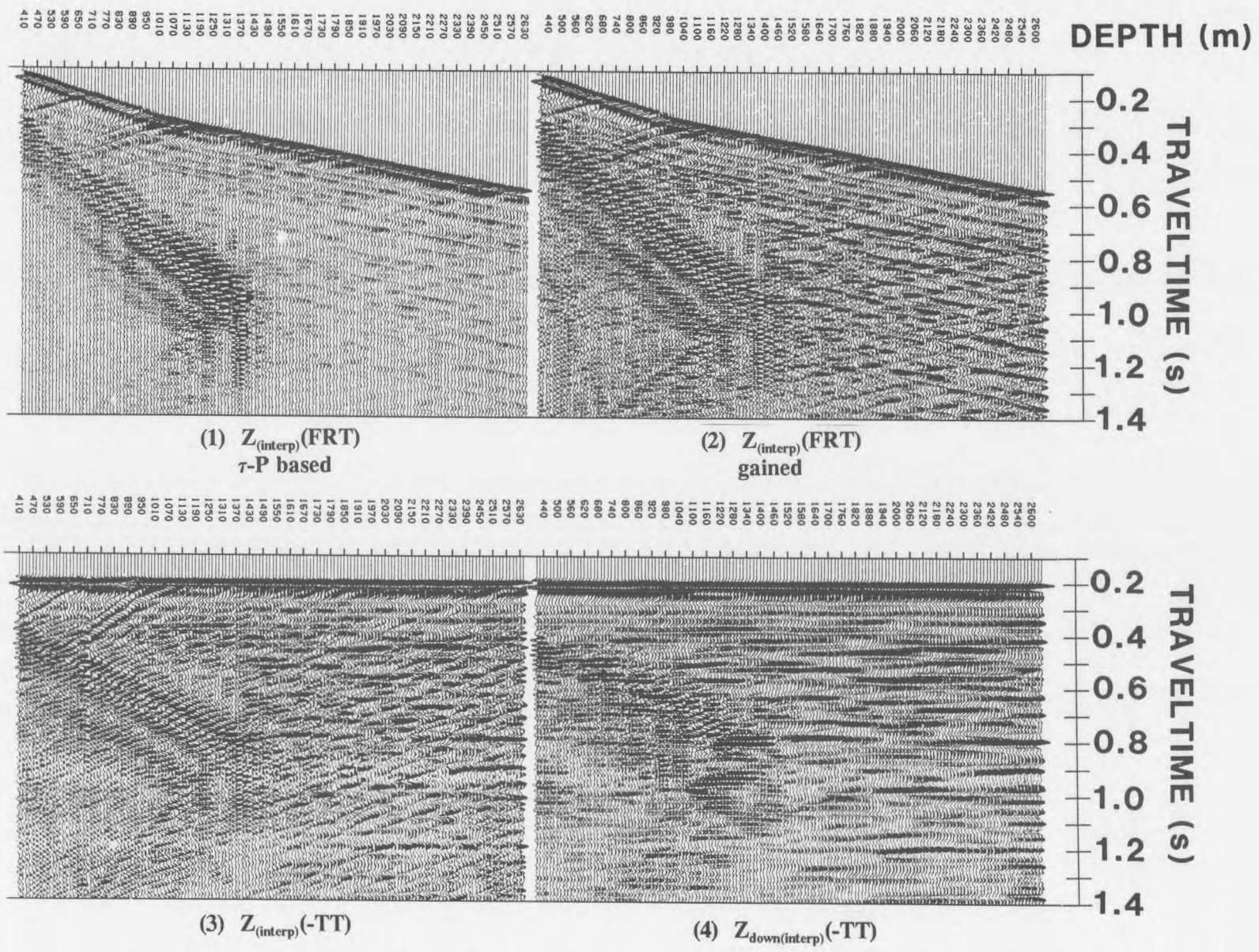

Figure 2.34A Panels 1 to 4 of the τ-**P** based wavefield separation IPP using the interpolated **Z(FRT)** tubewave contaminated data.

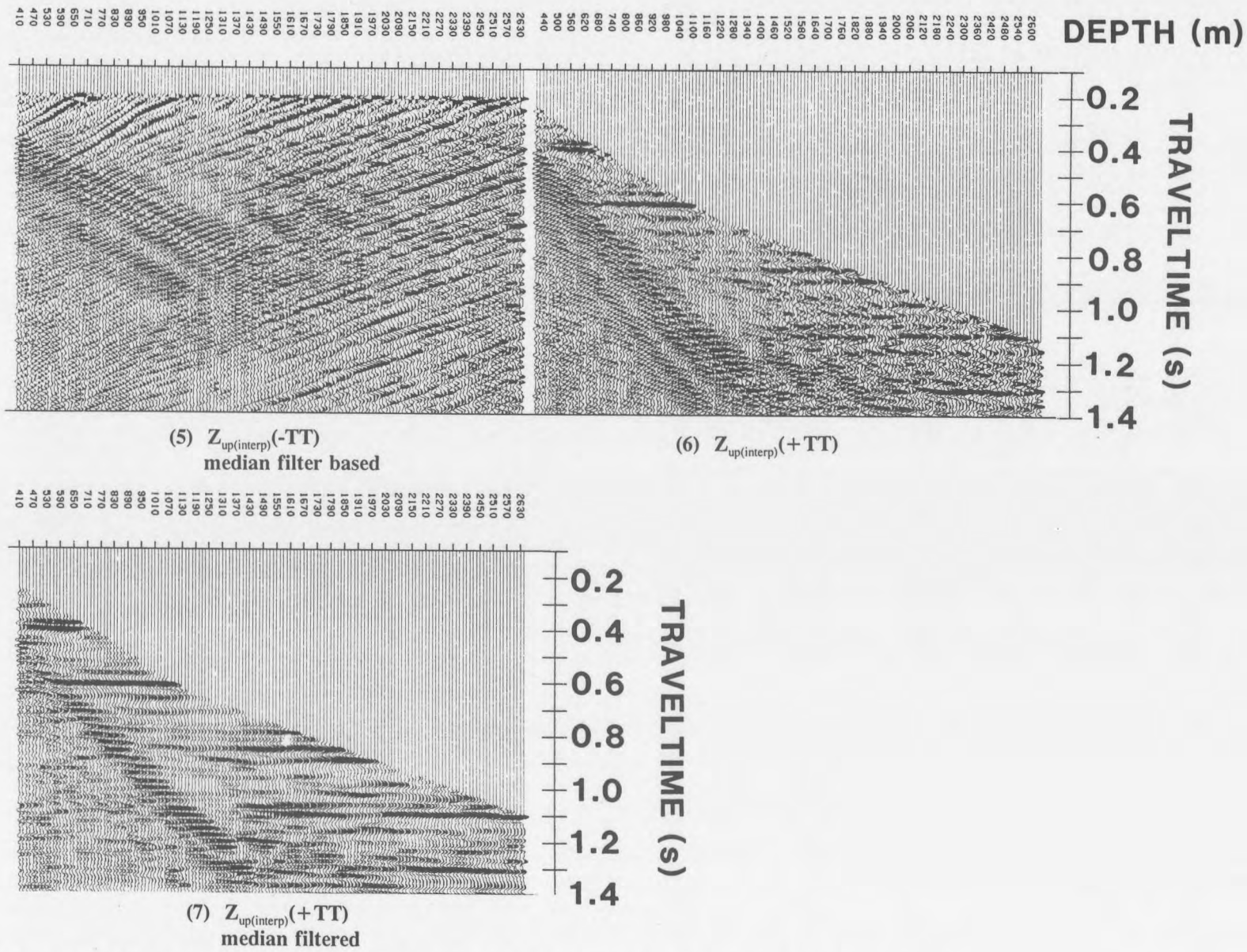

Figure 2.34B Panels 5 to 7 of the τ-**P** based wavefield separation IPP using the interpolated **Z(FRT)** tubewave contaminated data.

The F-K plot of the interpolated $\mathbf{Z_{(interp)}(FRT)}$ data is shown in Figure 2.35. The interpolation method used on the **Z(FRT)** data was a two-part operation where the up- and the downgoing waves were separated, interpolated and merged to create the $\mathbf{Z_{(interp)}(FRT)}$ data. This procedure is equivalent to imposing cutoff slownesses for both the up- and downgoing wavefields during the forward τ-P transformations. This translates into the two "accept" F-K zones as is shown in Figure 2.35.

2.2.5.6 Future directions for τ-P filtering in wavefield separation

The τ-P filtering and IPP's shown in sections 2.2.5.2 to 2.2.5.5 have attempted to familiarize the reader with the many roles that the τ-P filtering can play within wavefield separation. When interactive τ-P muting has become a common processing tool, then interactive interpretive processing can be routinely performed to assist in the examination and elimination of multiple reflections (Hu and McMechan, 1987). If we are limited to slowness filtering (specifying slowness cutoffs during the forward τ-P transformation), then the method will suffer the same limitations as in pie-slice F-K filtering.

The τ-P data can be transformed into the frequency-P domain. In this domain, the tubewave events can easily be muted using interactive processing (Hu and McMechan, 1987). The mute parameters are then used in the processing runstream and used in a combined τ-P and frequency-P IPP.

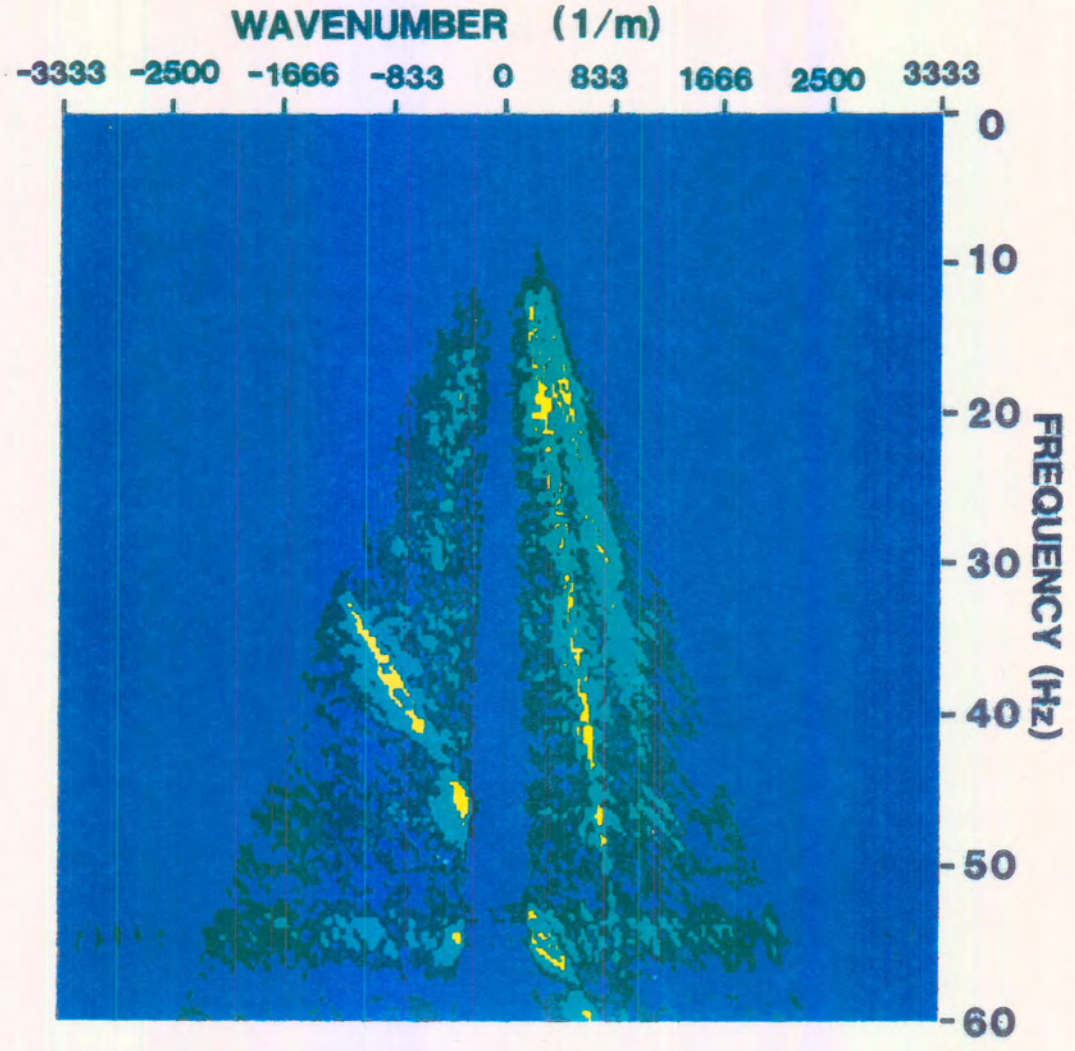

Figure 2.35 F-K plot of the interpolated **Z(FRT)** data shown in panel 1 of Figure 2.34.

2.2.6 VSP deconvolution and corridor stacks

The procedure of VSP or "up over down" deconvolution (Hubbard, 1979; Gaiser et al., 1984) was introduced in chapter 1. The term "up over down" refers to the computational procedure of the temporal frequency spectrum of $\mathbf{Z_{up}(-TT)}$ data being divided by the temporal frequency spectrum of $\mathbf{Z_{down}(-TT)}$ data to perform the deconvolution in the Fourier domain. If the spectrum of $\mathbf{Z_{down}(-TT)}$ is divided by itself (in the band limited sense), this would result in a zero phase band-limited "multiple free" delta function (Gaiser et al., 1984).

For interpretive processing, the following questions are posed:

(1) are the multiples attenuated ?

(2) are the underlying primary events preserved ?

(3) has the deconvolution processing added unwanted noise ? and

(4) what are the origins of the multiple events ?

In this section, the following IPP's are developed

(1) deconvolution IPP: the $\mathbf{Z_{up}(+TT)}$ and $\mathbf{Z_{up(decon)}(+TT)}$ can be compared directly to evaluate the effect of the deconvolution process on the upgoing events;

(2) $\mathbf{Z_{up}(+TT)}$ data inside and outside corridor stacks: the $\mathbf{Z_{up}(+TT)}$, inside and outside corridor stacks and the muted data that go into the stacks can be compared to facilitate multiple identification; and

(3) $\mathbf{Z_{up(decon)}(+TT)}$ data inside and outside corridor stacks: the deconvolved data and the corridor stacks can be used to evaluate the effect of the deconvolution on multiple suppression.

2.2.6.1 Deconvolution IPP

A VSP deconvolution IPP is presented in Figure 2.36 using the Fort St. John Graben case study near offset data (Hinds et al., 1991a; Hinds et al., 1993a and 1994b; Hinds et al., 1994c). Panels 1 and 2 are the $\mathbf{Z_{up}(+TT)}$ and $\mathbf{Z_{up(med)}(+TT)}$ data, respectively. These nondeconvolved data clearly show the multiples (highlighted in yellow on panels 1 and 2) and will be compared to the deconvolved **+TT** data. The $\mathbf{Z_{down}(-TT)}$ data in panel 3 shows the downgoing event multiple pattern (all of the downgoing events recorded after the arrival of the first break wavelet). To evaluate any increases in the background noise level due to the deconvolution process, the $\mathbf{Z_{up}(-TT)}$ and $\mathbf{Z_{up(decon)}(-TT)}$ data are shown in panels 4 and 5 (Fig. 2.36) can be compared. The $\mathbf{Z_{up(decon)}(+TT)}$ and $\mathbf{Z_{up(decon;med)}(+TT)}$ data are shown in panels 6 and 7.

The first step in the interpretive processing procedure is the detailed interpretation of similar events in panels 2 and 7. A highlighted (in orange) primary event (peak) at 0.595 s (+TT) in panel 2 is severely interfered with by the series of multiple events associated with Spirit River event. The primary event is preserved and continuous across the entire suite of traces in panels 6 and 7.

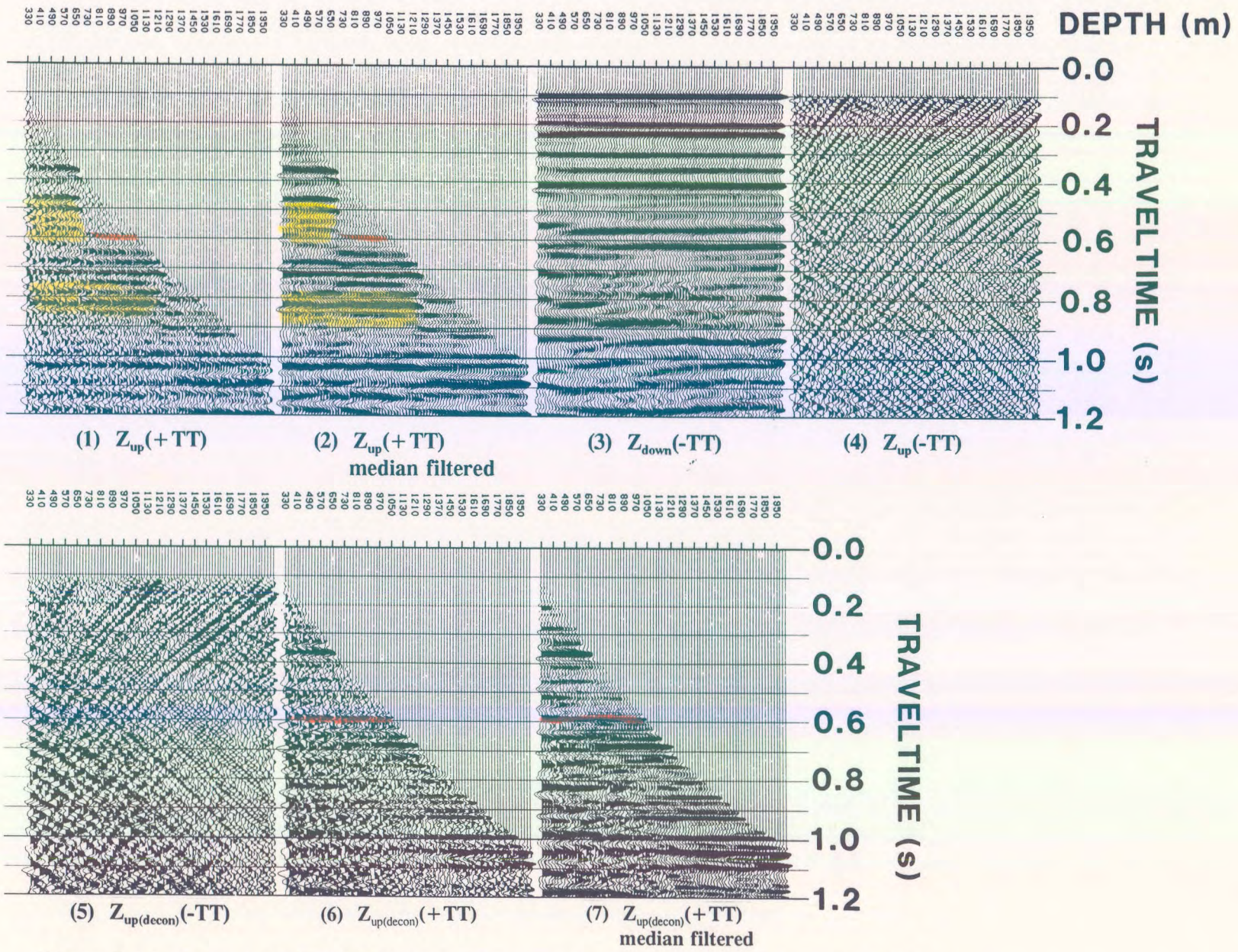

Figure 2.36 Deconvolution IPP for the Fort St. John Graben data (Hinds et al., 1993a). Compare panels 2, $Z_{up}(-TT)$, and 7, $Z_{up(decon)}(-TT)$, to evaluate the attenuation of the multiples seen on panel 2.

2.2.6.2 Corridor stack IPP's

A more detailed investigation into the success of the VSP deconvolution process can be achieved using the corridor stack IPP. The basic premise behind the use of the inside and outside corridor stacks is shown in Figure 2.37 (Hinds et al., 1989a). The time delays between a primary event and associated upgoing multiples are key factors in the interpretation panels designed to facilitate the identification of multiples in the $\mathbf{Z_{up}(+TT)}$ data.

Interpreted primary upgoing events intersect the first break curve. Upgoing multiples are recorded later in time at sonde locations above the bottom generating interface due to the added traveltime delay present in the surface generated or interbed multiples. In the $\mathbf{Z_{up}(+TT)}$ data (Fig. 2.37), the multiple of a primary reflection is interpreted later in time than the primary event. The upgoing multiple is recorded on the data traces of the shallowest depth down to the depth of the bottom generating interface.

A data corridor of multiple-free upgoing event data will exist immediately in the area of the first break curve of the $\mathbf{Z_{up}(+TT)}$ data since the upgoing multiples do not intersect the first break curve. Primary events will dominate a horizontal sum of the "outside corridor" of $\mathbf{Z_{up}(+TT)}$ data (Fig. 2.37). If a horizontal sum is performed between the corridor line in the opposite direction from the first break curve ("inside corridor"), both multiples and primary events (if not destructively interfered with by multiples generated at shallower interfaces) will be part of the inside corridor sum (Fig. 2.37).

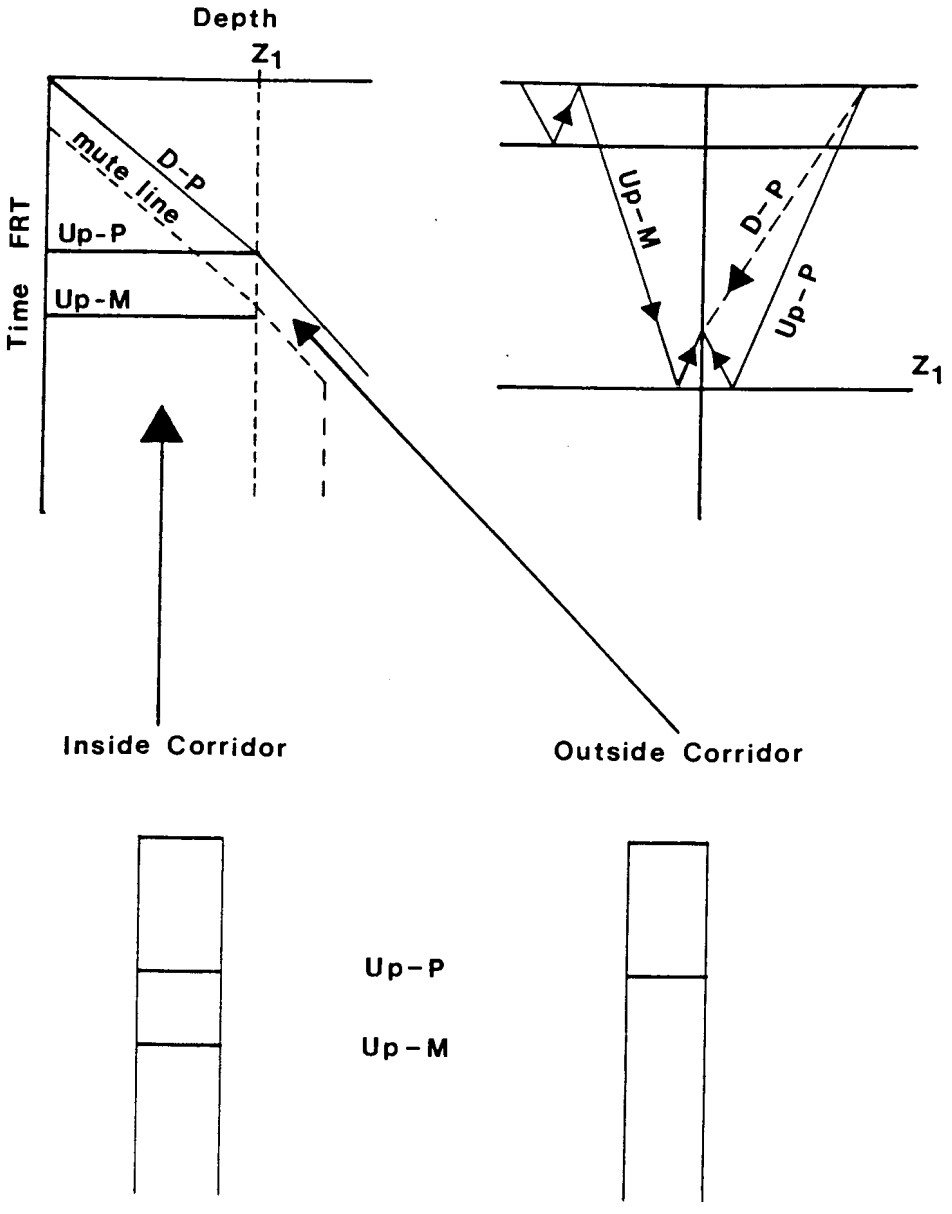

Figure 2.37 The schematic definition of the outside and inside corridor stack. The depth/(+**TT**) traveltime plot shows the downgoing primary (D-P), upgoing primary (Up-P), and upgoing multiple (Up-M) events with corresponding raypaths shown to the right of the traveltime plot. In the inside corridor, both the primary and multiple upgoing events are retained. For the outside corridor stack, only the primary event (Up-P) is seen after horizontally summing the events in the outside corridor. (after Hinds et al., 1989a).

To locate the interbed multiple generating interfaces, the up- and downgoing multiple pattern will reveal the top and bottom generating interfaces, respectively. The downgoing waves in (-TT) time will show the top generating interface and the upgoing waves in (+TT) time reveal the bottom generating interface. This is illustrated in Figure 2.38. The simplistic $\mathbf{Z_{down}(-TT)}$ and $\mathbf{Z_{up}(+TT)}$ diagrams in Figure 2.38B and C illustrate the location of the up- and downgoing primary and multiple events. The two data panels can be used to determine the origin of the multiple events.

The corridor stack IPP consists of (Hinds et al., 1989a; Hinds et al., 1994c):

(1) input $\mathbf{Z_{up}(+TT)}$ data;

(2) muted $\mathbf{Z_{up}(+TT)}$ before the horizontal summations are performed;

(3) inside and outside corridor stacks.

2.2.6.3 $\mathbf{Z_{up}(+TT)}$ Corridor stack IPP

The corridor stack IPP for the $\mathbf{Z_{up}(+TT)}$ data is shown in Figure 2.39. Near offset $\mathbf{Z_{up}(+TT)}$ data for the Fort St. John Graben case study (Hinds et al., 1991a; Hinds et al., 1993a; Hinds et al., 1994c) are displayed in panel 1. Two sets of multiple events are highlighted in red. This interpretation is carried over to the muted $\mathbf{Z_{up}(+TT)}$ data in panel 2. This panel contains the data that will go into the inside corridor sum (panel 3).

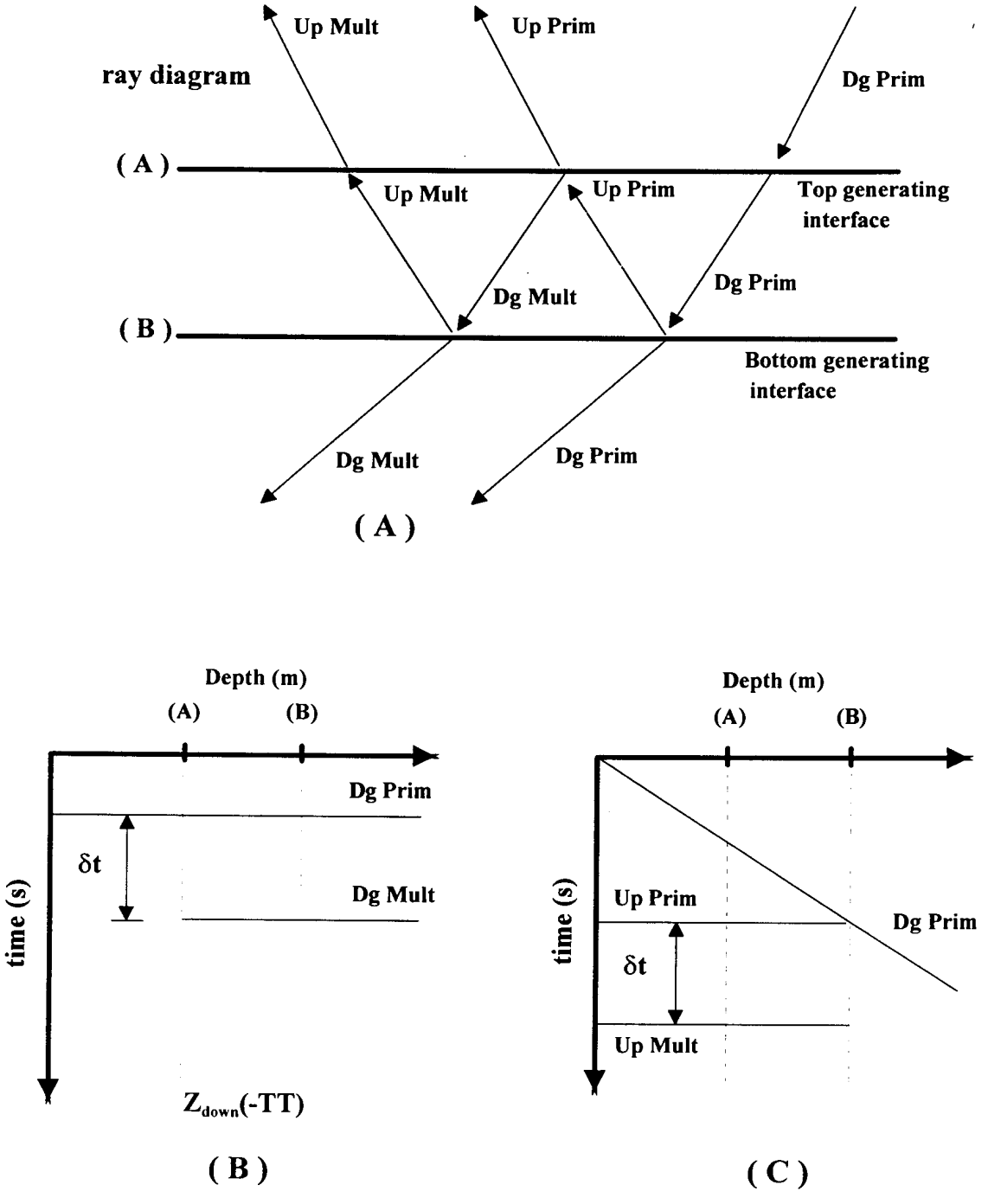

Figure 2.38 Ray and depth/time plots, Z_{down}(-TT) and Z_{up}(+TT), showing the top and bottom generating interfaces for interbed multiples (modified from Hinds et al., 1989a).

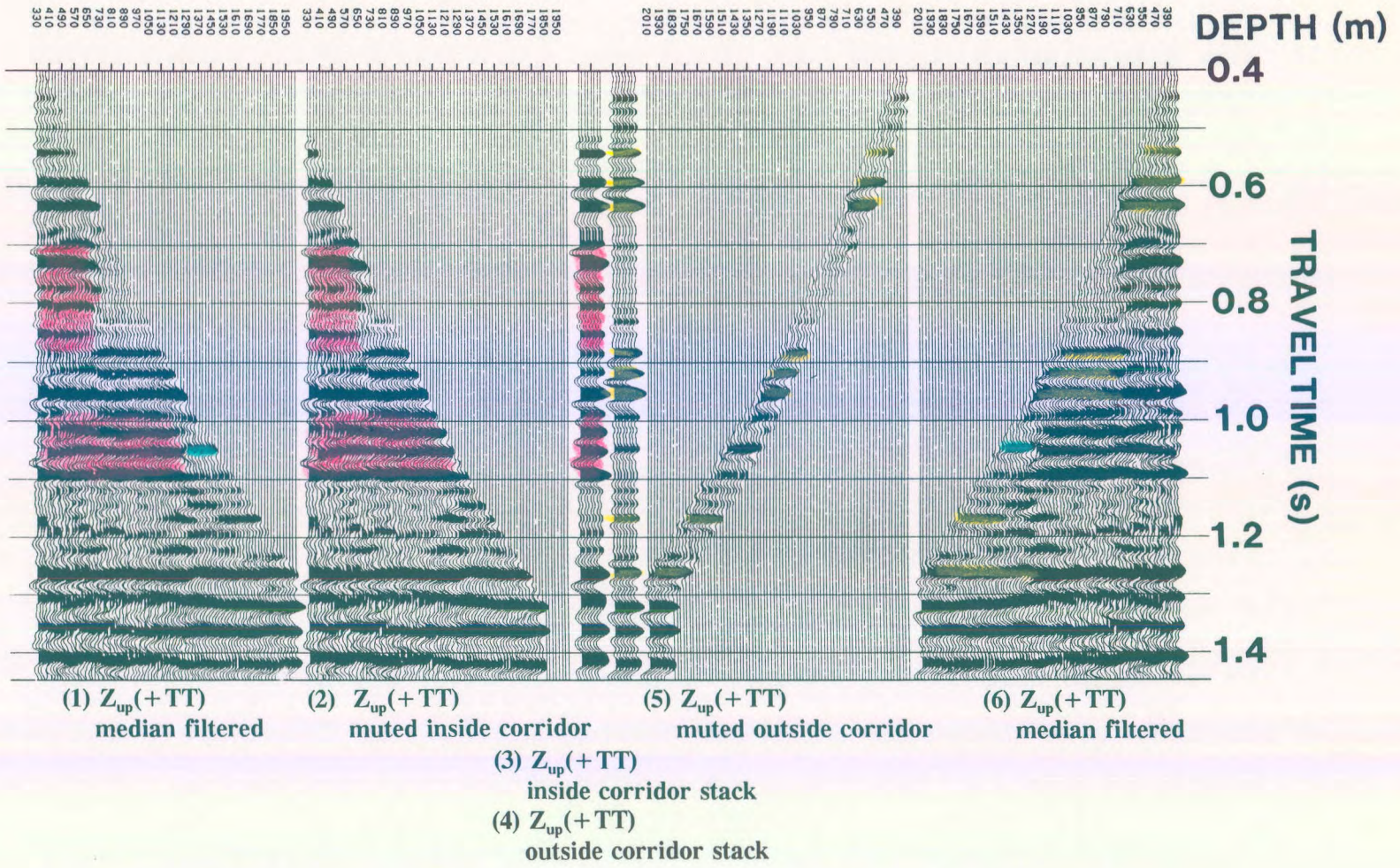

Figure 2.39 Corridor stack IPP of the Fort. St. John Graben $Z_{up}(+TT)$ data (Hinds et al., 1993a). Note the high amplitude multiple events at 0.7-0.8 s and 1.0-1.1 s on the inside corridor stack.

It was stated above that the inside corridor sum will contain multiples and primaries. To see this, the outside corridor sum data in panel 4 are placed next to the inside corridor sum data in panel 3. The multiple events highlighted in red in panel 3 do not appear in the outside corridor stack of panel 4; however, the primary events (shown in yellow) are common to both corridor stack data in panels 3 and 4.

The outside corridor mute data shown in panel 5 contains only primary events (highlighted in yellow at 0.6 s, 0.9-1.0 s, 1.1-1.2 s and at 1.25 s). The events below 1.3 s cannot be interpreted to be either multiple or primaries as there is no longer a first break curve at those recording times. The data in panels 3 and 4 in Figure 2.39 can be used to reliably interpret the multiple and primary event content of the $\mathbf{Z_{up}(+TT)}$ data.

2.2.6.4 $\mathbf{Z_{up(decon)}(+TT)}$ Corridor stack IPP

The effect of VSP deconvolution processing on $\mathbf{Z_{up}(+TT)}$ data can be determined by interpreting a corridor stack IPP that uses the $\mathbf{Z_{up(decon)}(+TT)}$ as input. Ideally, the data in both the inside and outside corridor stacks of the $\mathbf{Z_{up(decon)}(+TT)}$ data should be multiple free if the deconvolution was successful. These stacks can be compared with the $\mathbf{Z_{up}(+TT)}$ outside corridor stacks of Figure 2.39 to interpret the introduction of any deconvolution-generated noise to the data.

In Figure 2.40, the corridor stack IPP for $\mathbf{Z_{up(decon)}(+TT)}$ data is presented. The corridor stacks (panels 3 and 4) differ where the deconvolution could not totally attenuate the

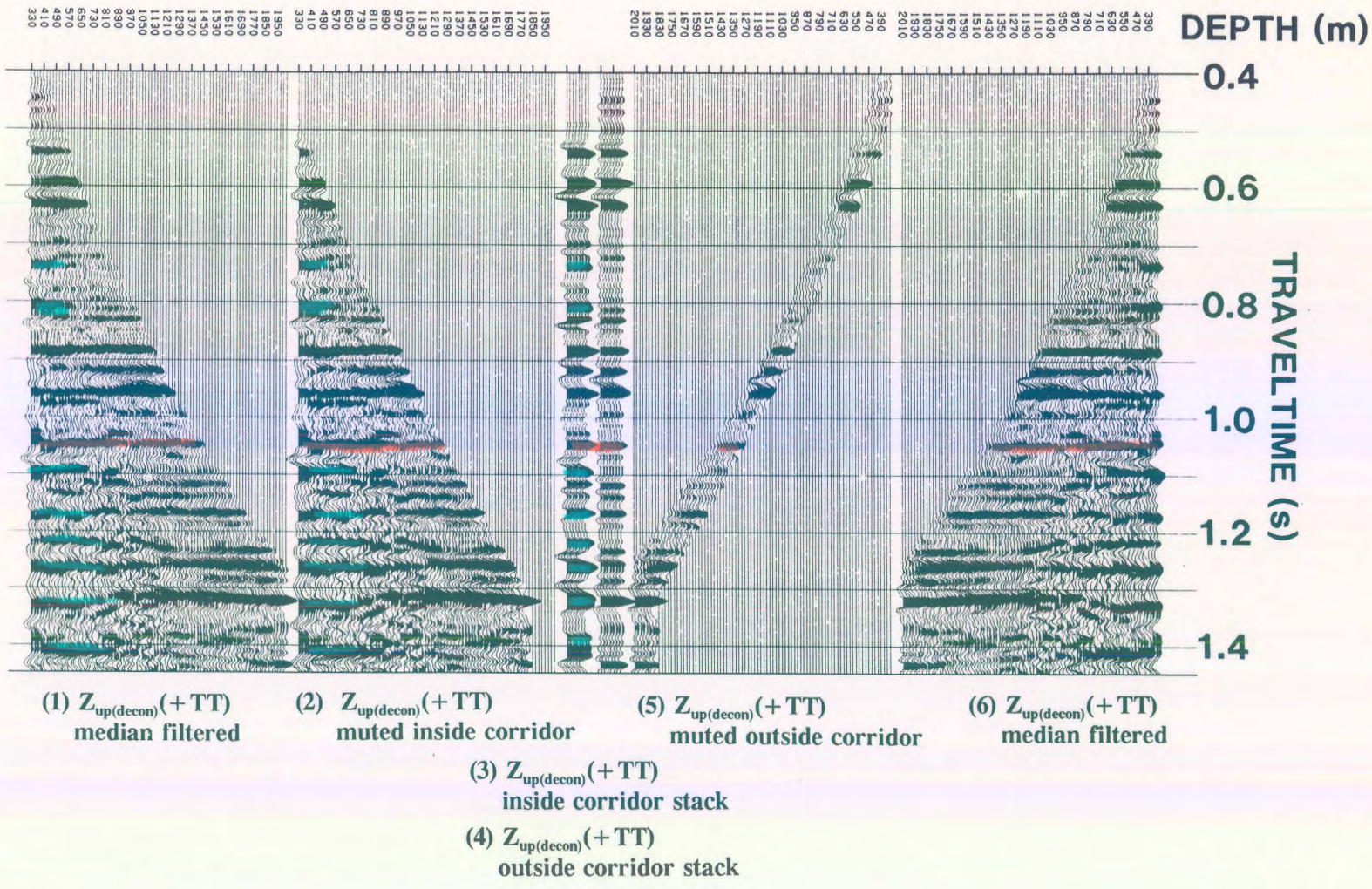

Figure 2.40 Corridor stack IPP of the Fort. St. John Graben $Z_{up(decon)}(+TT)$ data (Hinds et al., 1993a). Residual multiple events are present on the corridor stacks; such as the peak at 0.74 s on panel 3.

multiples on the shallow traces. These remnant multiple events have been highlighted (in blue) on all of the panels of Figure 2.40. A prominent primary highlighted on Figure 2.40 has been enhanced by the deconvolution at 1.05 s. On Figure 2.39, the same highlighted primary event (highlighted in blue) can only be detected at 1.05 s on the 1270 m trace and out to the first break curve. The remainder of the primary event at 1.05 s in Figure 2.39 is destructively interfered with by an upgoing multiple event (coloured red) occurring at the same time.

The outside corridor stack for the $\mathbf{Z_{up}(+TT)}$ and $\mathbf{Z_{up(decon)}(+TT)}$ data are similar indicating that the deconvolution process did not add appreciable amounts of deconvolution noise within the outside data corridors. The $\mathbf{Z_{up(decon)}(+TT)}$ inside corridor stack is different from the outside corridor stack of the same data between 1.2 to 1.3 s. This appears to be caused by a failure of the deconvolution on the shallow traces between those times; however, the interpretation of the near offset data proceeded using the remainder of the deconvolved traces between 1.2 to 1.3 s (traces deeper than 1210 m).

The use of the corridor stack IPP does not end there. In a production processing run, one would take the two IPP paper displays and fold them both in between panels 3 and 4. These are overlain onto the surface seismic section with the same time scale. A comparison between the VSP corridor stacks and surface seismic events can assist in interpreting where the CDP stacking method has not attenuated the multiples. Later in the chapter, the inside and outside corridor stacks will be used as part of the integrated interpretation display (IID) which will bring together a variety of exploration data.

2.3 Far offset data processing IPP's

In this section, the far offset processing will be reviewed and case studies showing the use of interpretive processing within far offset processing will be illustrated. The "normal" far offset processing will consist of

(1) polarization of the **X(FRT)** and **Y(FRT)** data into **HMAX(FRT)** and **HMIN(FRT)** data: the **HMAX(FRT)** data is the projection of the **X(FRT)** and **Y(FRT)** data into a plane defined by the well and the source location;

(2) polarization of the **HMAX(FRT)** and **Z(FRT)** data into **HMAX'(FRT)** and **Z'(FRT)** data: the **HMAX'(FRT)** data will be polarized in the direction of source and the **Z'(FRT)** data will be orthogonally polarized to **HMAX'(FRT)**;

(3) wavefield separation of the **Z'(FRT)** and **HMAX'(FRT)** data into $\mathbf{Z'_{up}(FRT)}$ and $\mathbf{HMAX'_{up}(FRT)}$ data;

(4) wavefield separation of the **HMAX'(FRT)** data into $\mathbf{HMAX'_{down}(FRT)}$ data: this will be used to deconvolve the final output, $\mathbf{Z''_{up}(FRT)}$ into $\mathbf{Z''_{up(decon)}(FRT)}$;

(5) derotation (Hinds et al., 1989a) of the $\mathbf{Z'_{up}(FRT)}$ and **HMAX'(FRT)** data into $\mathbf{Z_{up(derot)}(FRT)}$ and $\mathbf{HMAX_{up(derot)}(FRT)}$ data;

(6) time-variant polarization of the $\mathbf{Z_{up(derot)}(FRT)}$ and $\mathbf{HMAX_{up(derot)}(FRT)}$ data into

Z"$_{up}$(FRT) and **HMAX"$_{up}$(FRT)** data;

(7) VSP-CDP or migration of the **Z"$_{up}$(+TT)** data into the **+TT** versus offset from the well domain.

In the interpretation of the far offset IPP's, a number of crucial observations are being made. Some of the questions are:

(1) do the **X**, **Y**, and **Z** data obey the assumptions behind the time invariant polarizations reviewed in chapter 1 (section 1.4.3) ?

(2) what are the origins of noise seen on the data ?

(3) how is the noise being propagated onto the output data panels following each processing stage ?

(4) what is the multiple event content in the VSP-CDP or migrated data ?

(5) do the multiples in the VSP-CDP or migrated data interfere with the interpretation of primary events ?

(6) Can the primary and multiple events be differentiated since reflectors imaged away from the well may not intersect the first break curve ?

These questions will be posed again and again during the interpretive processing of the far offset IPP's. The partitioning of the energy of the various wavefields onto the polarization axis and time-variant "axis" will be illustrated using the far offset data contained in Chapter 4 (Ricinus carbonate reef case study; Hinds et al., 1989a; Hinds et al., 1993c; Hinds et al.,

1994c), Chapter 5 (Fort St. John Graben case study; Hinds et al., 1991a; Hinds et al., 1993a and 1994b; Hinds et al. 1994b) and Chapter 6 (Simonette carbonate reef case study; Hinds et al., 1991b; Hinds et al., 1993b and 1994c). The success and failures of far offset deconvolutions will be illustrated using Chapter 4 and 6 data.

A review of the Ricinus carbonate reef case study polarization IPP's will show:

(1) the results after using "normal" processing runstreams (see section 2.1);

(2) an analysis of the noise on the polarized results; and

(3) the modification of the processing runstream to enhance the interpretation of the $\mathbf{Z"_{up}(+TT)}$ data.

2.3.1 Time invariant polarization: isolation of the downgoing P-wave

In this section, the **Z(FRT)**, **X(FRT)** and **Y(FRT)** data are polarized to isolate the downgoing P-wave events onto a single data panel, **HMAX'(FRT)**. The orthogonal data projection, **Z'(FRT)**, was considered in the past to contain predominantly upgoing P-wave events. Interpretation would be performed on the wavefield separated $\mathbf{Z'_{up}(+TT)}$ data and on the VSP-CDP transformed upgoing events. In the next section, time variant polarization will be used to isolate the upgoing P-wave events onto a single output panel, $\mathbf{Z"_{up}(+TT)}$.

The polarization analysis presented in this section use hodogram derived rotation angles derived in a time invariant sense. The hodogram analysis is performed on a single window of data around the first breaks of the two input VSP data to yield a single polarization angle.

In the next section, the polarization angle for a pair of input traces is allowed to vary in time along the traces.

In Figure 2.41, the time invariant polarization IPP for the far offset data (700 m offset source location; source location in a direction of 307° from the well) of the Fort St. John Graben case study (Chapter 5) is shown. For reference within this chapter and chapter 5, the dataset will be referred to as the FSJG1 data.

The **X(FRT)**, **Y(FRT)**, and **Z(FRT)** data are shown in panels 1, 2, and 3, respectively. The downgoing P-wave events in the **Z(FRT)** data of panel 3 are highlighted in yellow. In comparison to the panels 1 and 2, the **Z(FRT)** data contain the majority of the downgoing P-wave events.

Primary downgoing P-wave energy is divided in varying amounts on the **X(FRT)** and **Y(FRT)** data shown in panels 1 and 2 (highlighted in yellow) indicating that the geophone sonde was rotating within the borehole during the acquisition of the data. However, the first break wavelet on the two panels show the most consistency for the bottom two-thirds of the borehole indicating that the sonde was rotating slowly during the acquisition at those depths.

The **Z(FRT)** data shown in panel 3 contains a diffraction event (highlighted in purple) in the lower left hand corner of the panel. This diffraction will be unfortunately partitioned onto all of the output data panels (see highlighted purple events in panels 5-7) as a result of further processing. Since these diffraction events are not polarizable in the same way that the up-

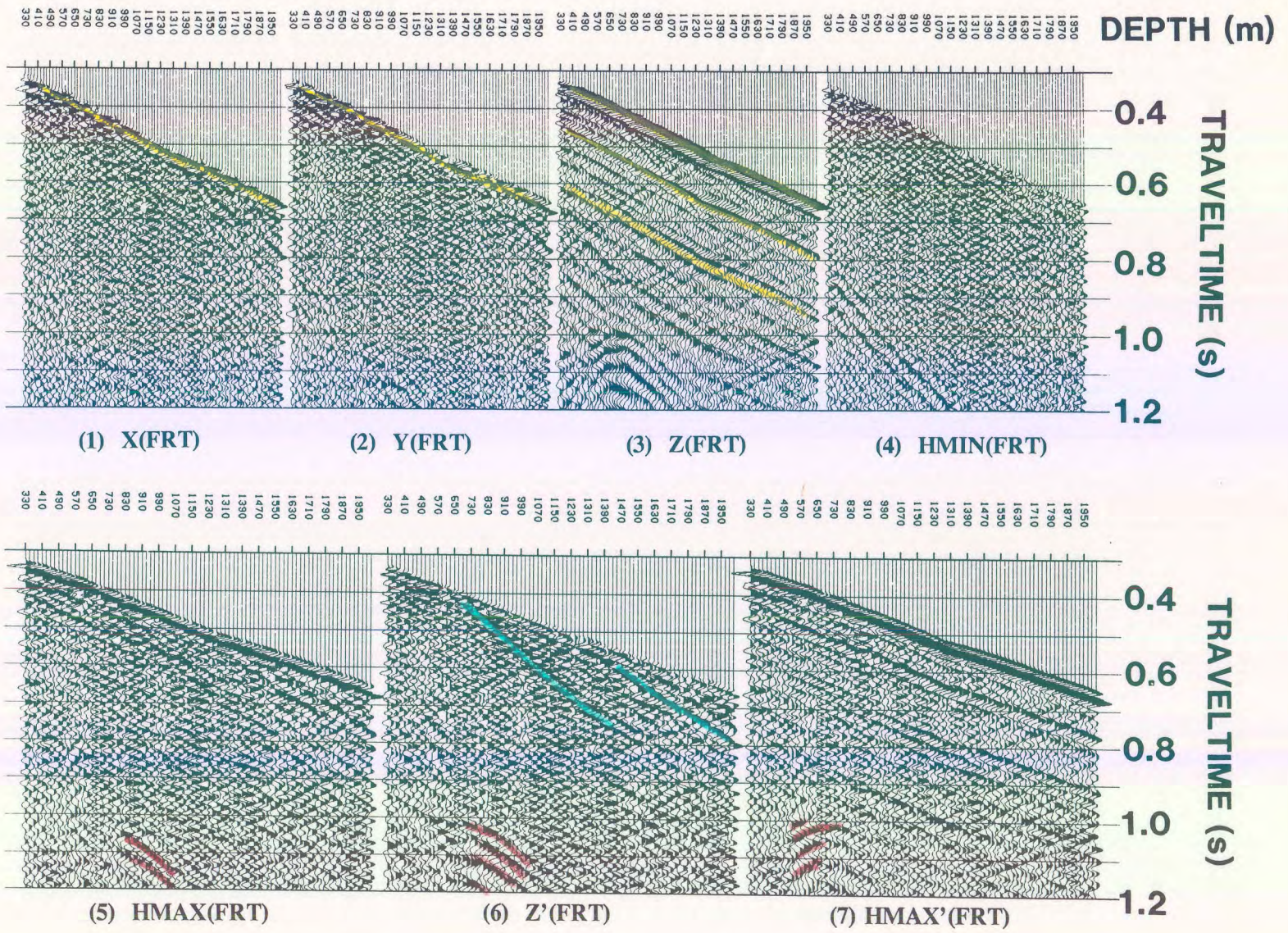

Figure 2.41 Hodogram-based polarization IPP for the Fort St. John Graben (FSJG1) far offset data (Hinds et al., 1993a). The downgoing P-wave events have been isolated on the **HMAX'(FRT)** data in panel (7).

and downgoing P-wave events are, interpretation will be performed "over" these "noise" events.

The result of hodogram based polarization analysis on the **X(FRT)** and **Y(FRT)** data and subsequent "single angle" rotation yields the **HMIN(FRT)** and **HMAX(FRT)** data shown in panels 4 and 5, respectively. The minor amount of downgoing P-wave events evident in the **X(FRT)** and **Y(FRT)** data shown in panels 1 and 2 have been isolated within the **HMAX(FRT)** data of panel 5.

The rotation of the **X(FRT)** and **Y(FRT)** data was performed using an interactive hodogram analysis program. A window of input data, from the **X(FRT)** and **Y(FRT)** data, centred around the first break of two input traces at the same depth recording level are shown in one portion of the screen. The trace data are colour coded so that hodogram points shown in another portion of the screen can be correlated to the traveltime of the trace data. This enables an interpretation of the hodogram plot. A least squares routine estimates the best straight line through the cloud of hodogram points. The **HMAX(FRT)** and **HMIN(FRT)** windowed results using the rotation angle determined by the least-squares fit is displayed onto another portion of the monitor. The user can now interactively alter the angle of the straight line through the hodogram cloud of points and the displayed window of **HMAX(FRT)** and **HMIN(FRT)** output traces (also centred around the first break) immediately change according to the updated rotation angle. The calculations which produce the **HMIN(FRT)** and **HMAX(FRT)** traces use the rotation matrix shown in the Appendix.

During the determination of the rotation angle using the hodogram plot and the various

screen displays, the aim is to:

(1) to maximize the amount of downgoing P-wave first break energy on the **HMAX** trace; and

(2) produce a consistent output polarity.

The polarity of the **HMAX(FRT)** data in panel 5 is consistent and minimal downgoing P-wave energy can be seen on the **HMIN(FRT)** data in panel 4. Mode-converted downgoing SV events are highlighted (in blue) on the **HMAX(FRT)** in panel 5.

The **Z'(FRT)** and **HMAX'(FRT)** data calculated using a hodogram analysis and subsequent rotation of the **HMAX(FRT)** and **Z(FRT)** data are shown in panels 6 and 7, respectively. The downgoing P-wave data are isolated onto the **HMAX'(FRT)** panel and the **Z'(FRT)** data contains mode-converted SV energy (highlighted in blue). Mode-converted SV downgoing events on the **Z'(FRT)** data appear to originate at the impedance boundaries at 690 m (Spirit River Formation; see Chapter 5) and the 1260 m (Nordegg Formation; see Chapter 5). Upgoing P events can be identified on panel 6 from the Nordegg reflector (highlighted in orange).

The diffraction event seen clearly on the **Z(FRT)** data has now been partitioned onto both the **HMAX'(FRT)** and **Z'(FRT)** data. Interestingly enough, the **HMAX'(FRT)** data contain the "upgoing" part of the diffraction and the **Z'(FRT)** data contain the "downgoing" part of the event.

2.3.2 Time variant polarization: isolation of the upgoing P-wave events

In this section, time variant polarization will be applied to the upgoing events from the **HMAX'$_{up}$(FRT)** and **Z'$_{up}$(FRT)** data to yield the **Z"$_{up}$(FRT)** data. The final interpretations are done on the **Z"$_{up}$(+TT)** and the VSP-CDP transformed and/or migrated **Z"$_{up}$(+TT)** data.

The time invariant polarizations performed in the previous section assumed that a single angle was adequate to polarize the up- and downgoing **Z(FRT)** and **HMAX(FRT)** event onto separate panels, **Z'(FRT)** and **HMAX'(FRT)**. The polarization angle needed to isolate (polarize) the upgoing P-wave onto the **Z"$_{up}$(FRT)** data is time variant. The angle of reflection from interfaces below the sonde change with depth as is shown in Figure 2.42. This implies that the incident angle of the upgoing P-wave events at a single geophone location changes accordingly with recording time.

The **Z'$_{up}$(FRT)** and **HMAX'$_{up}$(FRT)** data are a result of performing wavefield separation on the **Z'(FRT)** and **HMAX'(FRT)** data, respectively. The IPP for the time variant polarization of the FSJG1 far offset data is shown in Figure 2.43. The **Z'$_{up}$(FRT)** and **HMAX'$_{up}$(FRT)** data shown in panels 1 and 2, respectively, contain:

(1) upgoing P events (highlighted in orange);

(2) possible diffraction appear between 0.4 - 0.6 s (highlighted in brown); and

(3) mode converted downgoing shear wave events (highlighted in blue).

The **Z$_{up(derot)}$(FRT)** and **HMAX$_{up(derot)}$(FRT)** data shown in panels 3 and 4 are formed from **Z'$_{up}$(FRT)** and **HMAX'$_{up}$(FRT)** data by applying a rotation operation opposite to that used

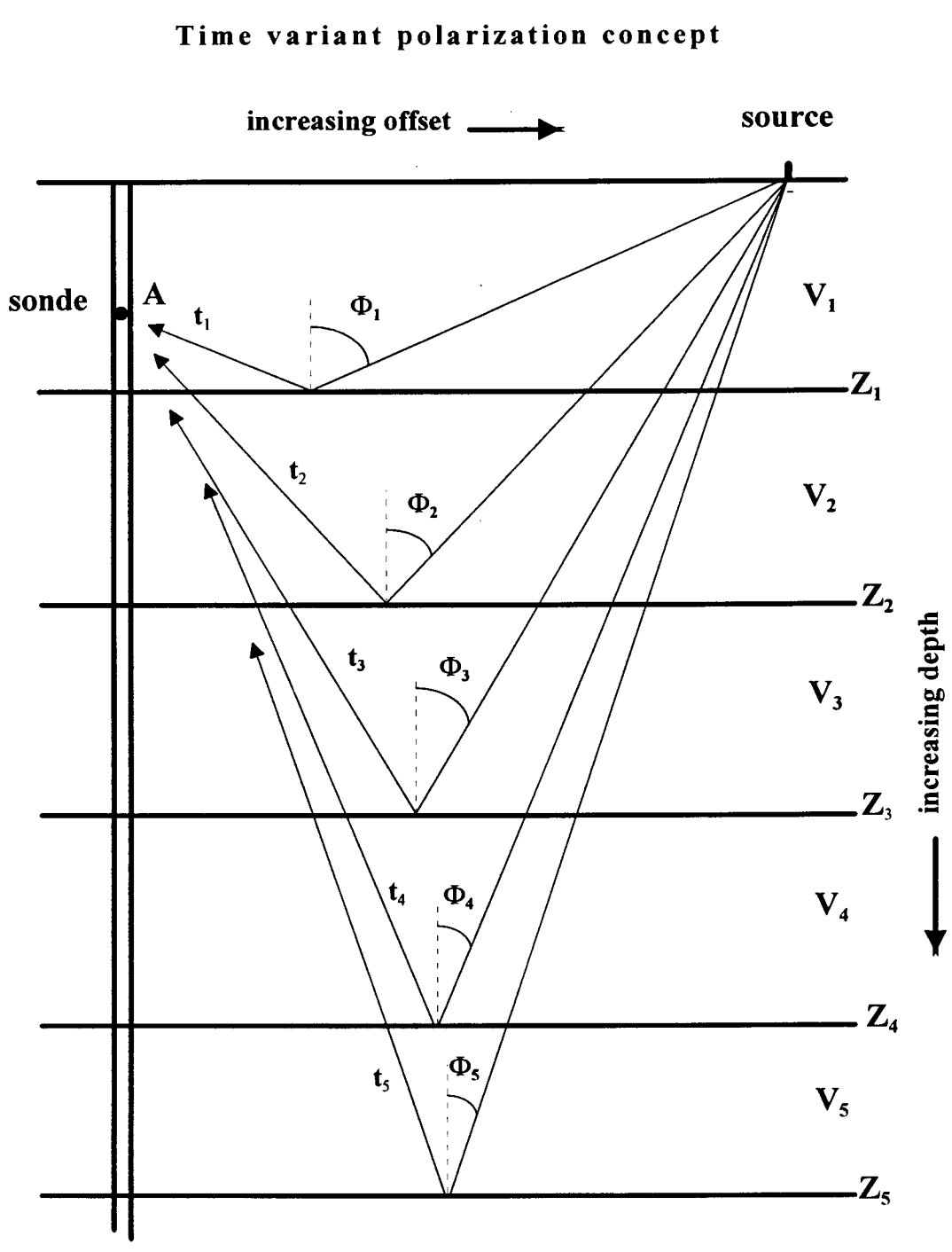

Figure 2.42 The reflection angle for upgoing raypaths emerging at the geophone at A from deeper interfaces decreases in comparison to the reflections from shallower interfaces. The Φ_i are the reflection angles, V_i are the layer velocities, Z_i are the layer depths and t_i are the raypath traveltimes to the sonde at **A.**

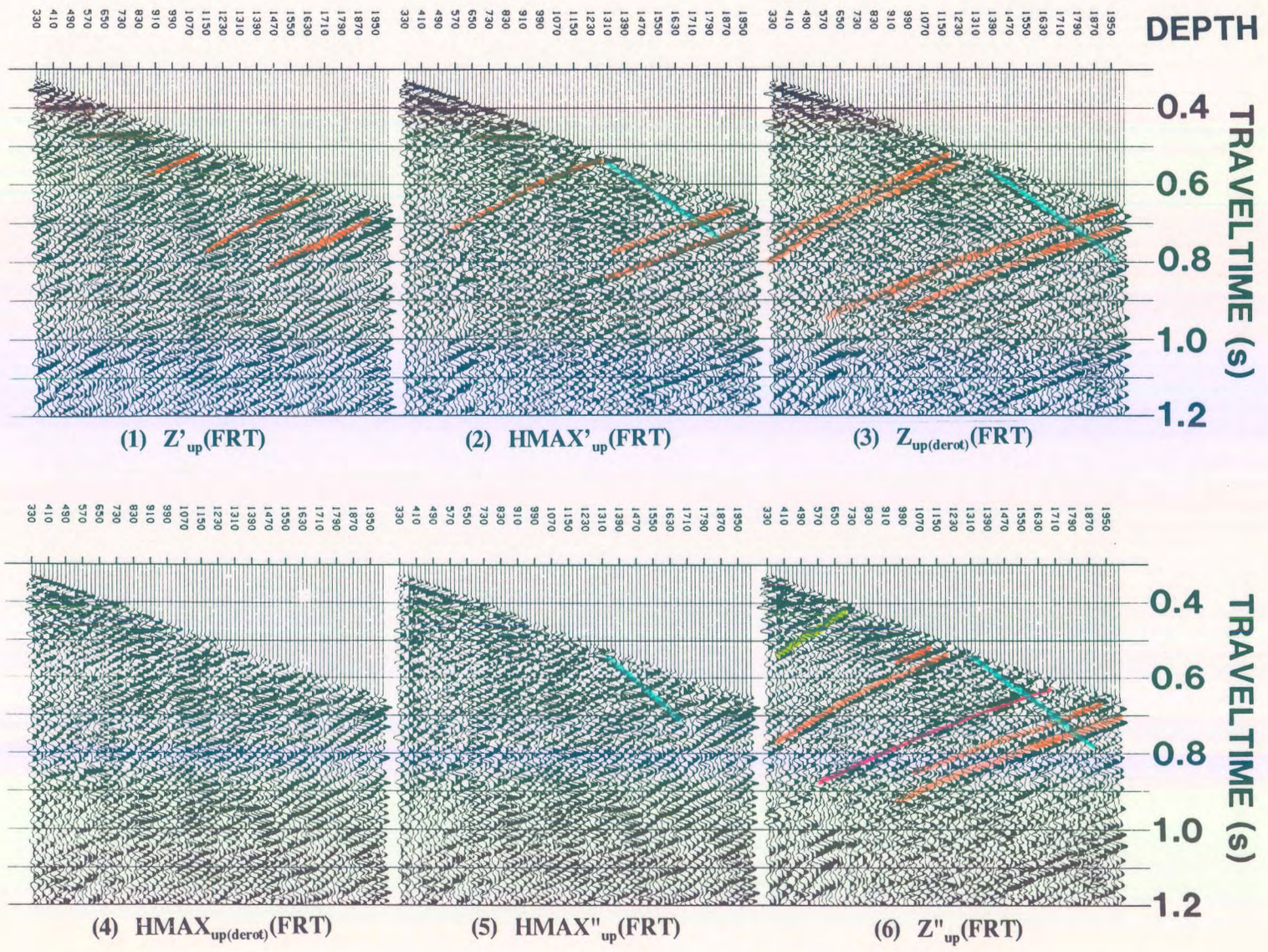

Figure 2.43 Time-variant polarization IPP for the Fort St. John Graben (FSJG1) far offset data (Hinds et al., 1993a). The upgoing P-wave events have been predominately partitioned onto the **Z"$_{up}$(FRT)** panel.

in calculating the **Z'(FRT)** and **HMAX'(FRT)** data. By inspection of panels 3 and 4, it appears as if this simple derotation is already isolating the upgoing P-wave events (highlighted in orange in panel 3).

The interval velocities and first break times from the near offset VSP data of the Fort St. John Graben case study are used to construct a model for ray-tracing. The first breaks (when the downgoing P-wave should reach an interface) and the velocity of the various interfaces (which will be used to propagate the upgoing reflections) are derived through simple calculations. The ray-tracing to the defined geophone locations (given the source offsets) will result in the (time,angle) pairs to be used in time-variant polarization (see Appendix). The result of the time-variant polarization is **HMAX"$_{up}$(FRT)** and **Z"$_{up}$(FRT)** shown in panels 5 and 6 (Fig. 2.43), respectively.

By inspection of panels 3 and 6 ($\mathbf{Z_{up(derot)}}$ and **Z"$_{up}$**), the downgoing (residual) SV events seen on panel 3 are now mapped jointly onto panel 5 and 6 (coloured in blue). The upgoing P event (coloured pink) originating near the 1750 m depth is more interpretable on the **Z"$_{up}$(FRT)** data in panel 6. The shallow Spirit River event (coloured green on panel 6) at 690 m which was not resolved on panels 1 to 4 can now be interpreted. Other upgoing events on the **Z"$_{up}$(FRT)** data have been coloured orange in panel 6.

2.3.3 VSP-CDP Transformation and Migration

In this section, the $\mathbf{Z''_{up}(FRT)}$ data are VSP-CDP transformed or migrated and the IPP designed to utilize interpretive processing is presented. The term VSP-CDP or "VSP-CDP mapping" refers to mapping the VSP data into a pseudoseismic section that displays coverage starting from the borehole out to the furthest reflection defined by the VSP data geometry and input velocity model (Wyatt and Wyatt, 1981; Millahn et al., 1983). The product of the VSP-CDP mapping has been called the VSPCDP (Hardage, 1985). The VSP-CDP and migration far-offset IPP for the FSJG1 data (chapter 5) is shown in Figure 2.44.

The $\mathbf{Z''_{up}(+TT)}$ and $\mathbf{Z''_{up(med)}(+TT)}$ data are shown in panels 1 and 2, respectively. The VSP-CDP (Dillon and Thomson, 1984) mapped $\mathbf{Z''_{up}(+TT)}$ data are shown in panel 3. Note that the horizontal axis for panel 3 (and 4) is not depth but offset distance from the well. The image of the reflectors on the VSP-CDP or migrated data is similar to how the reflectors would appear on a seismic section.

The IPP is completed with a Kirchhoff migrated version of the $\mathbf{Z''_{up}(+TT)}$ data shown in panel 4. The migrated data appear to be "smoother" than the VSP-CDP mapped data of panel 3. The events between 1.2 and 1.35 s display faulting. An example of the faulting is highlighted by the event in green and interpreted faults (in pink) on panels 3 and 4.

One of the most important interpreted events is a dominant peak (in blue) at 1.27 s which exists laterally from the well out to a distance of 55 to 75 m away from the well. The amplitude of the event attenuates rapidly at offsets beyond that point and may represent a

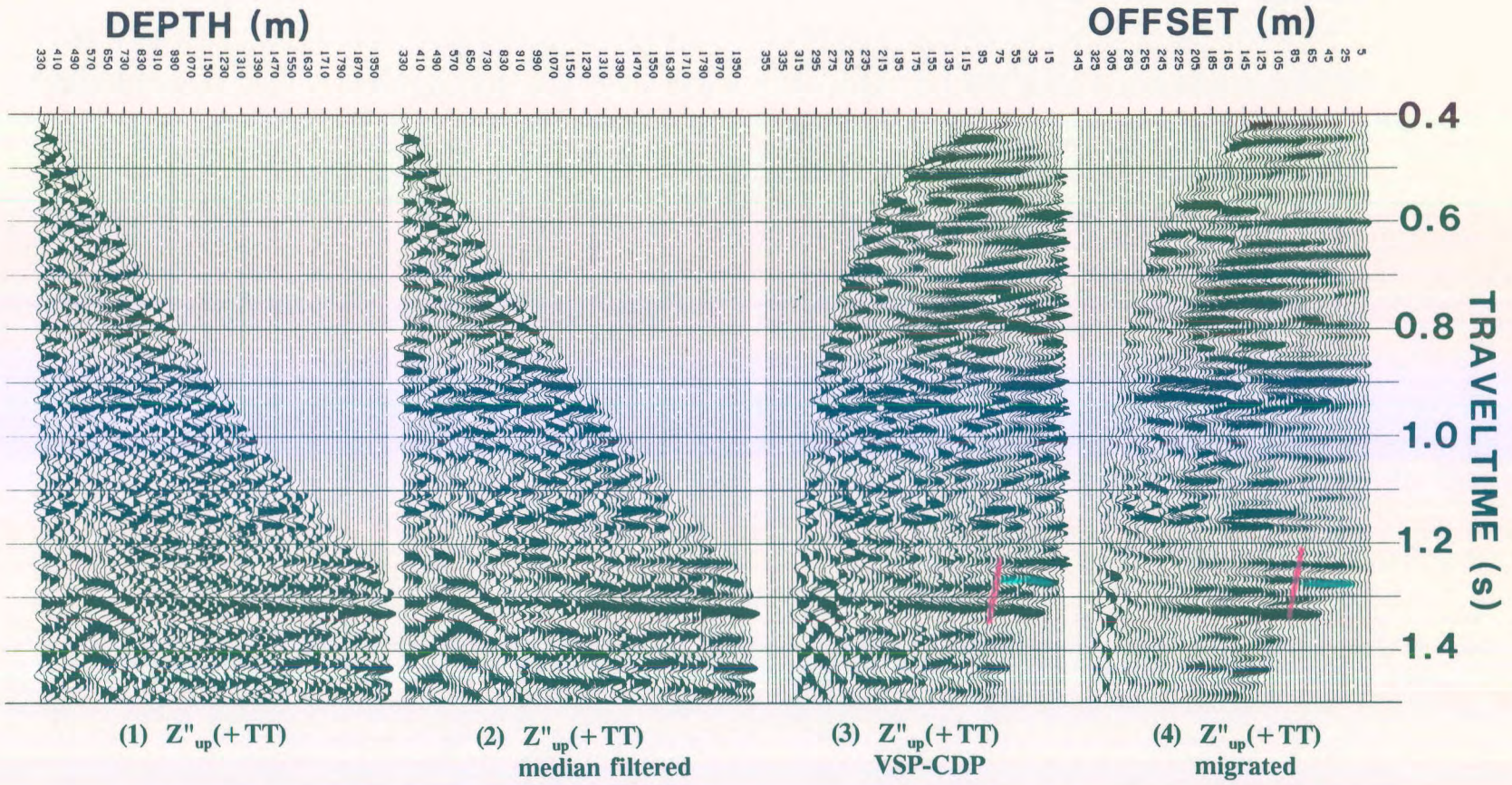

Figure 2.44 VSP-CDP and Kirchhoff migration IPP for the Fort St. John Graben (FSJG1) far offset data (Hinds et al., 1993a). Note the termination of the event (peak) on the VSP-CDP at 1.27 s (panels 3 and 4). The event exists only on offset traces 0-55 m.

possible facies change in the basal Kiskatinaw (chapter 5 and in Hinds et al., 1991a; Hinds et al., 1993a and 1994b; Hinds et al., 1994c). This observation is an important consideration for exploration. Beyond the interpreted fault (in pink) at a distance of 95 to 115 m offset from the well, the event appears to terminate.

The other far offset data for the Fort St. John Graben case study (source location offset of 741 m; location of offset source is East of the well) will be referred to as the FSJG2 data. Figures 2.45, 2.46, and 2.47 display the far-offset IPP's for the FSJG2 data.

By following the rotation processes on these figures, it can be interpreted that the event at 1.25 - 1.27 s on the VSPCDP and migrated $\mathbf{Z''_{up}(+TT)}$ data (coloured blue) in panels 3 and 4 of Figure 2.47 does not terminate near the well. The event is laterally more continuous than the same event on the FSJG1 data seen in panels 3 and 4 of Figure 2.44. Faulting (shown in pink) is also evident on the VSPCDP and migrated data in Figure 2.47 between 1.1 and 1.35 s.

2.3.4 Far offset deconvolution

In this section, the deconvolution of the far offset VSP data is reviewed and far offset deconvolution IPP's are presented. The process of far offset deconvolution is the spectral division of the $\mathbf{Z''_{up}(FRT)}$ data by the $\mathbf{HMAX'_{down}(FRT)}$ data to output the $\mathbf{Z''_{up(decon)}(FRT)}$ data.

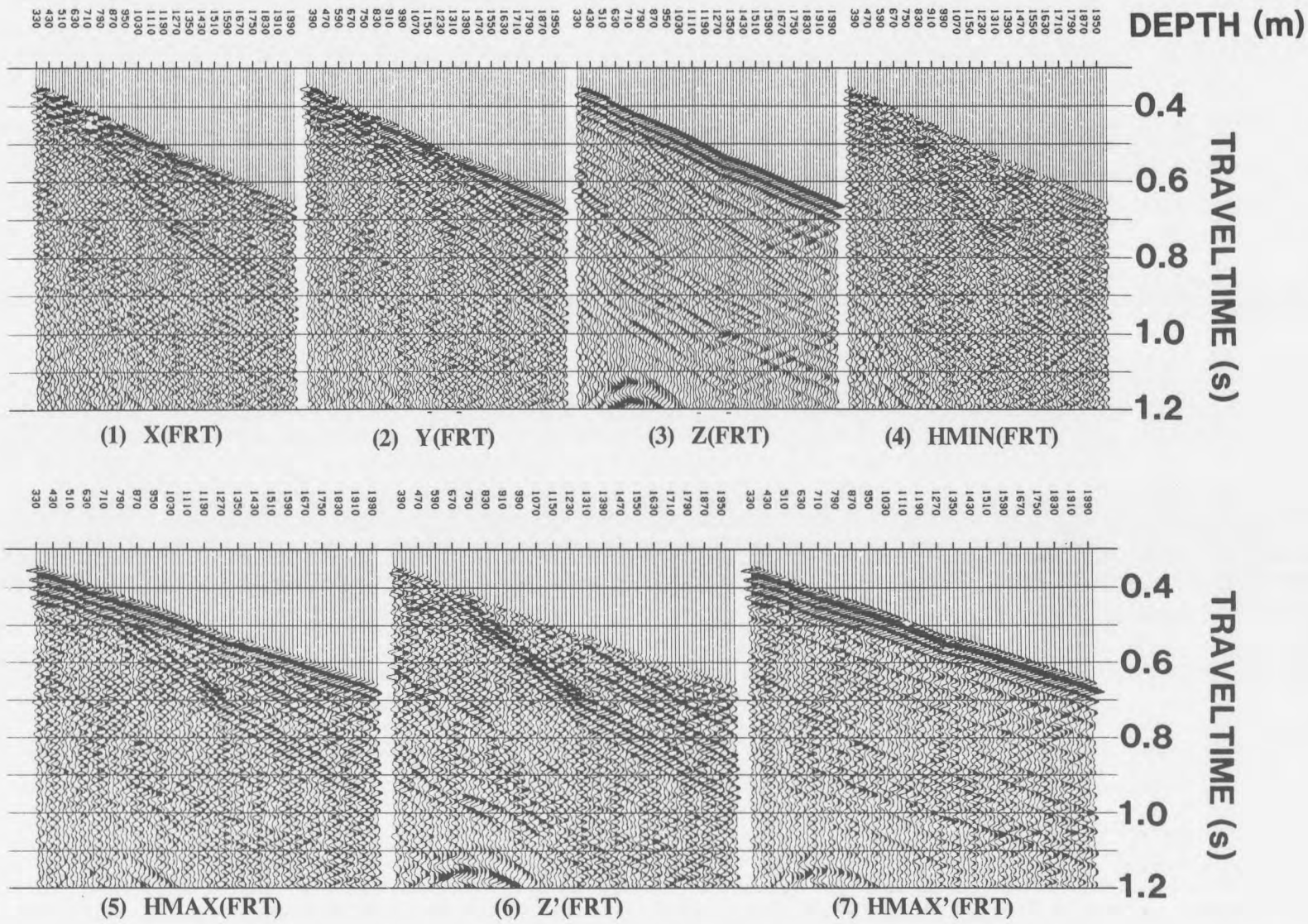

Figure 2.45 Hodogram-based polarization IPP for the Fort St. John Graben (FSJG2) far offset data (Hinds et al., 1993a). The downgoing P-wave events have been isolated on the **HMAX'(FRT)** data in panel (7).

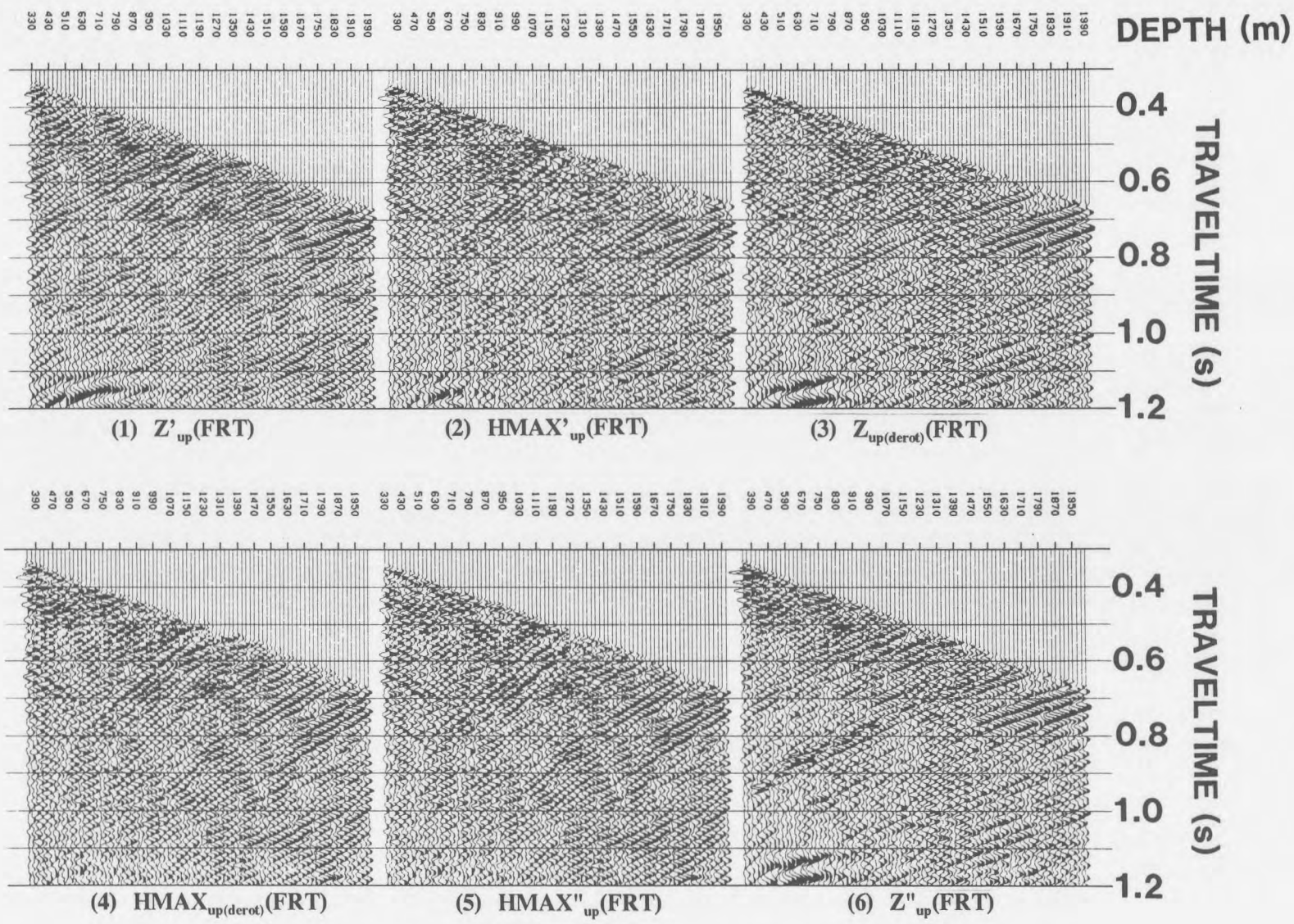

Figure 2.46 Time-variant polarization IPP for the Fort St. John Graben (FSJG2) far offset data (Hinds et al., 1993a). The upgoing P-wave events have been predominately partitioned onto the **Z"$_{up}$(FRT)** panel.

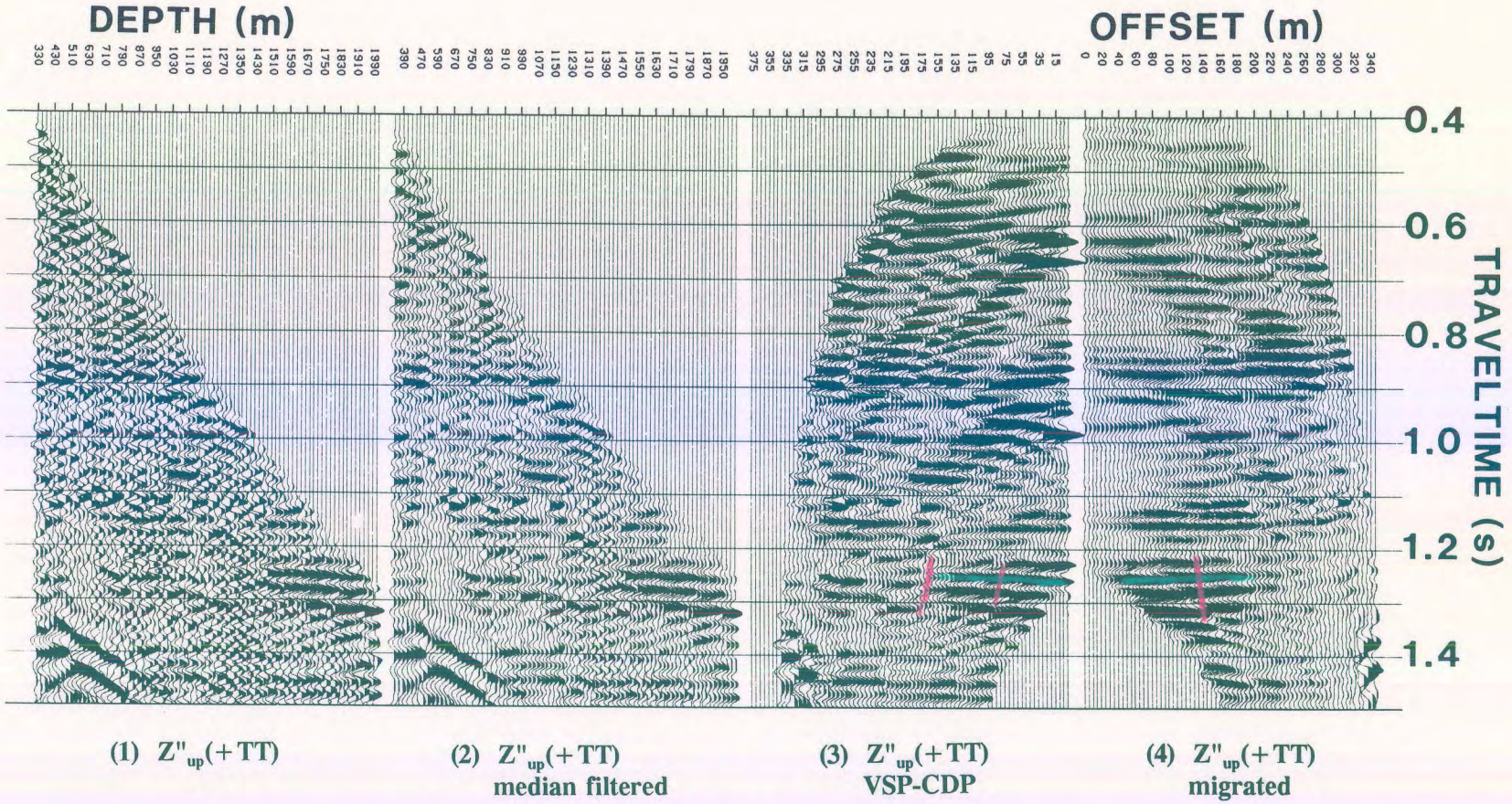

Figure 2.47 VSP-CDP and Kirchhoff migration IPP for the Fort St. John Graben FSJG2 far offset data (Hinds et al.,1993a). Note the continuity of the event (peak) on the VSP-CDP display at 1.27 s (from offset traces 0-55 m).

The VSP (far offset) deconvolution has not received attention in the literature because the decision to deconvolve the far offset is usually made after interpretation. Whereas, deconvolution of near offset VSP data would be done as a matter of course, the far offset deconvolution decision-making would follow the course of:

(1) searching for possible interfering multiples on the far offset $\mathbf{Z''_{up}(+TT)}$;

(2) confirming that the event is not a terminating reflector located away from the borehole;

(3) utilization of the $\mathbf{Z'_{down}(-TT)}$ data to deconvolve the $\mathbf{Z''_{up}(+TT)}$; and

(4) reconfirming the interpretation by comparing the data before and after deconvolution.

This illustrates the arduous task presented to the "interpreter/processor".

The VSP-CDP/migration IPP for the far offset data of the Simonette carbonate reef case study (Chapter 6; Hinds et al., 1991b; Hinds et al., 1993b and 1994c) is presented in Figure 2.48. The data contain destructively interfering multiples (coloured green). On panel 2, the off-reef carbonate (coloured "reef" purple; see chapter 6 or Hinds et al., 1993b and 1994c) starts at 1.96 s on the deepest trace and climbs onto the low-relief reef mid-way across the display rising up onto the peak event at 1.92 s (the transition being between depth levels 2470 - 2570 m).

There is an anomalous event (peak) at 1.8 s that does not seem to correspond to the geology interpreted from the sonic log. The Wabamun Formation (highlighted in red; see Chapter 6) event intersects the first break curve at 3020 m as a peak at 1.735 s in the $\mathbf{Z''_{up}(+TT)}$ data. Note that the anomalous event (the peak colored green for reference) between 1.77 - 1.81 s lies immediately under the Wabamun event and does not intersect the first break

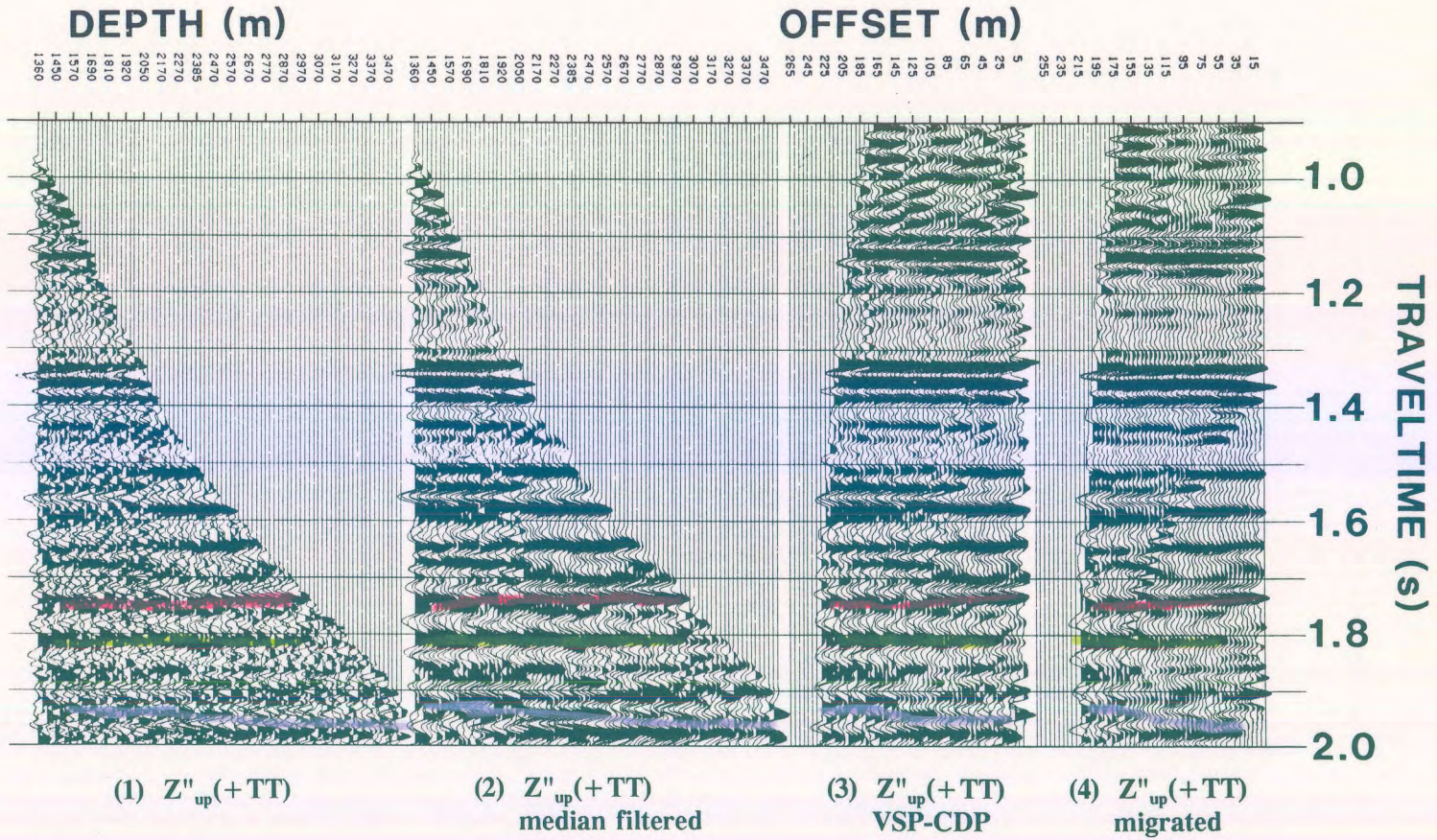

Figure 2.48 VSP-CDP and migration IPP for the Simonette far-offset non-deconvolved data (Hinds et al., 1993b). A possible multiple event occurs at 1.8 s (peak).

curve. This may be a real geological event that phases out before the borehole and subsequently would not be on the borehole logs; however, it could also be a multiple of the Wabamun primary event.

The $\mathbf{Z'_{down}(-TT)}$ data were used to deconvolve the $\mathbf{Z_{up}(+TT)}$ data from panel 1 of Figure 2.48 to output the $\mathbf{Z_{up(decon)}(+TT)}$ data in panels 1 and 2 of Figure 2.49. The deconvolution has been successful in attenuating the possible multiple and the interpretation of the reef events (in "reef" purple) can proceed on the VSP-CDP and migrated data shown in panels 3 and 4. The two IPP's shown in Figure 2.48 and 2.49 can be interpreted cooperatively in order to interpret through possible deconvolution noise.

2.3.5. Problematic far offset interpretive processing

In this section, the far offset polarization and deconvolution processing of the Ricinus carbonate reef case study (Hinds et al., 1989a; Hinds et al., 1993c; Hinds et al., 1994c) shall be presented. The case study presented in Chapter 4 also highlights the difficulties within the data processing that were solved through the interpretive processing of the far offset data; however, in the context of more detailed interpretation.

The two procedures that will be shown are:

(1) the far offset time variant polarization; and

(2) far offset deconvolution.

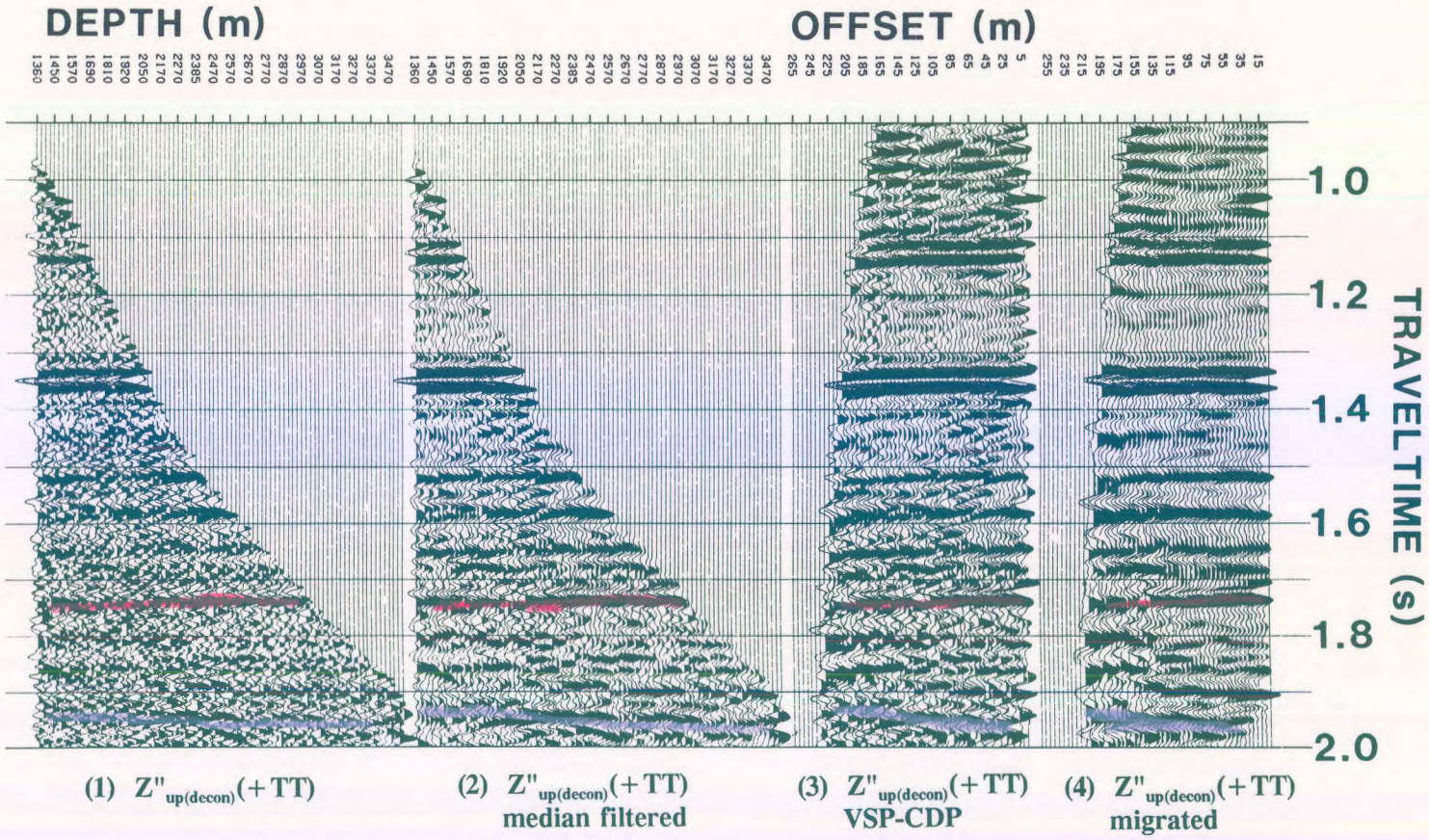

Figure 2.49 VSP-CDP and Kirchhoff migration IPP for the Simonette far-offset deconvolved data (Hinds et al., 1993b). The suspected multiple at 1.8 s has been attenuated; however, the reef interpretation (detailed in chapter 6) remains.

2.3.5.1 Time variant polarization of the Ricinus case study data

Figure 2.50 shows the time variant polarization IPP for the Ricinus carbonate reef case study (Chapter 4) far-offset (1100 m) data after "normal" processing. The processing followed the guideline far offset processing runstream presented in section 2.1.

The **Z"$_{up}$(FRT)** data (panel 6) is contaminated with diffractions and mode-converted SV up- and downgoing events highlighted in yellow. The same mode-converted SV events, also highlighted in yellow, are shown in panel 1 of the VSP-CDP IPP in Figure 2.51. On panel 1 (Fig. 2.51), upgoing P events highlighted in orange intersect the first break "curve" between the 3300 and 3510 m traces. Linear events, highlighted in yellow, trending from the left hand bottom corner of panel 1 cross the data and merge with the highlighted (in orange) P-wave events. The yellow highlighted events represent the upgoing SV events that are contaminating some of the underlying P-wave data.

The downgoing mode-converted SV events can be seen better on panels 2, 3, 5 and 6 of Figure 2.50. These linear events (highlighted in green) trend in the same direction as the P-wave first break "curve" but at a steeper dip (implying a slower apparent velocity).

The first break "curve" does not exist following the downgoing wavefield separation processing. The "curve" refers to the mute limit on the data chosen using the first breaks.

The second stage of interpretive processing is now accomplished. By interpreting the "noise" (mode converted up- and downgoing SV events), the interpreter/processor can begin to

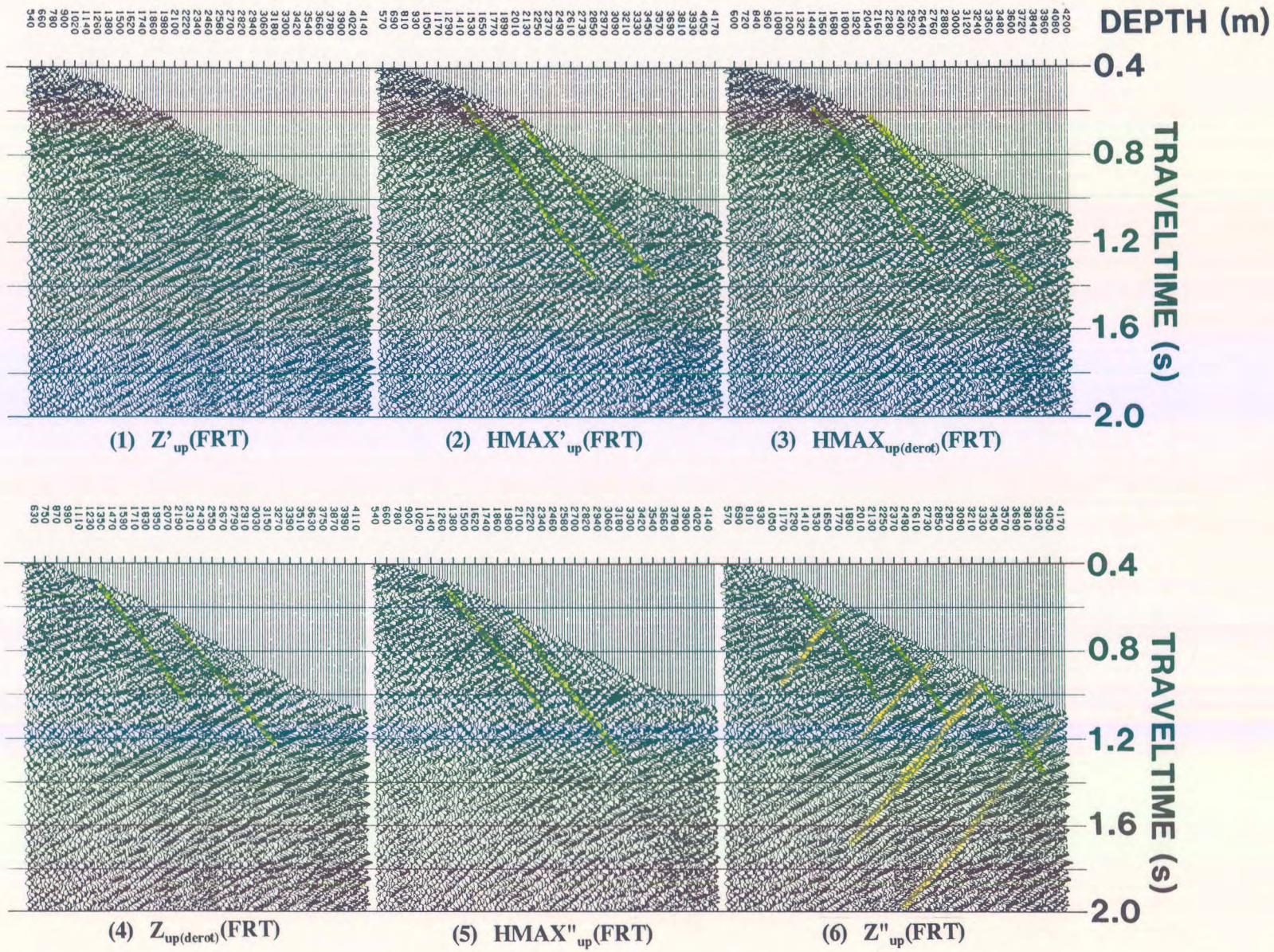

Figure 2.50 Time-variant polarization IPP for the Ricinus data (Hinds et al., 1989a; Hinds et al., 1994b) using the example far-offset processing initially presented in the "processing runstreams" section of chapter 2.

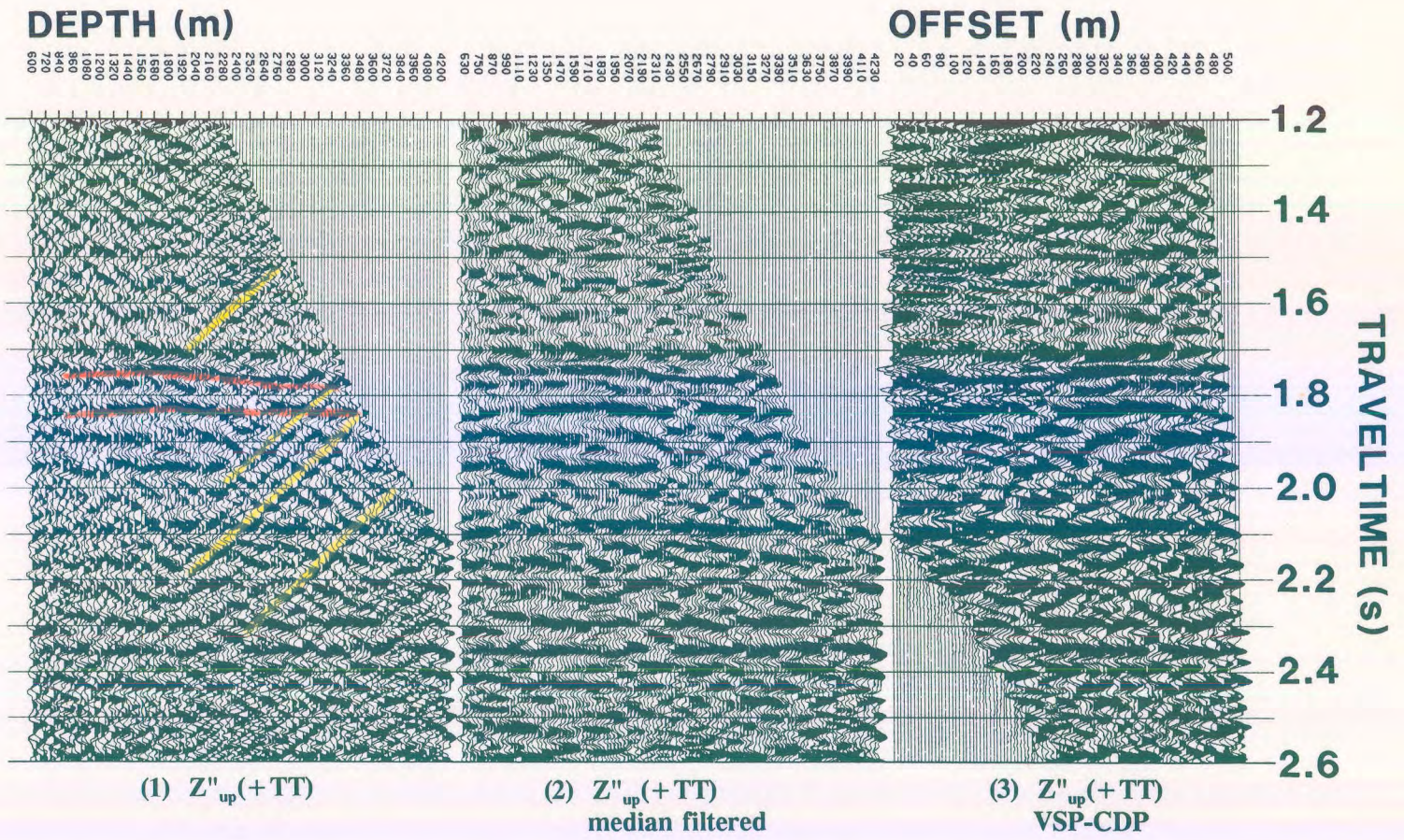

Figure 2.51 VSP-CDP IPP for the Ricinus data (Hinds et al., 1989a; Hinds et al., 1993c) using the $\mathbf{Z}''_{up}$ data shown in Figure 2.50. The upgoing P-wave events are difficult to interpret due to up- and downgoing SV-wave events.

redesign the processing to minimize the "unwanted" noise.

It was decided to go back to the **Z(FRT)** and **HMAX(FRT)** data and perform the wavefield separation on these two data panels (and not the **Z'(FRT)** and **HMAX'(FRT)** data as suggested in the processing guidelines of section 1.2). The wavefield separation processing included the attenuation of the mode-converted SV events. The results of the new processing runstream are shown in the updated time variant IPP shown in Figure 2.52.

The input **HMAX(FRT)** and **Z(FRT)** data are shown in panels 1 and 2. The wavefield separated $\mathbf{HMAX_{up}(FRT)}$ and $\mathbf{Z_{up}(FRT)}$ data in panels 3 and 4 can now be compared to the original $\mathbf{HMAX_{up(derot)}(FRT)}$ and $\mathbf{Z_{up(derot)}(FRT)}$ data in panels 3 and 4 of Figure 2.50 (the guideline runstream processing). Bypassing the (**Z**, **HMAX**) to (**Z'**, **HMAX'**) rotation (and possible noise generation caused by the polarization), the upgoing P events (some are highlighted in orange in panels 3 and 4 in Fig. 2.52) are more interpretable on the new processing. Time-variant polarization of the $\mathbf{HMAX_{up}(FRT)}$ and $\mathbf{Z_{up}(FRT)}$ data produces the $\mathbf{HMAX"_{up}(FRT)}$ and $\mathbf{Z"_{up}(FRT)}$ data shown in panels 5 and 6.

The VSP-CDP IPP display shown in Figure 2.53 for the modified processing runstream shows that the upgoing P events are much easier to follow and subsequently to interpret than the results presented in the VSP-CDP IPP using the original processing (Fig. 2.51). An example of this are the upgoing events highlighted in orange on panels 1 of Figures 2.51 and 2.53.

The $\mathbf{Z"_{up(med)}(+TT)}$ data in panel 2 of Figure 2.53 was created using a 5 point median filter

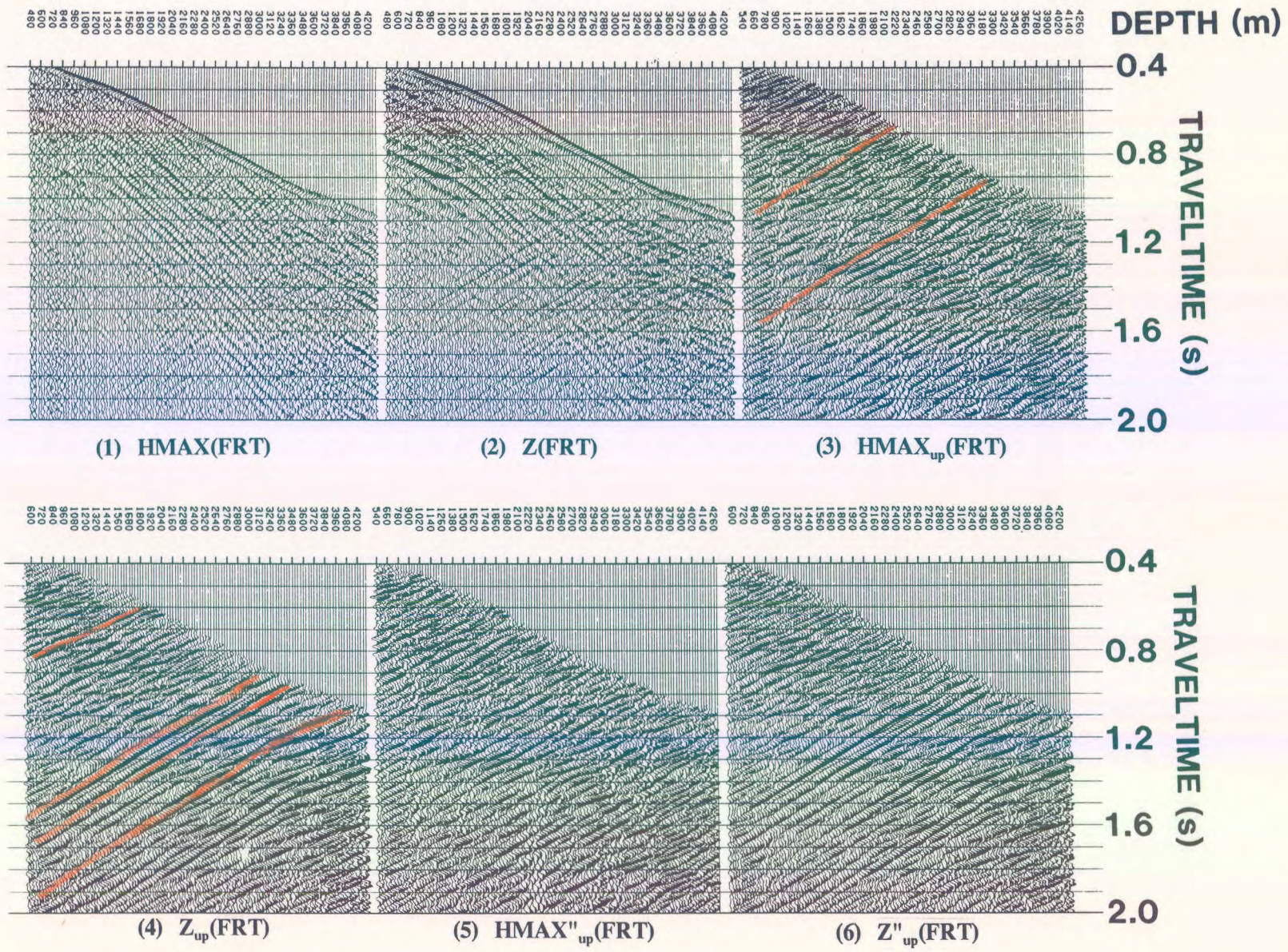

Figure 2.52 Modified time-variant polarization and wavefield separation IPP for the Ricinus data (Hinds et al., 1993c) following processing decisions made using interpretive processing.

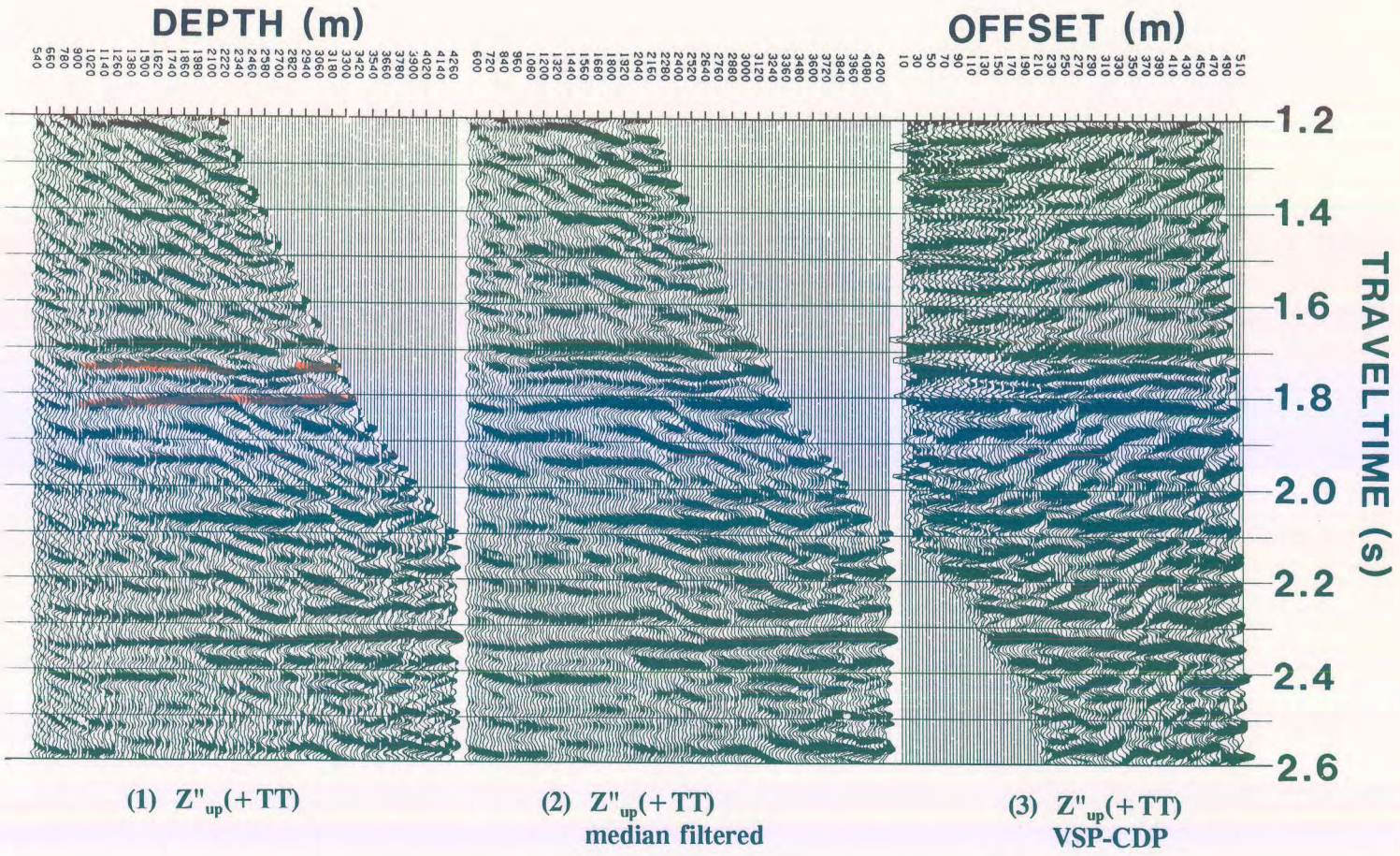

Figure 2.53 VSP-CDP IPP for the Ricinus data (Hinds et al., 1989a; Hinds et al., 1994b) using the $\mathbf{Z''_{up}}$ data shown in Figure 2.52. The upgoing P-wave events are more interpretable although the diffraction and downgoing SV-wave events have not been completely eliminated.

on the data seen in panel 1. Additional VSP-CDP displays using 9 and 11 point median filters to enhance the upgoing events on the **Z"$_{up}$(+TT)** data are shown in Figures 2.54 and 2.55, respectively. As noted before, the interpreter/processor would derive an interpretation from Figures 2.53 to 2.55; however, one would also verify that the same events are resident on Figure 2.51. Interpretive processing includes every piece of information available during the interpretation stage.

2.3.5.1 Far offset deconvolution of the Ricinus case study data

In this section, the far offset deconvolution of the Ricinus carbonate reef case study (Hinds et al., 1989a; Hinds et al., 1994c) is examined. The deconvolved far offset results are also presented in Chapter 4 (Hinds et al., 1994c) in order to examine the evaluation of deconvolution generated noise testing in the context of a case study.

The far offset deconvolution IPP for the Ricinus far offset (1100 m) data is shown in Figure 2.56. The **HMAX'(-TT)** and **HMAX'$_{down}$(-TT)** data are shown in panel 1 and 2, respectively. By inspection, the **HMAX'$_{down}$(FRT)** data do not posses an abundance of multiple events. Few, if any, multiple events are seen after the primary downgoing event.

The deconvolution verification panel contains the deconvolved downgoing events and is shown in panel 3. This is the result of applying the deconvolution processing to the downgoing events themselves. The **Z"$_{up}$(-TT)** data of the updated interpretive processing

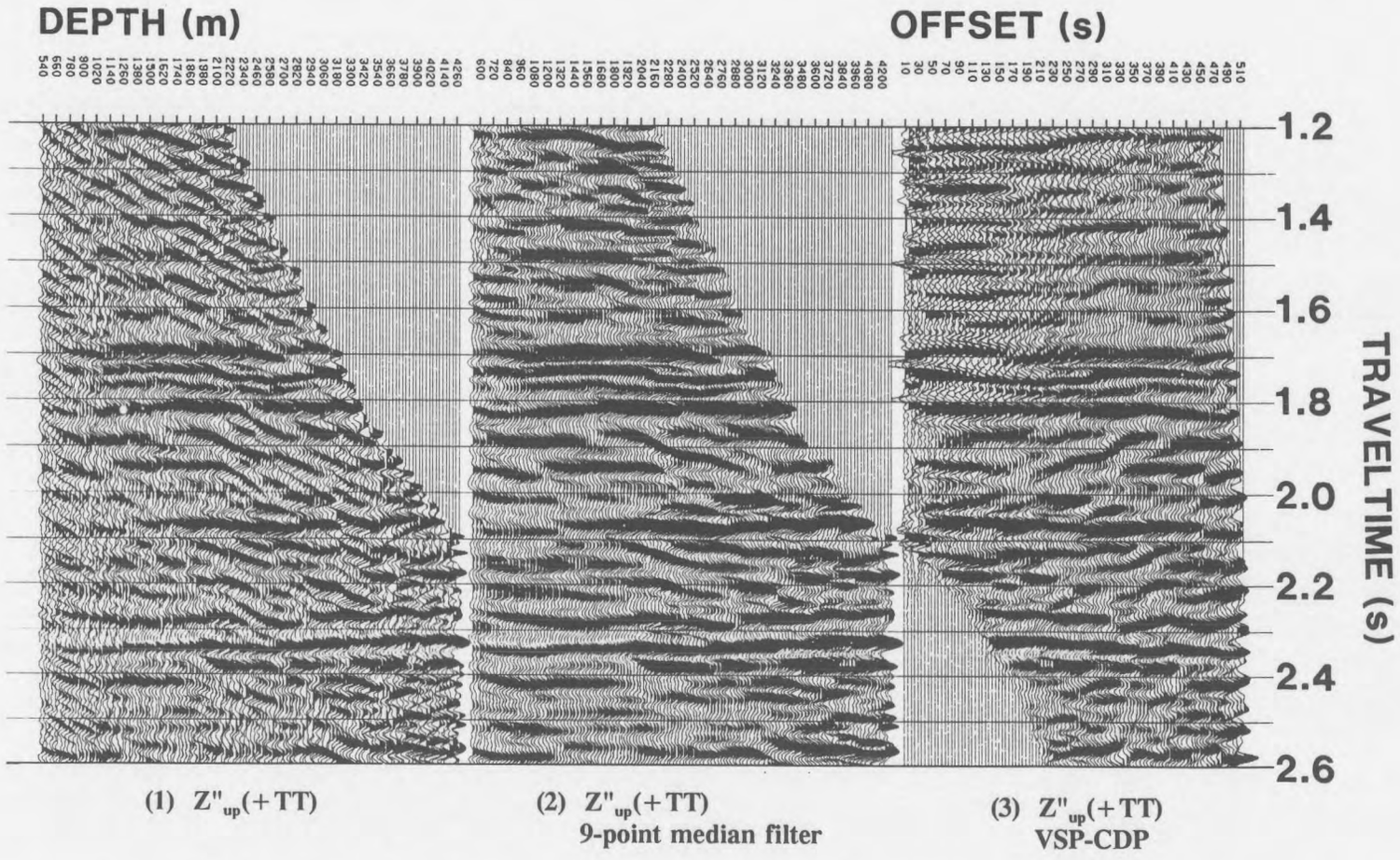

Figure 2.54 VSP-CDP IPP for the Ricinus data (Hinds et al., 1994b) with the Z''_{up} data shown in Figure 2.51 as input and data enhancement using a 9-point median filter.

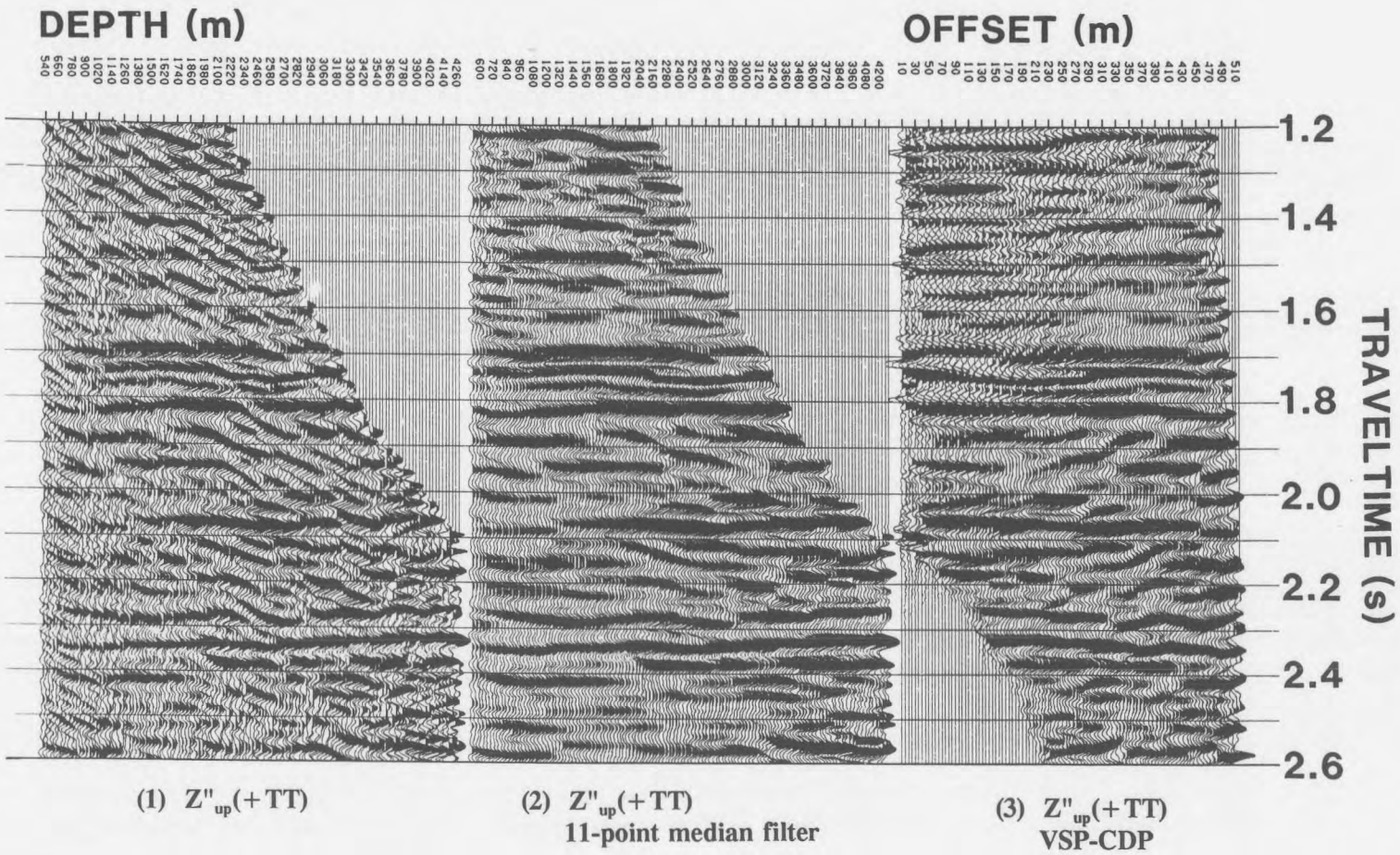

Figure 2.55 VSP-CDP IPP for the Ricinus data (Hinds et al., 1994b) with the Z''_{up} data shown in Figure 2.51 as input and data enhancement using a 11-point median filter.

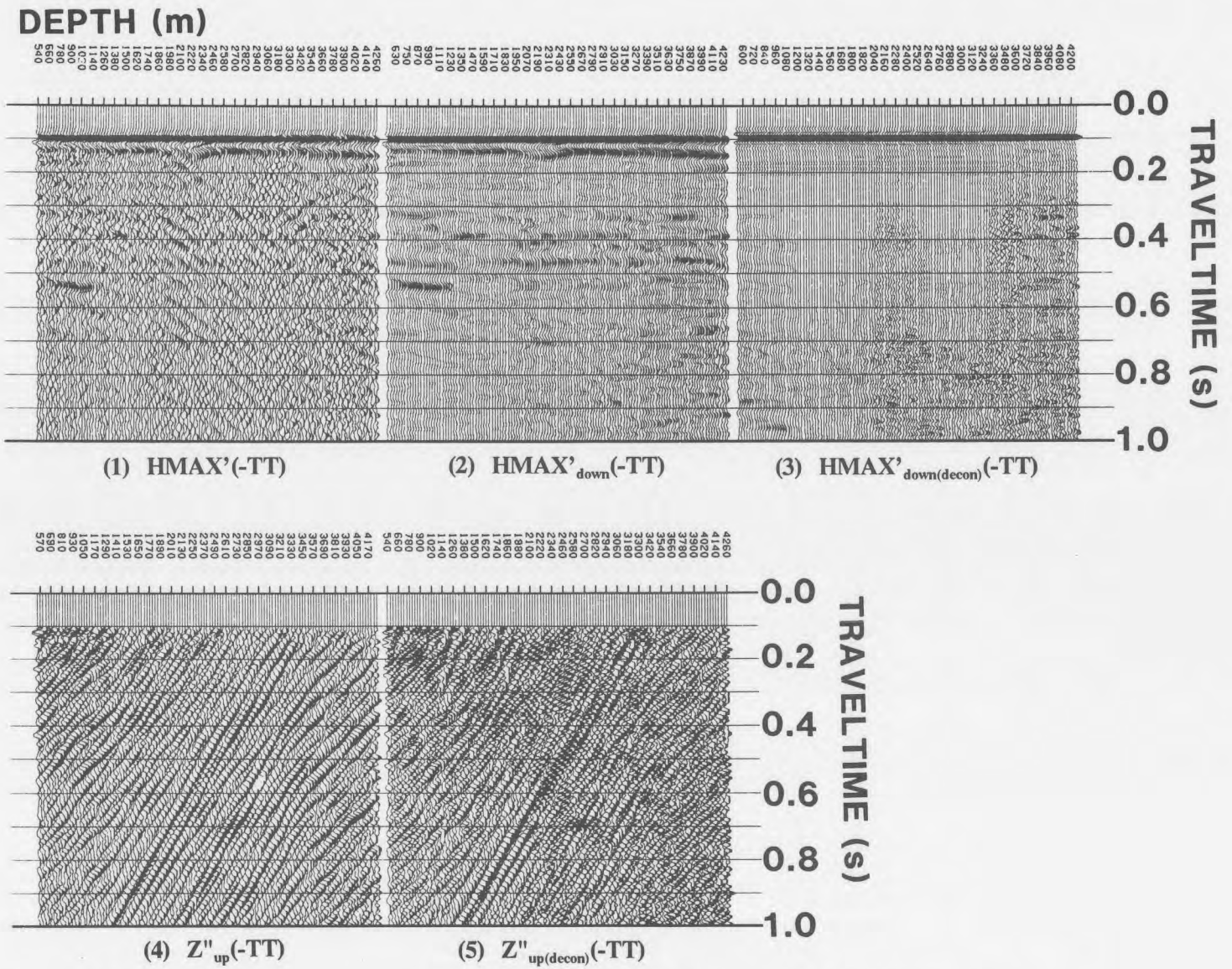

Figure 2.56 Far offset deconvolution IPP for the Ricinus data (Hinds et al., 1994b). Note the deconvolution induced noise by comparing panels 4 and 5.

(shown in Fig. 2.52) are shown in panel 4. The $\mathbf{Z''_{up(decon)}(-TT)}$ data are shown in panel 5. By inspection of panels 4 and 5, the deconvolution process has added undesirable noise to the upgoing event data.

The VSP-CDP IPP of the $\mathbf{Z''_{up(decon)}(+TT)}$ data is shown in Figure 2.57. The interpretation of the data was damaged by the addition of deconvolution noise. One reason for the deconvolution processing failure is that the simple time delay relationship between up- ($\mathbf{Z''_{up}}$) and downgoing ($\mathbf{HMAX'_{down}}$) events may not be satisfied for the far-offset data (1100 m offset).

2.4 Integrated displays

2.4.1 Integrated Log Display (ILD)

The integrated well log display highlights the seismic data around the well, the geological log data (in time) and the synthetic seismogram as shown in Figure 2.58. This display is included because, in practice, the VSP survey is usually the final survey to be run on a well following the acquisition of the geological logs. By the time that the VSP is processed, the sonic log should have been digitized and ready for the "check-shot" type of calibration.

Whilst the VSP is being processed, the near offset VSP first break times can be used to calibrate the sonic log (correct for sonic log drift and tie the integrated sonic log to the VSP first break times). The seismogram and calibrated sonic log (merged onto the seismic line

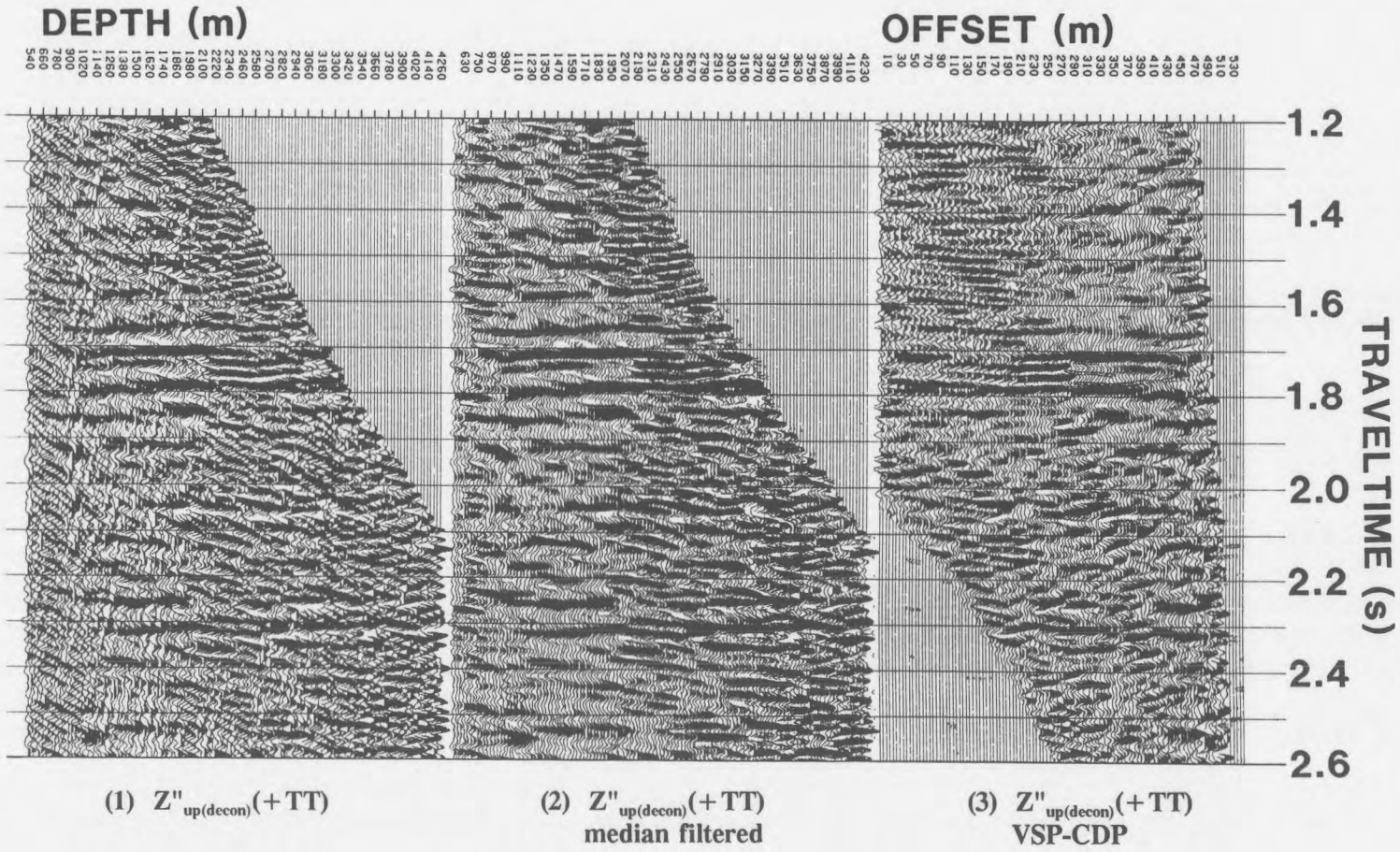

Figure 2.57 VSP-CDP IPP for the Ricinus $Z''_{up(decon)}(+TT)$ data (Hinds et al., 1994b). The deconvolution was not successful and was dropped from the Ricinus case study "normal" far offset processing runstream flow.

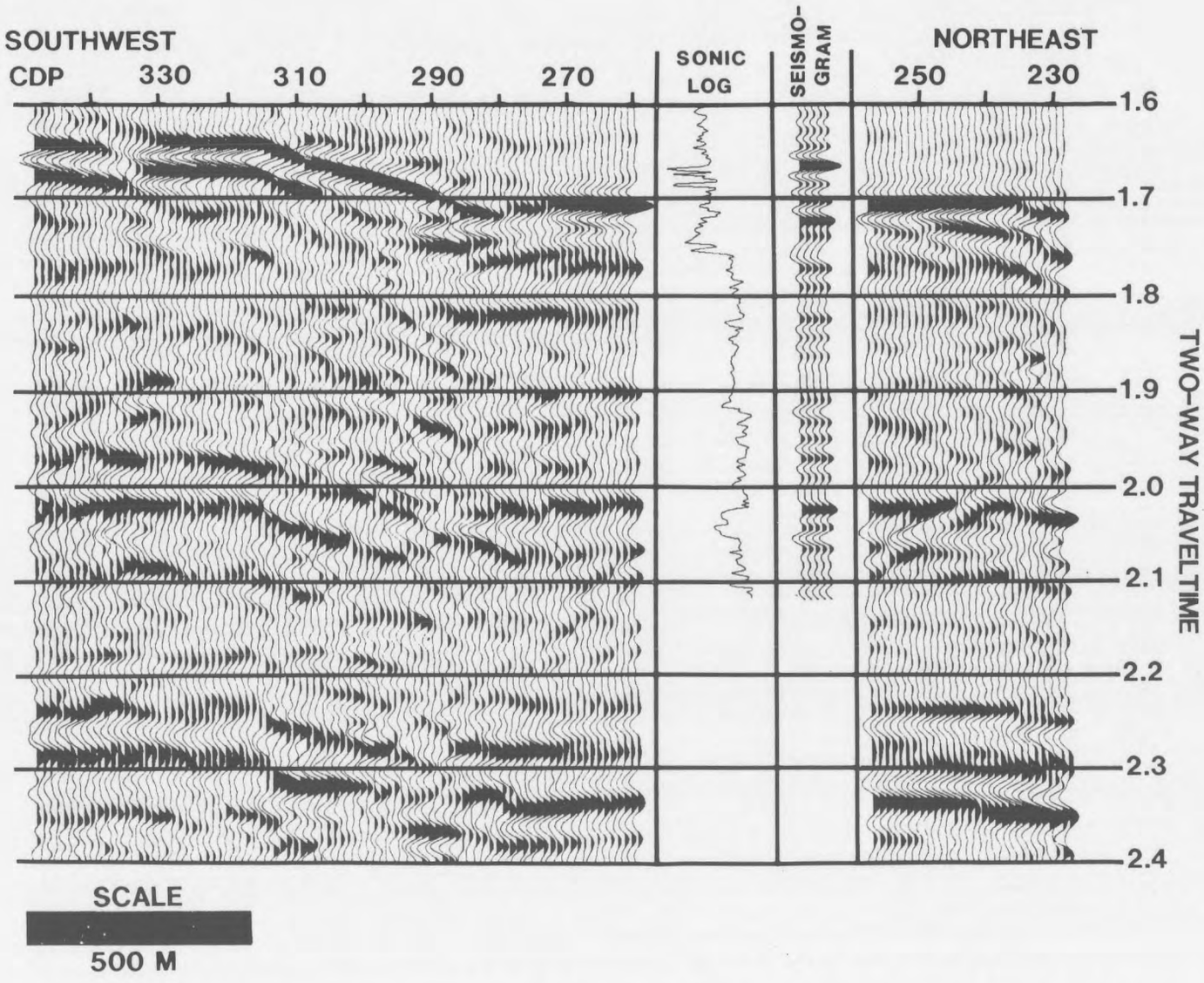

Figure 2.58 Integrated log display (ILD) for the Ricinus data (Hinds et al., 1989a; Hinds et al., 1994b).

on the ILD) can assist the interpreter to get a first-hand look at the location of the seismic events that were "intersected" by drilling.

2.4.2 Integrated Seismic Display (ISD)

The integrated seismic display for the Ricinus carbonate reef case study (Hinds et al., 1989a; Hinds et al., 1993c; Hinds et al., 1994c) is shown in Figure 2.59. The display contains the VSP-CDP (or migration) results merged with the surface seismic. The VSP-CDP is lateral offset data imaging the reflectors away from the well and can provide a high-resolution image of the reflectors in comparison to the same events seen on surface seismic.

2.4.3 Integrated Interpretive Display (IID)

At the final presentation stage of the project, a large part of the geoscience exploration results should be displayed. This is accomplished using the integrated interpretive display. The IID shown in Figure 2.60 displays the integrated results from the Simonette carbonate reef case history (Hinds et al., 1991b; Hinds et al., 1993b and 1994c).

This case study involves using the data to substantiate the need for a well "whipstock". It

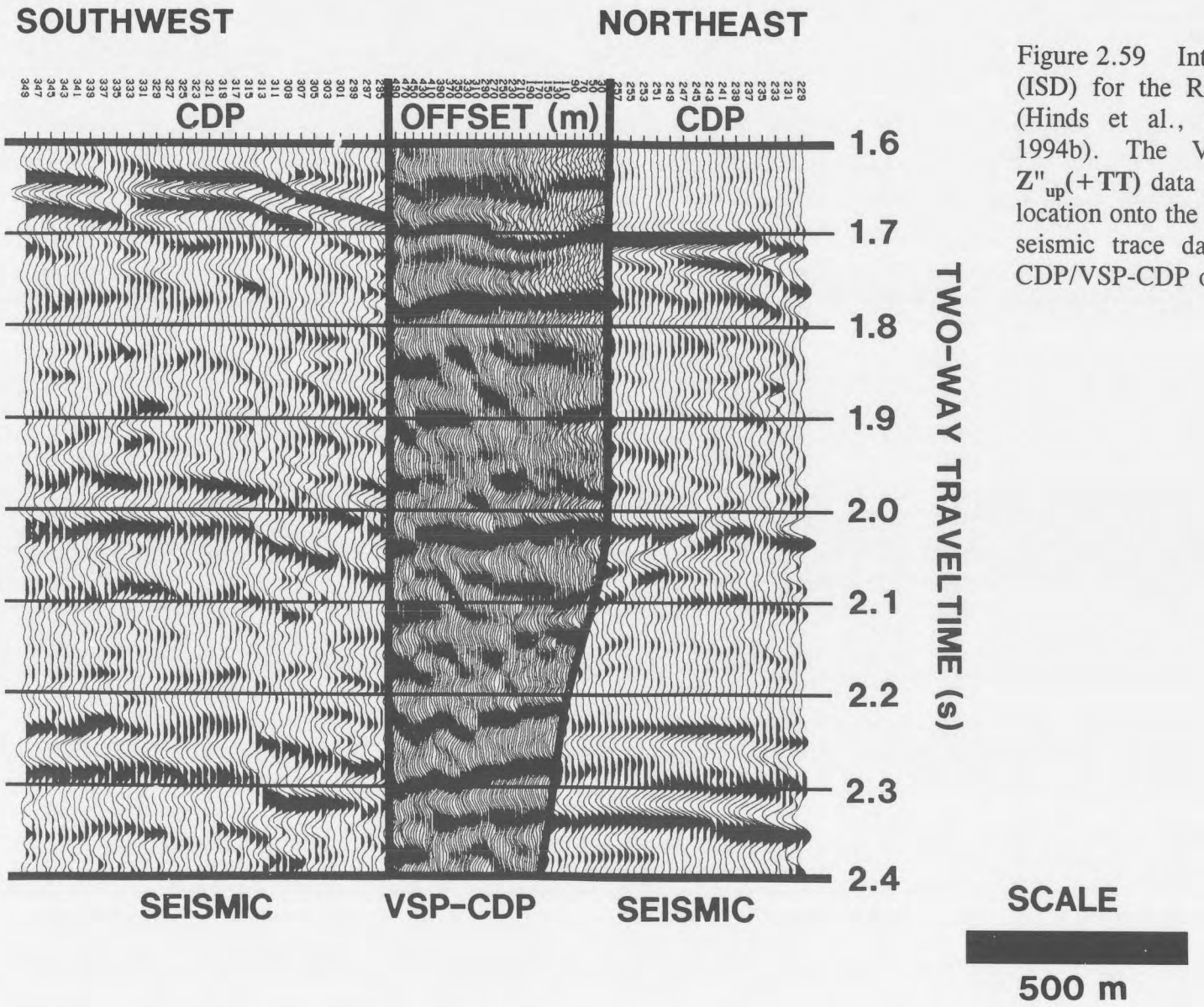

Figure 2.59 Integrated seismic display (ISD) for the Ricinus case study data (Hinds et al., 1989a; Hinds et al., 1994b). The VSP-CDP transformed $Z''_{up}(+TT)$ data are inserted at the well location onto the seismic and replace the seismic trace data at the overlapping CDP/VSP-CDP offset locations.

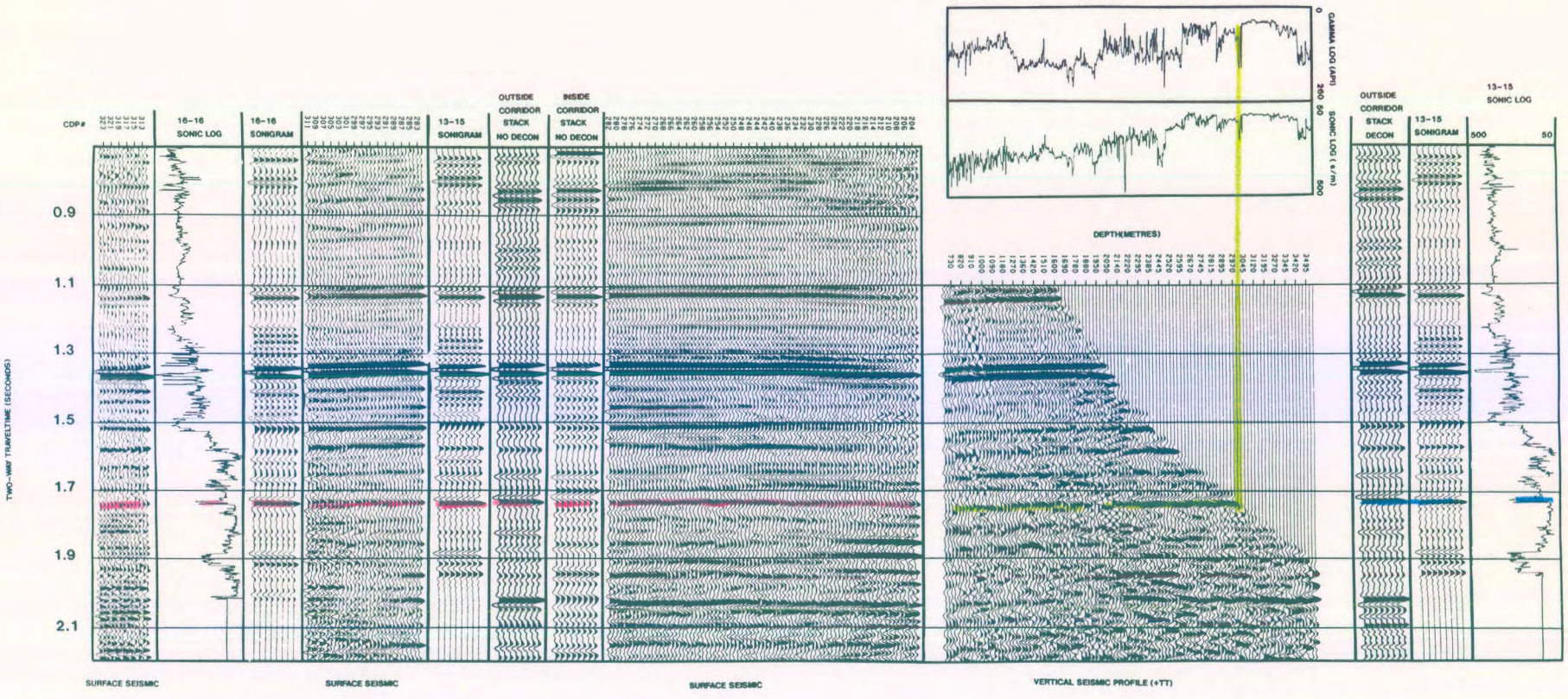

Figure 2.60 Integrated Interpretive Display (IID) of the Lanaway case study data (Hinds et al., 1989a; Hinds et al., 1994a). The display includes sonic and gamma logs (both in time and depth), the $\mathbf{Z_{up}(+TT)}$ VSP data, corridor stack results and surface seismic data. This panel incorporates all of the exploration data for the area onto one single display for easy integrated interpretation.

was interpreted that the reef is beyond the "economic" reach of the whipstock (Hinds et al., 1993b and 1994c). The IID is used to conveniently show the lateral coverage and the interpretation away from the well towards the "known" reef on the far offset VSP in conjunction with the information available from the other types of exploration data.

The IID can be used to explain the entire interpretation procedure and how the different datasets tie. For example, the Wabamun Formation interface was interpreted from the sonic and gamma log to be at 3020 m well depth. Starting with the sonic and gamma logs in depth on Figure 2.60, a line can be drawn through the sonic and gamma high (at 3020 m) down to the upgoing (peak) event that intersects the 3020 m depth trace on the far offset $\mathbf{Z''_{up}(+TT)}$ data. This line is shown in green on Figure 2.60. The Wabamun seismic marker is now tied to the logs through the common depth axis of the far offset VSP data (centre panel) and the logs (located above the centre panel).

The Wabamun VSP event can be tied to the surface seismic event at the 13-15 well using the time tie from the geologic logs. To the right of the VSP data are the outside corridor stack after deconvolution (to show primary events), the 13-15 synthetic seismogram and the 13-15 sonic log displayed in two-way traveltime. Using the tie of the VSP to the geologic logs, an interpreted Wabamun event can be further confirmed by tying the event (on the 3020 m trace) to the corridor stack, sonigram and sonic log (in time). This is shown by a blue line in Figure 2.60.

This tie can be drawn on the 13-15 sonigram, outside corridor stack of the $\mathbf{Z_{up(decon)}(+TT)}$ data and inside corridor stack of the $\mathbf{Z_{up}(+TT)}$ data that are spliced into the surface seismic

at the 13-15 well location. This is seen on the left panel of Figure 2.60. The nondeconvolved inside corridor stack would enable an interpretation of multiples on the surface seismic at the 13-15 well location. The interpretation of the Wabamun event (shown in red) is extrapolated onto the surface seismic on either side of the well. The 16-16 sonic log (in time) and 16-16 sonigram are spliced into the seismic section at the 16-16 well location. This will enable the interpretation of the reef at the 16-16 location.

The interpreted basal reef marker rising onto the reef pinnacle can be shown on the far offset VSP data panel (see chapter 6 or Hinds et al., 1991b and 1993b; Hinds et al., 1994c).

The VSP-CDP IPP displays would complete the presentation (Figs. 2.48 and 2.49) by showing the reef interpretation at the well and laterally offset for 200 m away from the well towards the "known" reef (at the 16-16 well). Questions about the effects of multiples are answered and the tie of the geology to the geophysics is resolved. The economics are discussed in the view of production penalties (caused by whipstocking the well onto another company's "zone") and the interpretation that the reef is encountered approximately 120 m away from the new well.

Interpretive processing has driven the processing and the various IPP and displays confirm the interpretation.